
# Elucidation of structure and dynamics of compounds related to medical imaging techniques

PhD Thesis

Éva Csajbók

University of Debrecen
Debrecen, 2005.

*Családomnak* *To my family*

*„Ma...szemtanúi vagyunk a kísérletes tudomány gyors elterjedésének, amint megváltoztatja az emberi lét paramétereit, és egy merőben új világot teremt... Ennek a változásnak egy új, tudományos gondolkodás az alapja. Ennek a gondolkodásnak alapvető vonása az alázatosság, tökéletlenségünk felismerése. Ez a gondolkodás először is arra ösztönöz bennünket, hogy bizonyíték nélkül semmit se fogadjunk el, a problémákkal mint olyanokkal, hideg fejjel, félelem vagy előítélet nélkül, a gondolkodás meg nem alkuvó becsületességével, félelem, remények, vagy érdek által nem befolyásolva nézzünk szembe.”*

*Szent-Györgyi Albert*

*“Today...we see experimental science in rapid expansion, changing all the parameters of human existence, creating an entirely new world... What underlies this change is a new scientific thinking. The essential feature of this thinking is humility, the realization of our imperfections. The first command of this thinking is to accept nothing without evidence, face problems as such, with a cool head, without fear or prejudice, with uncompromising honesty of thought, unbiassed by fear, hopes, or interest.”*

*Albert Szent-Györgyi*

## Table of Contents

# 1 General Introduction

Imaging of internal human organs with exact and non-invasive methods is very important for medical diagnosis, treatment and post-treatment follow-up. Before the recent advances in medical technology, our knowledge of the internal structure of the human body had mostly relied on surgical methods, hence the word anatomy (from Greek: cutting up). Nowadays, tomography, another word with Greek origin, is associated with a virtual "cutting up" process (*tomos*: a cut, *graph:* written).

In x-ray computer-assisted tomography (CT) the signal intensity in the final picture reflects electron density. The technique applies ionising radiation, x-rays. Usually tungsten is used as x-ray tube target material. The resulted x-ray emission spectrum is a combination of general radiation (Brehmsstrahlung) (maximum intensity is at 45-50 keV, maximum photon energy is 150 keV) and characteristic radiation (57-69 keV). The low-energy photons are removed by aluminium or copper filtration for safety reasons.[1]

When x-ray beam traverses matter, the reduction of beam intensity due to absorption and deflection leads to attenuation, following Eq. 1.1.

$$I = I_0 e^{-\mu x} \qquad \text{Eq. 1.1}$$

where $I$ is the transmitted, $I_0$ is the incident x-ray intensity and $x$ is the thickness of the absorber. The mass attenuation coefficient, μ, is expressed in $cm^2/g$. μ is the sum of three contributions: the coherent scattering, the photoelectron effect and the Compton scattering. Coherent scattering is so minor as we can exclude from further consideration, photoelectron effect is briefly an interaction between the x-ray photons and the inner-shell electrons while Compton scattering arises from the interaction between x-ray photons and outer-shell electrons. Therefore, without going into details, the value of μ can provide information about the electron density of the matter under study. If we study two neighbouring regions with different mass attenuation coefficients, the percental difference between the two transmitted intensities, $I_1$ and $I_2$, is defined as the x-ray contrast and as a function of the thickness and the mass attenuation coefficients of the different tissues (Eq. 1.2, Figure 1).

$$\frac{I_1 - I_2}{I_1} = 1 - e^{-(\mu_2 x_2 - \mu_1 x_1)} \qquad \text{Eq. 1.2}$$

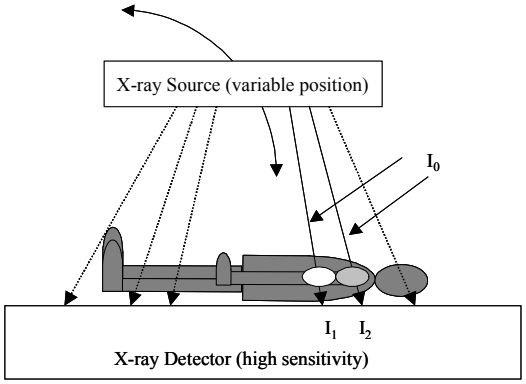

**Figure 1.** Schematic representation of a patient undergoing an x-ray CT imaging procedure. $I_0$ is the incident, $I_1$ and $I_2$ are the transmitted intensities.

X-ray attenuation is also a function of x-ray photon energy. The differences among mass attenuation coefficients of body tissues (bone, muscle, fat) become smaller as x-ray photon energy increases, leading to poor contrast. To gain better contrast, contrast-enhancing agents (contrast agents, CAs) with differential uptake in different tissues are used in CT. All x-ray contrast agents contain a heavy element (I, Ba, Ce, Gd, Tb, Dy, Yb, Au, Pb, Bi) and contrast enhancement mainly results from the photoelectron effect due to their large atomic numbers. The photoelectron effect induces sharp increase in the mass attenuation coefficient at the K-shell binding energy, therefore results in higher contrast.[1]

In 1979, Allan M. Cormack and Godfrey Newbold Hounsfield were awarded the Nobel Prize in Physiology or Medicine for the development of computer-assisted tomography.[2] By this method the cross-sectional imaging was born. The basic feature of the method is that the x-ray tube permits the rays to sweep in many directions through the cross-section of the body under examination. The detection is made by sensitive crystal detector and the signals are stored and analysed by a computer. The obtained two-dimensional picture corresponds to the examined cross-section of the body as each individual tiny square (pixel) in the picture corresponds to a tiny part of the examined organ. The main advantage is that the separate parts do not influence each other during the image reconstruction and there is no overlapping of elements in the image, in contrast with the traditional x-ray

examination. Like its predecessor, CT, magnetic resonance imaging (MRI) is also a computer-based imaging modality. In MRI, ionising radiation is not used; the nuclear magnetic resonance (NMR) signal intensity of the $^1$H nuclei is measured. The $^1$H nuclei have the advantages of high NMR sensitivity, high natural abundance and their omnipresence (more than 70% in weight of the human body is water).

Spatial encoding in MRI is obtained by using field gradients superimposed on the main, homogenous magnetic field (Figure 2). While the intense main field, $B_0$ is aligned in the $z$ direction (in MRI, the $z$ direction is defined along the lying patient from the head to the toe), the gradient fields are generated in $z$, $x$, and $y$ direction and are extremely weak in comparison with $B_0$.

Slice selection in MRI involves the use of the $z$ gradient and a selective (soft) radiofrequency pulse during the excitation period. Since the applied $z$ gradient results in the $^1$H nuclei at different positions resonating at different fields ($B_0+B_1$, $B_0+B_2$, $B_0+B_3$, etc. where $B_1$, $B_2$ and $B_3$ are the different field components caused by the field gradient), the excitation of the desired slice (the slice selection) can be easily made by adjusting the frequency of the selective radiofrequency pulse so that only the $^1$H nuclei of this slice are at resonance.

Phase encoding is used to determine the distribution in the $y$ direction. Usually it is performed by a sequence of independent measurements with stepwise incrementation of the strength of the $y$ gradient pulse during the signal evolution period. The rate of dephasing of the magnetisation vectors is dependent on the strength of the $y$ gradient, therefore on the position of the $^1$H nuclei in the $y$ direction.

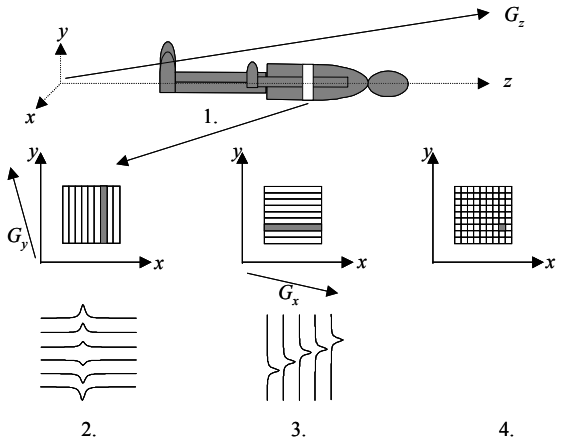


**Figure 2.** Schematic representation of a patient undergoing an MRI procedure. 1. Slice selection, 2. Phase encoding 3. Frequency encoding, 4. The final pixel. *Gz, Gx, Gy* are the applied magnetic field gradients in the appropriate directions

Frequency encoding is used in the readout stage and gives information about the distribution in the *x* direction. This is carried out by applying *x* gradient during the acquisition of the NMR response. $^{1}$H nuclei at diverse positions in the *x* direction experience different values of the gradient therefore are detected at different precessing frequencies.[3]

After detection, by a computer-assisted mathematical process similar to the one used in CT, it is possible to reconstruct the image. By this "back-projection", the contrast among the pixels in the final image corresponds to the difference in signal intensities of the various tiny cubes (voxels) of the examined part of the body.[4]

The obtained signal intensity reflects the density of mobile $^{1}$H nuclei modified by the chemical environment, e.g. by the relaxation times, $T_1$ (longitudinal or spin-lattice relaxation time) and $T_2$ (transverse or spin-spin

relaxation time). One of the most commonly used measuring pulse sequence is the spin-echo sequence. The signal intensity obtained by applying this sequence is given by Eq. 1.3.

$$I = N(^1H)\left(1 - e^{-TR/T_1}\right)e^{-TE/T_2} f(\nu) \qquad \text{Eq. 1.3}$$

Here, $N(^1H)$ is the proton density, *TR* (repetition time) and *TE* (echo delay time) are inserted time intervals in the spin-echo sequence and $f(\nu)$ is a parameter dependent on flow.[5]

By using appropriate values of *TR* and *TE* it is possible to construct images not only with contrast reflecting differences in $^1$H density (proton-density weighted images), but images emphasising the differences in $T_1$ ($T_1$-weighted images) or $T_2$ ($T_2$-weighted images). Among common clinical problems are the detection of brain oedemas, primary or metastatic tumours, inflammation, or infarction. Since oedema has longer $T_1$ and $T_2$ than normal brain, and tumours have usually even longer $T_1$ than oedemas, $T_1$ or $T_2$-weighted images can be used to determine the alteration.[5] The contrast can be increased by using MRI contrast agents, which are usually paramagnetic compounds, mostly containing $Gd^{3+}$-ions. CAs decrease $T_1$ and $T_2$ values of the surrounding water protons, and in this way they can enhance the contrast. The recent advances in MRI CAs beyond the obtained increased image quality, such as special targeting of various tissues, design of responsive CAs for altering physiological conditions or inventing special CAs for MR angiography definitely assisted the MRI technique to become a widely

known and acknowledged diagnostic method in medicine. In 2003, Paul C. Lauterbur and Peter Mansfield were awarded the Nobel Prize in Physiology or Medicine for their discoveries concerning magnetic resonance imaging.[2]

Both in CT and MRI, the used CAs are facing with strict requirements. They, when administered to a patient, should enter and pass through anatomic regions of interest to provide contrast enhancement. Afterwards, these agents must be essentially completely excreted without being metabolised.

The undesirable biodistribution and excretion profile of heavy metal ions can be altered successfully by using metal chelate complexes. In general, the metal chelate complexes have lower *in vivo* absorption and therefore lower toxicity than the metal ions themselves. For example, $Gd^{3+}$ as free metal ion rapidly hydrolyses under physiological conditions, forming insoluble $Gd(OH)_3$. In this form, it accumulates in liver or bones from where it is successively released. The $Gd^{3+}$ can compete for binding sites usually occupied by endogenous ions such as $Ca^{2+}$, $Cu^{2+}$ and $Zn^{2+}$.[6,7] A chelate complex with high thermodynamic stability and kinetic inertness under physiological conditions can reduce the interaction with the biological system; therefore the metal complex can be excreted without significant accumulation or metabolisation.

The other requirement for these contrast agents is to provide large contrast with low administered dose, in other words, to have high efficacy. The parameters influencing this effectiveness are discussed in the Bibliographic Review. To develop efficient CAs it is necessary to gain information about the inherence between the structural and dynamic properties of these compounds and their effectiveness.

*During my Ph.D. work at the University of Debrecen, Hungary and at the Technical University of Delft, The Netherlands, the structure and dynamics of several, inert and labile complexes formed with polyamino-polycarboxylate (EOB-DTPA) and macrocyclic (DOTA) ligands have been investigated, mainly by multinuclear NMR spectroscopy. Our aim was to unravel new structural and dynamic properties according to the contrast agent applications, mainly focusing on the presence of various isomers in solution and the dynamic exchange processes among them. In the case of a new type of MRI contrast agent, Gd(III)-loaded zeolite nanoparticles, parameters influencing the relaxivity (efficiency of the MRI contrast agent) have been planned to study systematically, in order to clarify the mechanism of contrast enhancing effect of nanoparticles.*

# 2 Bibliographic review

## 2.1 Metal complexes as MRI contrast agents

Although MRI is regarded as a non-invasive technique, there are occasions when CAs are administered into the patient to enhance the contrast of the image. Paramagnetic ions, when administered, can reduce $T_1$ (and $T_2$) values of the water protons, even at low concentration. The most commonly used CAs are $Gd^{3+}$ chelates (Table 1, Figure 3).[8] $Gd^{3+}$, with its seven unpaired electrons is highly paramagnetic. Another advantage is that, due to its highly symmetric S-state, it has slower electronic relaxation, resulting in more effective $T_1$ (and $T_2$)-reducing effect on water protons.

The effectiveness in reducing relaxation times is expressed as the relaxivity. Relaxivity is the relaxation rate enhancement attributed to 1 mM $Gd^{3+}$ concentration, according to Eq. 2.1.

$$r_{1,2} = \left( \frac{1}{T_{1,2\ obs}} - \frac{1}{T_{1,2\ dia}} \right) \frac{1}{c_{Gd^{3+}}} \qquad \text{Eq. 2.1}$$

where $1/T_{1,2\ obs}$ is the observed relaxation rate at $c_{Gd3+}$ concentration, and $1/T_{1,2\ dia}$ is the relaxation rate measured in the absence of the paramagnetic contrast agents, in other words, in diamagnetic environment. $c_{Gd3+}$ is usually given in mM and therefore $r_{1,2}$ is expressed in $s^{-1}$ $mM^{-1}$.

The total relaxivity consists of two terms, an inner-sphere term ($r_{1,2}^{IS}$) and an outer-sphere term ($r_{1,2}^{OS}$) (Eq. 2.2a), and the same is true for the observed relaxation rates (Eq. 2.2b).

$$r_{1,2} = r_{1,2}^{IS} + r_{1,2}^{OS} \qquad \text{Eq. 2.2a}$$

$$\frac{1}{T_{1,2obs}} = \left(\frac{1}{T_{1,2obs}}\right)^{IS} + \left(\frac{1}{T_{1,2obs}}\right)^{OS} \qquad \text{Eq. 2.2b}$$

Generally, the coordination sphere of the overall nine-coordinated $Gd^{3+}$ consists of eight donor atoms of the chelate ligand and (at least) one inner-sphere water molecule. The protons of this coordinated water molecule in the immediate proximity of the paramagnetic metal centre relax fast due to the dipole-dipole interactions between the nuclear spins and the fluctuating local magnetic field raised by the unpaired electron spins. These inner-sphere water protons can exchange fast with the bulk water protons, thus the fastening of relaxation can be transferred to the bulk.

**Table 1**. Examples for commercially available MRI contrast agents

| **Chemical name** | **Generic name** | **Brand name** | **Company** | **Classification** |
|---|---|---|---|---|
| $[Gd(DTPA)(H_2O)]^{2-}$ | gadopentetate dimeglumine | Magnevist | Schering | extracellular |
| $[Gd(DOTA)(H_2O)]^{-}$ | gadoterate meglumine | Dotarem | Guerbet | extracellular |
| $[Gd(DTPA\text{-}BMA)(H_2O)]$ | gadodiamide | Omniscan | Nycomed-Amersham | extracellular |
| $[Gd(HP\text{-}DO3A)(H_2O)]$ | gadoteridol | ProHance | Bracco | extracellular |
| $[Gd(DO3A\text{-}butrol)(H_2O)]$ | gadobutrol | Gadovist | Schering | extracellular |
| $[Gd(DTPA\text{-}BMEA)(H_2O)]$ | gadoversetamide | OptiMARK | Mallincrodt | extracellular |
| $[Gd(BOPTA)(H_2O)]^{2-}$ | gadobenate dimeglumine | MultiHance | Bracco | hepatobiliary/extracellular |
| $[Gd(EOB\text{-}DTPA)(H_2O)]^{2-}$ | gadoxetic acid disodium | Eovist | Schering | hepatobiliary |
| MS-325 | gadophostriamine trisodium | AngioMark | EPIX/Mallincrodt | blood pool |

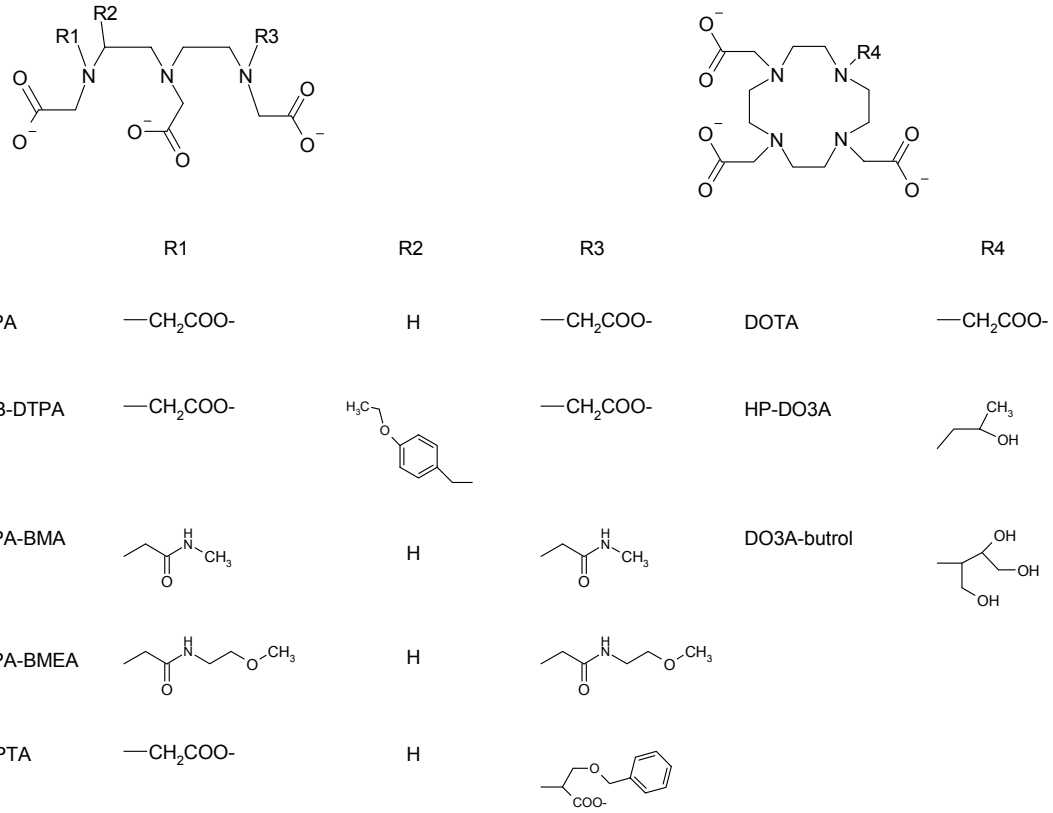


**Figure 3.** Structure of several ligands with MRI CA application (for the appropriate complexes see Table 1.)

The outer-sphere solvent molecules randomly diffusing in the surroundings of the paramagnetic centre also experience the paramagnetic relaxation rate-enhancing effect (Figure 4).

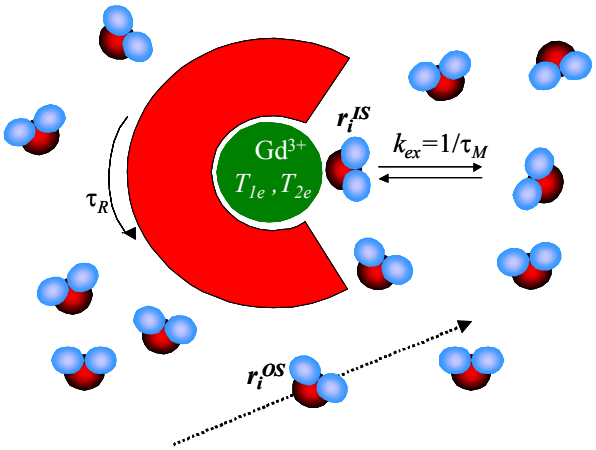


**Figure 4.** Schematic representation of the parameters affecting the relaxivity of contrast agents

### 2.1.1 Inner-sphere contribution

The inner-sphere proton relaxivity is a result of chemical exchange reaction between the coordinated water protons and the bulk. In this two-site exchange reaction, the bulk is the more populated and therefore the only observable site; the relaxation rate enhancement is measured at this bulk water signal. The longitudinal and transverse inner-sphere relaxation rates are described by Eq. 2.3 and Eq. 2.4.[9,10]

$$\left(\frac{1}{T_{1obs}}\right)^{IS} = \frac{c_{Gd^{3+}} q}{55.5}\left(\frac{1}{T_{1m}+\tau_m}\right) = P_m \frac{1}{T_{1m}+\tau_m} \qquad \text{Eq. 2.3}$$

$$\left(\frac{1}{T_{2obs}}\right)^{IS} = \frac{P_m}{\tau_m}\left[\frac{T_{2m}^{-2} + \tau_m^{-1}T_{2m}^{-1} + \Delta\omega_m^2}{\left(\tau_m^{-1} + T_{2m}^{-1}\right)^2 + \Delta\omega_m^2}\right] \qquad \text{Eq. 2.4}$$

where $c_{Gd3+}$ is the $Gd^{3+}$ concentration in mM, $q$ is the hydration number (the number of bound water molecules per $Gd^{3+}$), $P_m$ is the mole fraction of the bound water, $\tau_m$ is the lifetime of the water molecule in the coordination sphere (the reciprocal water exchange rate, $1/k_{ex}$), $\Delta\omega_m$ is the chemical shift difference between the bound and the bulk water protons, and $1/T_{1m}$ and $1/T_{2m}$ are the longitudinal and transverse proton relaxation rates of the bound water.

$1/T_{1m}$ and $1/T_{2m}$ can be described by the sum of three distinct contributions arising from the dipole-dipole *($1/T_i^{DD}$)*, the scalar coupling *($1/T_i^{SC}$)* and Curie *($1/T_i^{C}$)* mechanisms.

In the case of $Gd^{3+}$-chelates, $1/T_{1m}$ and $1/T_{2m}$ are governed mainly by the dipole-dipole mechanism, which is affected by the reorientation of the nuclear spin-electron spin vector (molecular rotation), by the electron spin relaxation and by the water exchange, according to Eq. 2.5-Eq. 2.8.[11]

$$\frac{1}{T_{im}} = \frac{1}{T_i^{DD}} + \frac{1}{T_i^{SC}}, \qquad where\ i = 1,2 \qquad \text{Eq. 2.5}$$

$$\frac{1}{T_1^{DD}} = \frac{2}{15}\left(\frac{\gamma_I^2 g^2 \mu_B^2}{r_{GdH}^6}\right) S(S+1)\left(\frac{\mu_0}{4\pi}\right)^2 \left(7\frac{\tau_{c2}}{1+\omega_s^2\tau_{c2}^2} + 3\frac{\tau_{c1}}{1+\omega_I^2\tau_{c1}^2}\right)$$

Eq. 2.6

$$\frac{1}{T_2^{DD}} = \frac{1}{15}\left(\frac{\gamma_I^2 g^2 \mu_B^2}{r_{GdH}^6}\right) S(S+1)\left(\frac{\mu_0}{4\pi}\right)^2 \left(13\frac{\tau_{c2}}{1+\omega_s^2\tau_{c2}^2} + 3\frac{\tau_{c1}}{1+\omega_I^2\tau_{c1}^2} + 4\tau_{c1}\right)$$

Eq. 2.7

$$1/\tau_{ci} = 1/\tau_R + 1/T_{ie} + k_{ex}, \text{where } i = 1,2$$ Eq. 2.8

$\gamma_I$ is the nuclear gyromagnetic ratio, $g$ is the electron $g$-factor, $\mu_B$ is the Bohr magneton, $r_{GdH}$ is the electron spin-proton distance and $\omega_I$ and $\omega_S$ are respectively the nuclear and the electron Larmor frequencies. $\tau_R$ is the rotation correlation time, $T_{1e}$ and $T_{2e}$ are the longitudinal and transverse electron spin relaxation times of the metal ion, respectively.

The contribution of scalar or contact mechanism to the inner-sphere relaxation rates is very small in the case of the monomeric $Gd^{3+}$ complexes. It is modulated only by the electron spin relaxation and the water exchange rate, as it is given in Eq. 2.9-Eq. 2.11.[12]

$$\frac{1}{T_1^{SC}} = \frac{2S(S+1)}{3}\left(\frac{A}{\hbar}\right)^2 \left(\frac{\tau_{e2}}{1+\omega_s^2\tau_{e2}^2}\right)$$ Eq. 2.9

$$\frac{1}{T_2^{SC}} = \frac{S(S+1)}{3}\left(\frac{A}{\hbar}\right)^2 \left(\frac{\tau_{e2}}{1+\omega_s^2\tau_{e2}^2} + \tau_{e1}\right)$$ Eq. 2.10

$$1/\tau_{ei} = 1/T_{ie} + k_{ex}, \text{where } i = 1,2$$ Eq. 2.11

$A/\hbar$ is the hyperfine (scalar) coupling constant between the electron of the paramagnetic ion and the proton nuclei of the coordinated water.

Electronic relaxation rates also depend on the magnetic field. For Gd(III)-complexes, Bloembergen, Morgan and McLahlan interpreted the electron relaxation in terms of zero field splitting interactions (Eq. 2.12-Eq. 2.14).[13,14]

$$\left(\frac{1}{T_{1e}}\right)^{ZSF} = 2C\left(\frac{1}{1+\omega_S{}^2\tau_v{}^2}+\frac{4}{1+4\omega_S{}^2\tau_v{}^2}\right) \qquad \text{Eq. 2.12}$$

$$\left(\frac{1}{T_{2e}}\right)^{ZSF} = C\left(\frac{5}{1+\omega_S{}^2\tau_v{}^2}+\frac{2}{1+4\omega_S{}^2\tau_v{}^2}+3\right) \qquad \text{Eq. 2.13}$$

$$C = \frac{1}{50}\Delta^2\tau_v\left\{4S(S+1)-3\right\} \qquad \text{Eq. 2.14}$$

The Curie or susceptibility mechanism has significant contribution to the overall relaxivity when $\tau_R$ is at least four orders of magnitude larger than $T_{ie}$, at high magnetic field and mainly in $r_2$. Superparamagnetic nanoparticles having high Curie-contribution act as $T_2$-reducing agents at high field.[15] For Dy(III)-DTPA derivatives characterised by very short $T_{ie,}$ Vander Elst *et al.* showed experimental evidence of the Curie mechanism even in longitudinal relaxation.[16]

The Curie mechanism is based on the dipolar interaction between the nuclear spin and the large static magnetic moment arising from the electrons, as it was first described by Gueron.[17] It is modulated by the rotational correlation time and the chemical exchange, as it is shown by Eq. 2.15-Eq. 2.17.[16]

$$\frac{1}{T_1^C} = \frac{2}{5}\left(\frac{\mu_0}{4\pi}\right)^2 \gamma_I{}^2 B_0{}^2 \mu_B{}^4 g^4 S^2 (S+1)^2 \frac{1}{r^6} \frac{1}{(3k_B T)^2} \left[\frac{3\tau_{CC}}{1+\omega_I{}^2 \tau_{CC}{}^2}\right]$$

Eq. 2.15

$$\frac{1}{T_2^C} = \frac{1}{5}\left(\frac{\mu_0}{4\pi}\right)^2 \gamma_I{}^2 B_0{}^2 \mu_B{}^4 g^4 S^2 (S+1)^2 \frac{1}{r^6} \frac{1}{(3k_B T)^2} \left[4\tau_{CC} + \frac{3\tau_{CC}}{1+\omega_I{}^2 \tau_{CC}{}^2}\right]$$

Eq. 2.16

$$1/\tau_{CC} = 1/\tau_R + k_{ex}$$

Eq. 2.17

### 2.1.2 Outer-sphere contribution

The outer-sphere contribution to the relaxation enhancement is the result of the dipolar interaction between the paramagnetic centre and the water molecules diffusing around it. The most commonly used model for describing the outer-sphere mechanism is based on the Freed-equations (Eq. 2.18-Eq. 2.19).[18,19]

$$r_1^{OS} = \left(\frac{32\pi}{405}\right)\left(\frac{\mu_0}{4\pi}\right)^2 \gamma_I{}^2 \gamma_H{}^2 \hbar^2 S(S+1) \frac{N_A}{aD} \left[3J(\omega_H, T_{1e}) + 7J(\omega_S, T_{1e})\right]$$

Eq. 2.18

$$J\left(\omega, T_{je}\right) = \mathrm{Re}\left[\frac{1+\frac{1}{4}\left(i\omega\tau_d + \frac{\tau_d}{T_{je}}\right)^{1/2}}{1+\left(i\omega\tau_d + \frac{\tau_d}{T_{je}}\right)^{1/2} + \frac{4}{9}\left(i\omega\tau_d + \frac{\tau_d}{T_{je}}\right) + \frac{1}{9}\left(i\omega\tau_d + \frac{\tau_d}{T_{je}}\right)^{3/2}}\right]$$

Eq. 2.19

$$j = 1,2;\ \tau_d = \frac{a^2}{D}$$

## *2.2 Chemical Exchange Saturation Transfer (CEST) contrast agents*

Magnetisation transfer in MRI context was first used by Balaban *et al*.[20] They performed a magnetisation transfer experiment by selective saturation of urea, and they found a significant loss in the intensity of the tissue proton signal. They demonstrated that image contrast could also be altered by applying a frequency-selective radiofrequency pulse at the resonance frequency of an NH or OH group of an intrinsic amino acid, sugar, nucleotide or other metabolite molecule prior to collection of imaging data.[21]

Slow water exchange could be a serious weakness for $Gd^{3+}$-based MRI CAs. This disadvantage can be turned into an advantage for the new type of MRI CAs based on chemical exchange saturation transfer. In these contrast agents the paramagnetic centre is a lanthanide other than $Gd^{3+}$. As a consequence of the low water exchange rate and the large paramagnetic shift on the bound water ("slow exchange region") in these lanthanide complexes, it is possible to accomplish selective saturation transfer from the lower populated site (the coordinated water) to the bulk water signal, therefore to alter its intensity.

Zhang *et al.* gave detailed description about the CEST effect of DOTA-tetraamides.[22-24]

In the case of amidic protons of DOTA-tetraamides similar CEST relevance was observed.[25-27]

## *2.3 Particulate paramagnetic contrast agents*

Since the very beginning of using MRI CAs, need has risen for MRI contrast agents that can be administered orally and can be used to enhance the MRI image of the gastrointestinal (GI) tract. Insoluble particulates as Gd(III)-loaded zeolites,[28-30] clays containing Mn(II) or Gd(III),[31-33] or porous, and also particulate ion exchange resins with paramagnetic ions bound to their surface[34,35] were investigated.

For magnetic resonance angiography, small paramagnetic particulates are possible to use as CAs. They remain in the vascular system for longer time than the Gd(III)-complexes due to their slower clearance through the renal system, providing sufficient contrast for longer measurements. Nanosized Gd(III)-loaded zeolites,[36] metal-loaded nanoparticles with core-shell morphology,[37] and also colloidal particles prepared by specific phase organization of ampiphilic Gd(III)-chelates with cholesterol[38] were suggested for this purpose.

## *2.4 Metal complexes as CT contrast agents*

Metals, metal oxides, metal salts, or metal particulates with high mass attenuation coefficients were widely used as x-ray contrast agents from the very beginning of the practical radiology. The first radiograph of a bismuth-

enhanced segment of the gastrointestinal (GI) tract was made in 1897, using 5% suspension of bismuth subnitrate. Other metal salts and oxides such as CsCl, $ThO_2$, $Gd_2O_3$ and $Dy_2O_3$ also had several applications, but, because of their poor elimination profiles and both acute and long-term toxicity issues, today they are succeeded by various heavy metal coordination compounds. The only metal salt remained in clinical use is $BaSO_4$.[1]

The first testing of $Gd(DTPA)^{2-}$ as x-ray contrast agent started by an unexpected x-ray enhancement detected in the urinary tract of a patient, who received Gadovist in an MRI procedure prior to his CT scan. Subsequent studies on $Gd(DTPA)^{2-}$ and other metal complexes such as $Yb(DTPA)^{2-}$, Gd(DTPA-BMA), Gd(HP-DO3A) and Gd(DO3A-butrol) showed comparable or even greater contrast in comparison with equimolar quantities of iodinated contrast agents, mainly at higher tube voltages. They can be used as alternative x-ray CAs to patients with renal insufficiency or allergy to iodinated compounds. The lipophilic EOB-DTPA complexes of $Gd^{3+}$, $Dy^{3+}$ and $Yb^{3+}$ have proved to be efficient CAs for CT of liver and spleen.[39]

Bi(III)-complexes such as $Bi(DTPA)^{2-}$ and Bi(III)-tartrate were also investigated *in vivo* on animals as CT contrast agents. Although both of them showed diagnostically useful features ($(Bi(DTPA)^{2-}$ in angiography, Bi(III)-tartrate in imaging of the liver, kidney and spleen), toxicity and solubility problems call for further search for Bi(III)-complexes with more favourable biodistribution.[1]

## 2.5 Structure and dynamics of DTPA and DOTA lanthanide complexes

The Gd(III)-based MRI contrast agents function through catalytically relaxing water protons. The achieved relaxivity enhancement allows the CAs to be administered at a lower dose. Relaxivity depends on the electronic properties of the ion, the number of the water molecules in the inner coordination spheres, the ion-hydrogen distance and the mean lifetime of these water molecules in the inner-sphere, and the rotational correlation time of the complex (Section 2.1). Each of these parameters is related to the solution structure and intra/or intermolecular dynamics of the complex concerned. The electronic relaxation rate of the $Gd^{3+}$ ion, $1/T_{ie}$ is strongly related to the flexibility of the complex. The water exchange rate, $k_{ex}$ between the bound water and the bulk is dependent on the overall charge and on the steric strain around the water molecule. The rotation correlation time, $\tau_R$ is determined by the tumbling motion of the molecule. Therefore, elucidation of solution structure and dynamics of these complexes is indispensable for understanding the obtained results and for further developments in this field.

Major methods in this field are NMR spectroscopy and luminescence. X-ray crystallography provides a strong support by means of the corresponding solid-state structures.

$Gd^{3+}$-complexes, due to their intensive paramagnetism causing signal broadening, cannot be easily studied by NMR spectroscopy. However, it is common for a ligand to form nearly isostructural complexes within the lanthanide series.[40]

The $Ln^{3+}$ ions have unique properties in the periodic system. The first and last member, $La^{3+}$ and $Lu^{3+}$ are diamagnetic, the others, with 1-7 unpaired *4f* electrons, are paramagnetic. The *4f* electrons are shielded by the *5s* and *5p* electrons. Therefore, they are not readily available for covalent interactions with ligands, and, as a consequence, the $Ln^{3+}$ ions have very similar chemical behaviour. The differences in chemical behaviour can be attributed to the decrease in ionic radius from $La^{3+}$ to $Lu^{3+}$ (1.216 Å-1.032 Å).[41]

Owing to their large size, lanthanides tend to favour high coordination numbers in aqueous media. Until now, all $Gd^{3+}$-complexes approved for use in MRI are nine-coordinate complexes, in which a ligand occupies eight binding sites and the ninth coordination site is occupied by a water molecule.

### 2.5.1 Structure and dynamics of $Ln(DTPA)^{2-}$ complexes

X-ray structures for $Ln(DTPA)^{2-}$ complexes showed a nine-coordinated metal ion bonded to three nitrogens and five monodentate carboxylate oxygen atoms of the DTPA ligand, as it is illustrated in Figure 5. In most cases, the geometry is best described as a distorted tricapped trigonal prism. The ninth coordination place is usually occupied by a coordinated water molecule, however, dimeric structure is also known for $Gd(DTPA)^{2-}$, where the coordinated water is substituted by an oxygen atom of a bidentate carboxylate group from the neighbouring complex.

The solution structure was consistent with the crystallographic results, showing nonadentate coordination, as it was deduced from lanthanide induced relaxation rate (LIR) enhancements of the $^{13}C$ nuclei in the $Nd^{3+}$

complex.[42] Lanthanide induced $^{17}O$ chemical shifts (LIS) indicated one coordinated water molecule in the lanthanide complexes.

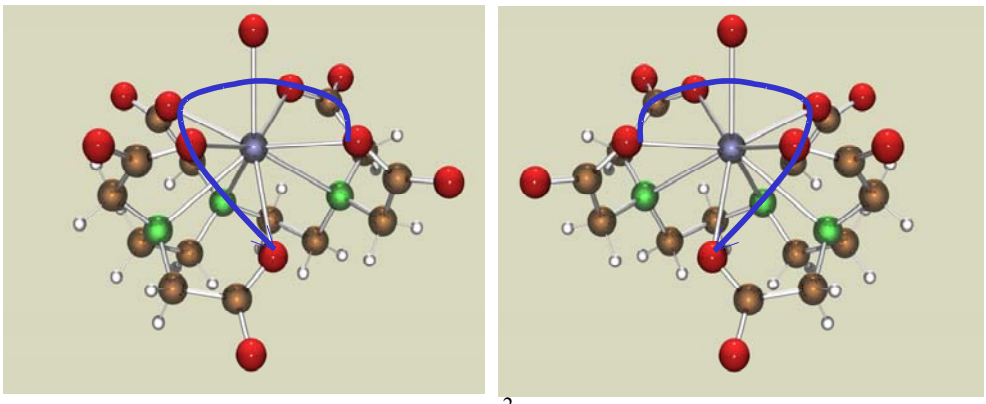

**Figure 5.** X-ray structure of $Eu(DTPA)^{2-}$ (ball and stick representation) showing the two different arrangements of the acetate arms in the enantiomers

The intramolecular dynamics showed interesting features both in the $^{13}C$ and $^{1}H$ NMR spectra. At 21 $^{o}C$, the $^{13}C$ NMR spectra of $Nd(DTPA)^{2-}$ showed six broad signals while two resonances (the middle acetate $-CH_2-$ and $-COO^-$ carbon signals) did not show any broadening. Increasing the temperature to 73 $^{o}C$ resulted in a significant sharpening of the broad signals. That was explained by exchange phenomena related to the conformational mobility of the complex. The number of signals expected in static situation, according to the low-symmetry x-ray structure is 14. The number of signals detected (8) at 73 $^{o}C$ indicates that the exchange phenomena result in an effective mirror plane through the middle nitrogen atom and through the the middle acetate $-CH_2-$ and $-COO^-$ carbons which were always very sharp regardless to the temperature.[42]

By means of $^{1}H$ two-dimensional (2D) exchange spectroscopy (EXSY), the solution dynamics of $Pr(DTPA)^{2-}$, $Eu(DTPA)^{2-}$ and $Yb(DTPA)^{2-}$ was investigated.[43] Raising the temperature caused the number of $^{1}H$ resonances to decrease from 18 to 9, consistent with exchange between two enantiomers (Figure 6). The helical chirality of the complex arises from the coordination of the carboxylate moieties. The intramolecular exchange (enantiomerisation) involves the change in this helical chirality and the flip-flop motion of the ethylene-diamine backbones.

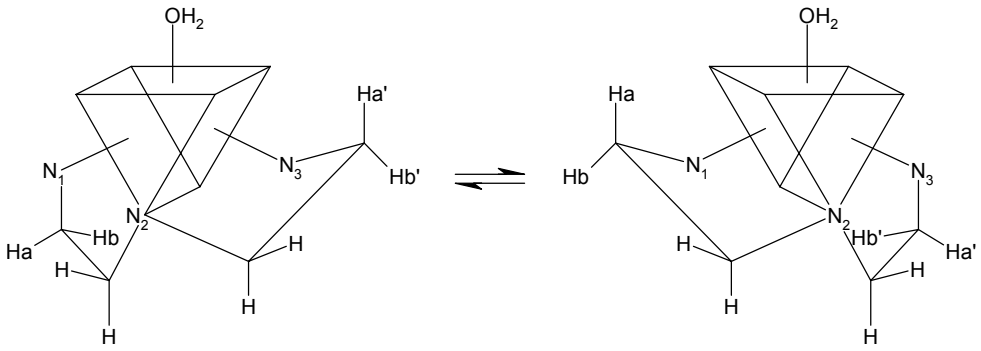


**Figure 6.** Exchange between two enantiomers in $Ln(DTPA)^{2-}$ complexes

The exchange rate between the two enantiomers for $Eu(DTPA)^{2-}$ is around 1500 $s^{-1}$ at 298 K and the activation parameters are $\Delta H^{\neq} = 38.5 \pm 2.4$ $kJmol^{-1}$ and $\Delta S^{\neq} = -56.8 \pm 7$ $Jmol^{-1}K^{-1}$.

The water exchange rate between the coordinated water in $[Gd(DTPA)(H_2O)]^{2-}$ and bulk water was determined by variable temperature $^{17}O$ NMR and was found to be $k_{ex}^{298} = (4.1 \pm 0.3) \cdot 10^{6}$ $s^{-1}$. Dissociative mechanism was suggested based on the obtained positive activation volume

($\Delta V^{\neq}$ = 12.5 ± 0.2 $cm^3mol^{-1}$) and the large activation enthalpy ($\Delta H^{\neq}$ = 52.0 ± 1.4 $kJmol^{-1}$) and positive activation entropy ($\Delta S^{\neq}$ = 56.2 ± 5 $Jmol^{-1}K^{-1}$).[44]

### 2.5.2 Structure and dynamics of $Ln(DOTA)^-$ complexes

DOTA is an octacoordinated ligand based on the tetraazadodecane ring in which each nitrogen atom bears an acetic substituent. The four nitrogens and four oxygens wrap around a lanthanide ion, resulting in high thermodynamic and kinetic stability.

It was early shown that the $Ln(DOTA)^-$ complexes can adopt either a square-antiprismatic (SA) or an alternative twisted square antiprismatic (TSA) geometry. The SA and TSA arrangements differ mainly in the twist angles between the planes formed by the coordinated N (basal plane) and O (capping plane) atoms, with ca $40^o$ for the SA and ca $-30^o$ for the TSA geometry. Both TSA and SA geometries exist as pairs of enantiomeric structures. Structures either with eight- or nine-coordinated lanthanides (where the ninth coordination site is occupied by a water molecule) can be found in both cases. Among the crystallographic data reported on $Ln(DOTA)^-$ family until now, eight refer to SA geometry with nine-coordinated lanthanides, two to the TSA type with nine-coordinated lanthanides and one each to the eight-coordinated SA and TSA structures.[45] All arrangements show $C_4$ symmetry in the complexes (Figure 7).

A thorough NMR study on the DOTA complexes of the lanthanide series showed that the four possible arrangements (TSA and SA enantiomer pairs) could coexist and interconvert in solution.[46-51]

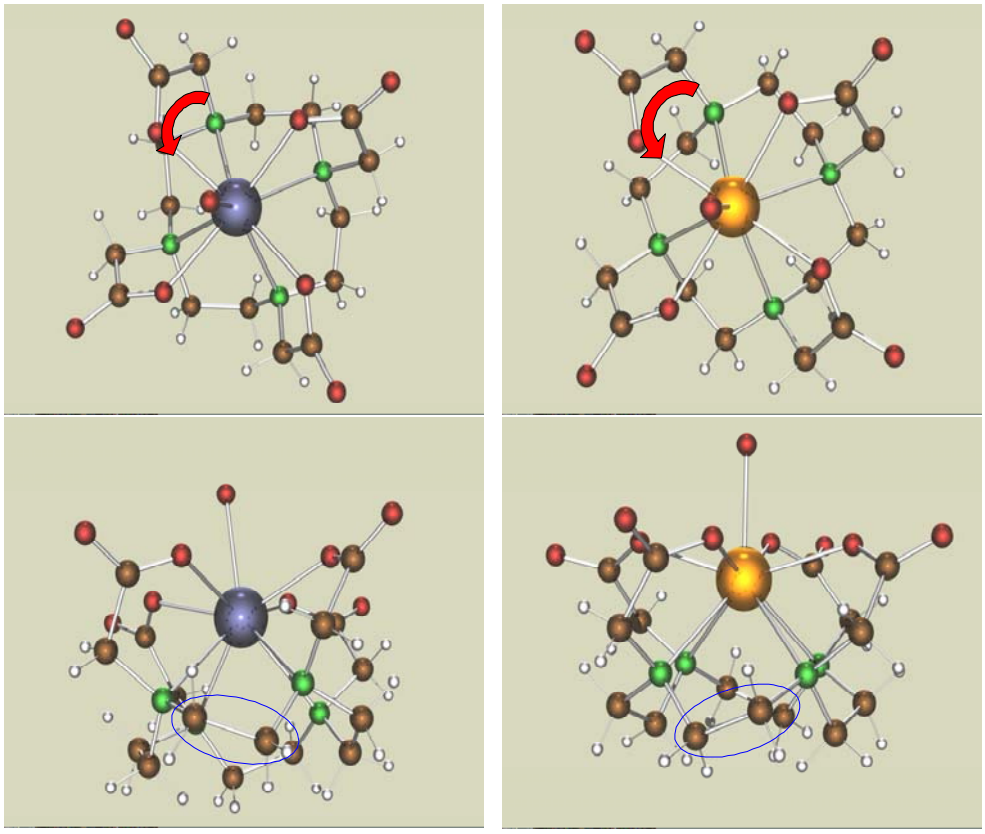

**Figure 7.** X-ray structure of Ce(DOTA)$(H_2O)^-$ (TSA, left) and Nd(DOTA)$(H_2O)^-$ (SA, right)

The ratio between the interconverting isomers in equilibrium is strongly dependent on the ionic radius of the lanthanide ion. Larger lanthanide ions, such as $La^{3+}$, prefer the TSA arrangement, while smaller lanthanide ions favour the SA geometry (Figure 8).[51-53]

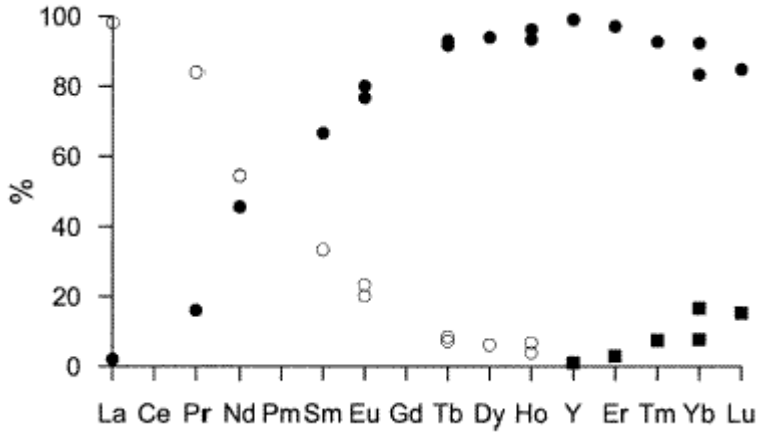


**Figure 8.** Ionic radius-dependent isomeric ratio of Ln(DOTA)$^-$ complexes along the lathanide series. ● nine-coordinated square-antiprismatic, ○ nine-coordinated inversed-square-antiprismatic and ■ eight-coordinated inversed-square-antiprismatic arrangements [53]

In the Ln(DOTA)$^-$ complexes two types of helical chirality appear: one belongs to the tilt of the ethylene bridges in the macrocycle (δ or λ), and the other belongs to the acetate arms' helicity Δ or Λ) upon coordination to the lanthanide ion. Consistent with the $C_4$ symmetry, all of the ethylene bridges adopt the same conformation and the same is true for the acetate arms. Consequently, each geometry consists of two enantiomers; Δ-*(λλλλ)* and Λ-*(δδδδ)* correspond to the SA, while Λ-*(λλλλ)* and Δ-*(δδδδ)* to the TSA arrangement.

Extensive VT $^1$H and $^{13}$C NMR studies demonstrated that the intramolecular exchange between the existing diastereomers could follow two different pathways: *i)* by a twist along the $C_4$ axis of the four oxygen-plane relative to

the four nitrogen-plane, resulting in Δ↔Λ interconversion, or *ii)* by a sequential flip of the ethylene bridges without changing the acetate arms' layout (δ↔λ). Enantiomerisation involves both rearrangements in a concerted or a stepwise fashion. For Ln= Ho, Er, Tm, Yb and Lu, a water coordination-decoordination equilibrium is superimposed on the intramolecular rearrangements (Figure 9). The exchange between enantiomers was found to occur with similar rate as the exchange between diastereomers in $Yb(DOTA)^-$ by means of quantitative $^1H$ EXSY spectroscopy.[49] In the Lu(DOTA)- complex, the enantiomerisation ($k_e^{298}$ = 18 $s^{-1}$ , $\Delta H_e^{\neq}$ = 100.5 ± 0.6 $kJmol^{-1}$ and $\Delta S_e^{\neq}$ = 116.0 ± 2 $Jmol^{-1}K^{-1}$) was found to take place much slower than the exchange between diastereomers ($k_d^{298}$ = 340 $s^{-1}$ , $\Delta H_d^{\neq}$ = 54.4 ± 1 $kJmol^{-1}$ and $\Delta S_e^{\neq}$ = -14.1 ± 3.5 $Jmol^{-1}K^{-1}$); however, the authors do not discriminate whether this exchange between diastereomers, involving either the conformational inversion of the ring or the reorientation of the acetate arms, has the same or different rate and activation parameters.[50]

The water exchange rate between the coordinated water in $[Gd(DOTA)(H_2O)]^-$ and bulk water was determined by variable temperature $^{17}O$ NMR and was found to be $k_{ex}^{298}$ = (4.8±0.4) · $10^6$ $s^{-1}$. The dissociative mechanism was supported by the positive activation volume ($\Delta V^{\neq}$ = 10.5 ± 0.2 $cm^3mol^{-1}$) and the large activation enthalpy ($\Delta H^{\neq}$ = 48.8 ± 1.6 $kJmol^{-1}$) and the positive activation entropy ($\Delta S^{\neq}$ = 46.6 ± 6 $Jmol^{-1}K^{-1}$), similarly to $[Gd(DTPA)(H_2O)]^{2-}$.[44]

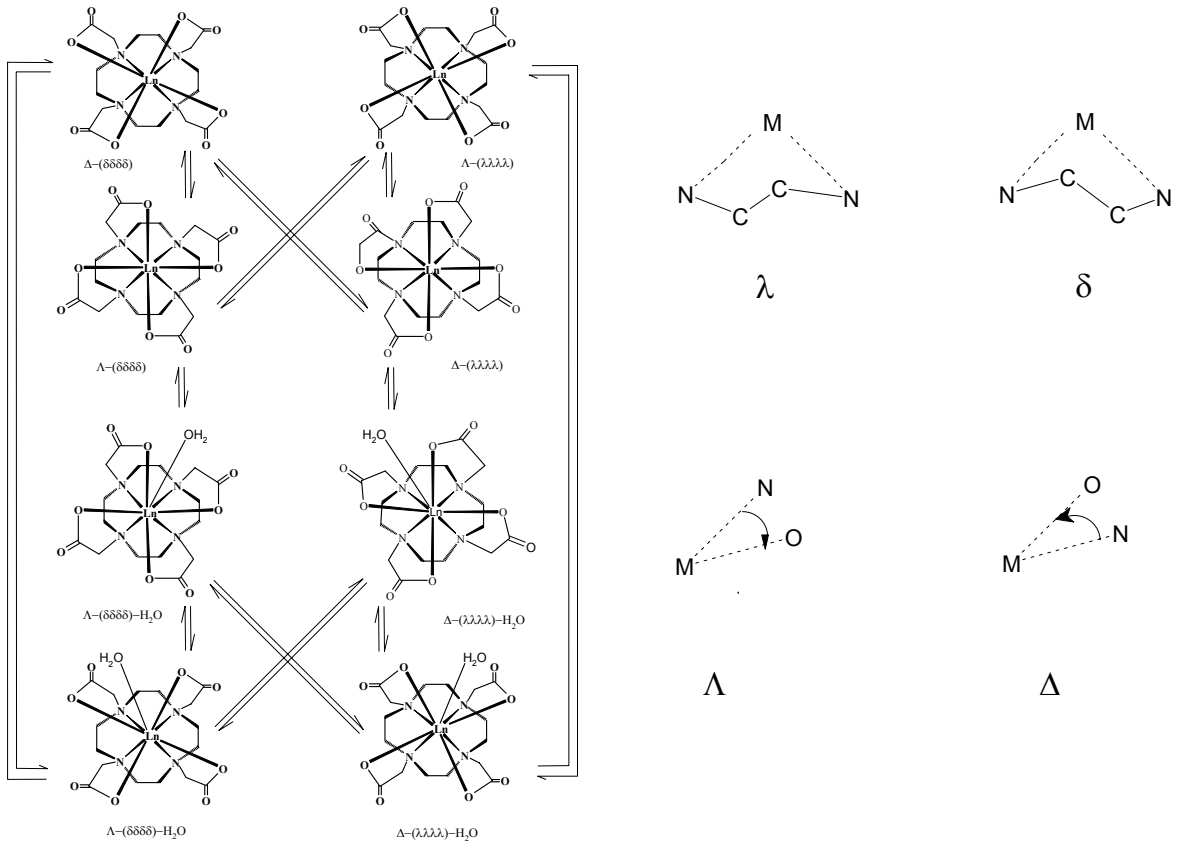


**Figure 9.** Schematic representation of the general equilibrium system and the available dynamic processes in the case of Ln(DOTA)- complexes(left) and chirality appearing in DOTA ring and acetate arms' helicity (right)

# 3 Structure and dynamics of Bi(DOTA)$^-$ and K($H_x$DOTA)$^{(3-x)-}$ complexes (x=0-4)

## *3.1 Introduction*

The ionic-radius dependent isomeric composition of Ln(DOTA)$^-$ complexes along the lanthanide series and the interconversion reactions among them were discussed in the Bibliographic review. Recent works have attempted to unravel the connection between these fluxionalities and the water-exchange rate of the individual isomers, which is important for applying these complexes as MRI contrast agents.[54-56] As an example, studies on [Eu(DOTAM)($H_2O$)]$^{3+}$ (DOTAM = 1,4,7,10-tetrakis(carbamoylmethyl)-1,4,7,10-tetraazacyclododecane) showed that at 298 K the TSA isomer has 40 times higher water exchange rate than the SA isomer. It was observed that one SA $\rightarrow$ TSA interconversion happens every two to three exchanges of a water molecule on the SA isomer.[55] Since the isomeric composition is strongly dependent on the ionic radius of the coordinated lanthanide ion, a sharp dependence of water exchange rate versus lanthanide ionic radii was found for various DOTA-tetraamide complexes.[56]

The formation of Ln(DOTA)$^-$ complexes is exceptionally slow and the kinetics shows interesting features.[57] [58-64]. Unusually stable intermediates were detected by spectrophotometry,[57,61] $^1$H-NMR[58] and luminescence spectroscopy.[62] The composition and structure of these intermediates were disputed for some time,[60,65] but an agreement seems to be emerging; namely

accepting the formation of a diprotonated complex, in which the $Ln^{3+}$ has an "out of cage" position, while two nitrogen donors are protonated.[61,62,64] The $[Eu(H_2DOTA)]^+$ intermediate contains four or five water molecules coordinated to $Eu^{3+}$, revealed by luminescence lifetime studies. [62] The lifetime of these intermediates is so long that even the stability constants could be determined by direct spectrophotometry and pH-potentiometry[61,62] beyond the kinetic methods.[58,62]

In this work we continue to search that in what extent the DOTA ligand itself is responsible for the intramolecular motions of the metal - DOTA complexes and what is the new feature brought about by the formed complex, which is a special assembly of the metal ion and the ligand. In the case of $Bi(DOTA)^-$, a potential CT contrast agent, the isomeric composition has been studied and compared with the results obtained for the $Ln(DOTA)^-$ complexes. By VT $^1H$ NMR spectroscopy, the dynamic behaviour of the complex has also been revealed.

On the one hand, when the pH dependence of the NMR spectra is studied, the application of alkali metal ions is not suitable because the potentiometric studies indicated interaction between DOTA and $Na^+$ or $K^+$.[66,67] On the other hand, the study of interaction between the alkali metals and DOTA may lead to interesting results because at least one condition, the kinetic inertness for metal ion exchange does not exist any more. Previous studies on alkali metal complexes of other tetraaza macrocyclic ligands (1,4,7,10-tetrakis(2-hydroxyethyl)-1,4,7,10-tetraazacyclododecane (thec12) and 1,4,7,10-tetrakis(2-methoxyethyl)-1,4,7,10-tetraazacyclododecane (tmec12)) were made to investigate the intramolecular (macrocyclic internal motion or

fluxionalities) and intermolecular (ligand-complex) exchange processes in non-aqueous media. While in the case of $[Li(thec12)]^+$ and $[Na(thec12)]^+$, the intramolecular exchange was found to be faster than the intermolecular one, in the case of $[K(thec12)]^+$, the similarity of the activation parameters showed consistency with the assumption that the intermolecular ligand exchange is the dominant enantiomerisation mechanism.[68,69]

In the case of DOTA ligand, in the absence of metal ions, using tetra-methyl-ammonium counter cation, all events have been found to be too fast for detection. At pH<1, where mainly the $H_6DOTA^{2+}$ is present in solution, the full protonation leads to slower fluxionality of the ligand, however, even at lower temperature, no scalar couplings could be detected.[70] Here we show that using $K^+$ ions, the formed labile complexes have had slower fluxionality and therefore have provided information about the structure through the scalar coupling constants. Moreover, some interesting new dynamic properties have been found, which probably helps to find out more about the nature of the solution behaviour of the important DOTA ligand.

## *3.2 Experimental*

### 3.2.1 Materials

The ligand was kindly provided by Guerbet (Roissy, France). The concentration of the ligand stock solution for preparing $Bi(DOTA)^-$ was determined by pH-potentiometric titration in the absence and presence of $Ca^{2+}$ excess; while we used weighted amounts of the ligand for the NMR titration resulting $K(H_xDOTA)^{(3-x)-}$.

The chemicals used for preparing the complexes were of analytical grade. $Bi(ClO_4)_3$ solution was prepared by dissolving $Bi_2O_3$ (99.9%, Fluka) in excess $HClO_4$. The concentration of the $Bi(ClO_4)_3$ solution was determined by complexometry with the use of standardized $Na_2H_2EDTA$ solution and xylenol orange as indicator at about pH 1. KOD and $(CH_3)_4NOD$ (TMAOD) solutions were made by dissolving weighted amounts of chemicals and $D_2O$.

**Na[Bi(DOTA)]** The 0.2 M solution of the complex Na[Bi(DOTA)] was prepared by the reaction of equivalent amounts of $Bi(ClO_4)_3$ and the ligand. To the vigorously mixed solution of $Na_4DOTA$, $Bi(ClO_4)_3$ solution was added dropwise. The pH of the solution was controlled, and it was set to 5-5.5. To the final solution 20% $D_2O$ was added, and the pH was adjusted to 8.6.

**$K(H_xDOTA)^{(3-x)-}$** The $K(H_xDOTA)^{(3-x)-}$ species were studied by NMR titration of the 0.1 M ligand solution in $D_2O$ with concentrated KOD solution. The change of the total concentration of DOTA was negligible. The pH was measured by a combined glass electrode with a Hanamed pH meter. The read values +0.4 were accepted as pH.[71] As a control measurement, NMR titration of the ligand was also performed with TMAOD.

### 3.2.2 Methods

The $^1H$ and $^{13}C$ NMR measurements were performed on Bruker AM 360 NMR and Bruker DMX 500 spectrometers in locked mode.

The chemical shifts were referenced to TMS*. The temperature was regulated by Eurotherm equipment, fitted to the spectrometer. The temperature was corrected by using methanol chemical shifts according to literature.[72] The $^{13}C$

NMR spectra were recorded in J-modulated decoupling or inverse gated decoupling mode, depending on the need for getting quantitative spectrum. Typical pulse width corresponded to 30° flip angle and 10-15 s relaxation delays were used in order to use the signal integrals determination of quantitative concentration of $^{1}H$ spectra.

The $^{1}H$-$^{1}H$ COSY spectra were made with the standard Bruker program, using 45º mixing pulse. The $^{1}H$-$^{13}C$ correlation spectra were recorded on Bruker DMX 500 spectrometer in inverse mode, using gradient pulses in the *z* direction with the usual Bruker HSQC pulse sequence. Data processing was made by Bruker WinNMR software package. The line widths were determined by deconvolution, fitting Lorentz curves on the peaks.

## *3.3 Results and Discussion*

### 3.3.1 $^{1}H$ and $^{13}C$ NMR studies on Bi(DOTA)$^{-}$

The $^{1}H$ NMR spectrum of Bi(DOTA)$^{-}$ consists of broad peaks at room temperature; these peaks broaden with increasing temperature. Since the equilibrium studies and the single crystal x-ray diffraction results indicated the presence of only one type of complex in solid state and in solution (Figure 10)[73], the broadening of the signals was considered as a consequence of fluxional dynamic processes, which are fairly common for DOTA complexes.[46,48-50,52]

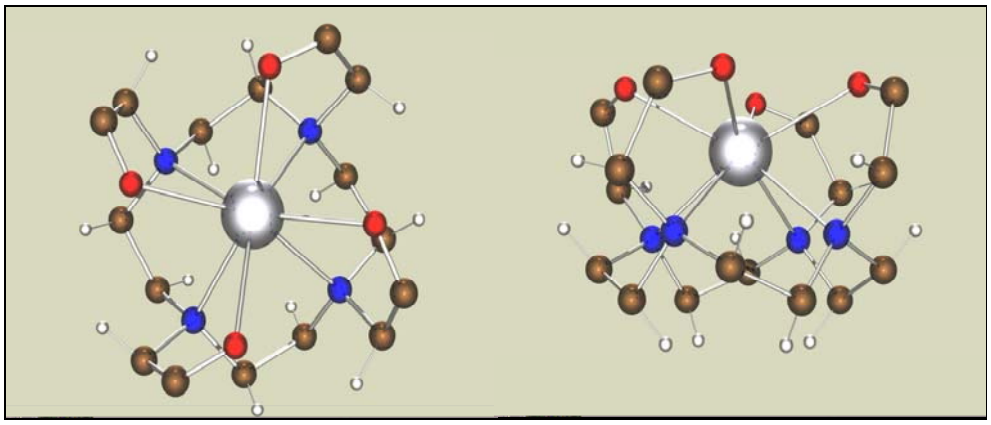

**Figure 10.** X-ray structure of Na[Bi(DOTA)](ball and stick representation) showing TSA ( Δ–δδδδ) arrangement

In order to acquire more information about the structure and dynamics of the complex, we first assigned the $^{1}H$ and $^{13}C$ NMR peaks on the basis of 2D $^{1}H$-$^{1}H$ COSY and $^{1}H$-$^{13}C$ HSQC at 274 K, where the $^{1}H$-$^{1}H$ coupling patterns are well visible (Figure 11).

The number of signals indicates that the complex itself has $C_4$ symmetry in solution, in the same way as in the crystalline form, where the $Bi^{3+}$ is coordinated by four nitrogen and four carboxylate oxygen donor atoms, without coordinated water. In contrast with most $Ln(DOTA)^{-}$ complexes, no other diastereomer was detected. This supports the previous observations establishing that the diastereomeric composition is dependent on the ionic radius.[51] The $Bi^{3+}$ (eight-coordinated, 1.17 Å),[41] therefore, behaves similarly to the larger lanthanides such as $La^{3+}$ (nine-coordinated, 1.216 Å); having one preferred arrangement, which is, according to the x-ray structure, the TSA geometry.

At 274 K the ring exhibits four proton signals (Table 2).

**Table 2.** $^{1}$H NMR data for Bi(DOTA)$^{-}$

| $^{1}$H signal label | δ (ppm) | $^{2}J_{HH}$, $^{3}J_{HH\ (Hz)}$ |
|---|---|---|
| $r_1H(a)$ | 3.75 | $^{2}J_{HH}\{r_1H(a)\text{-}r_1H(b)\} = -14.2$ |
| $r_1H(b)$ | 3.36 | $^{2}J_{HH}\{r_1H(a)\text{-}r_1H(b)\} = -14.2$<br>$^{3}J_{HH}\{r_1H(b)\text{-}r_2H(b)\} = 14.0$ |
| $r_2H(a)$ | 3.63 | $^{2}J_{HH}\{r_2H(a)\text{-}r_2H(b)\} = -13.6$ |
| $r_2H(b)$ | 3.53 | $^{2}J_{HH}\{r_2H(a)\text{-}r_2H(b)\} = -13.6$<br>$^{3}J_{HH}\{r_1H(b)\text{-}r_2H(b)\} = 14.0$ |
| acH(a) | 4.02 | $^{2}J_{HH}\{acH(a)\text{- }acH(b)\} = -17.85$ |
| acH(b)<br>(small intensity because of water suppression) | 4.45 | $^{2}J_{HH}\{acH(a)\text{- }acH(b)\} = -17.85$ |

The staggered conformation is confirmed by the coupling pattern; the detected large vicinal coupling between $r_1H(b)$ and $r_2H(b)$ corresponds to the axial arrangement, while the smaller vicinal coupling between the equatorial $r_1H(a)$ and $r_2H(a)$ protons could not be detected even at 274 K.

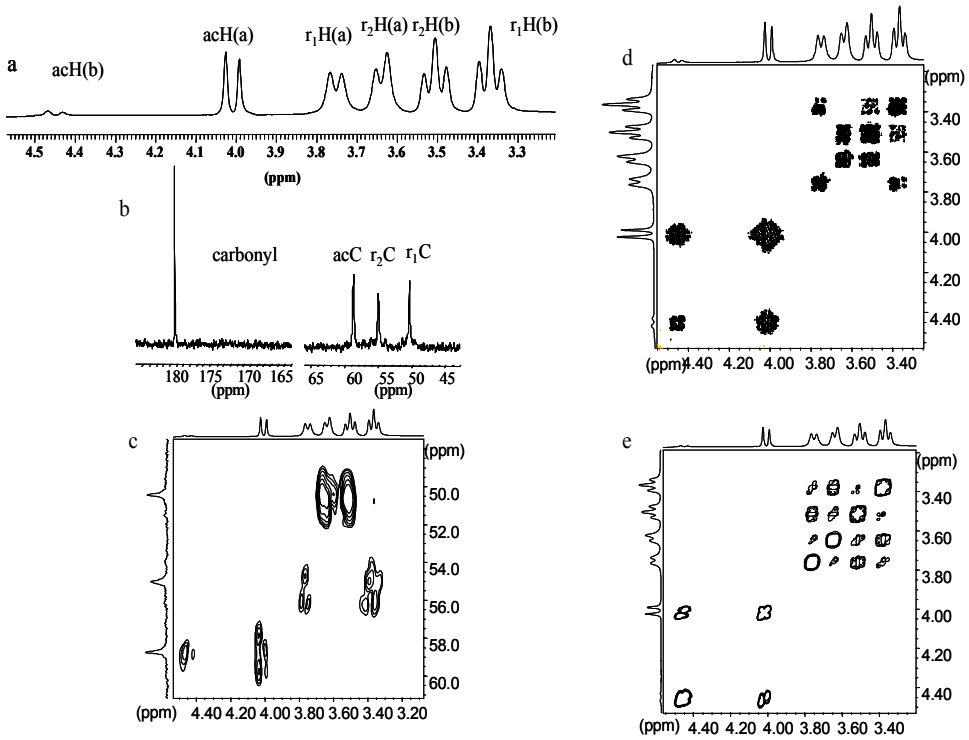


**Figure 11**.a $^{1}H$ NMR b. $^{13}C$ NMR c. $^{1}H$-13C HSQC d. $^{1}H$-$^{1}H$ COSY e. $^{1}H$-$^{1}H$ EXSY spectra of Bi(DOTA)$^{-}$ at 274 K

The acetate protons of $Bi(DOTA)^-$ give an AB doublet pair with an exceptionally large (-17.85 Hz) coupling constant. There is a rule, supported by experimental findings and also quantum mechanical calculations for R-$CH_2$-$COO^-$ fragments, which describes the variation in the $^2J_{HH}$ value with the dihedral angle of the R-C bond and the $COO^-$ plane.[74] If this angle is about 90°, then $^2J_{HH}$ is about –12 Hz, while it is 0° or 180°, then $^2J_{HH}$ can be even –18-–19 Hz. According to this finding, the preferred coordination mode in $Bi(DOTA)^-$ is where the C–N bond is in an eclipsed position to the $COO^-$ plane (Figure 12).

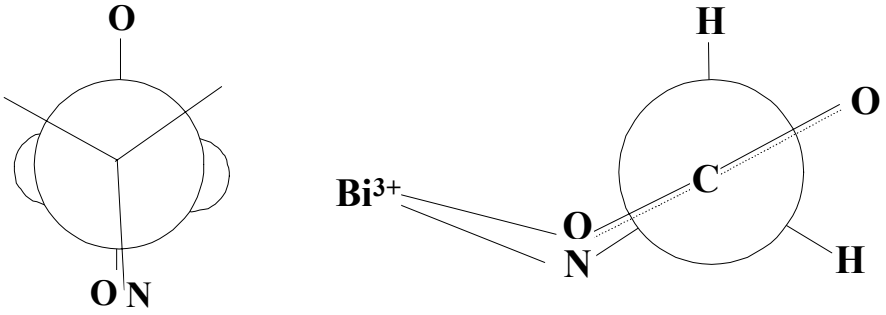


**Figure 12.** Preferred coordination mode in $Bi(DOTA)^-$ (the C–N bond is in an eclipsed position to the $COO^-$ plane)

The $^{13}C$ NMR spectrum of $Bi(DOTA)^-$ at 274 K shows four signals (Table 3).

**Table 3.** $^{13}C$ NMR data for $Bi(DOTA)^-$

| $^{13}C$ signal label | δ (ppm) |
|---|---|
| $r_1C$ | 50.5 |
| $r_2C$ | 55.0 |
| acC | 58.8 |
| carbonyl | 179.1 |

The $C_4$ symmetry is further supported by detecting only one carbonyl signal for the four carbonyl C atoms and one acC signal corresponding to the four acetate-$CH_2$- atoms. The appearance of $r_1C$ and $r_2C$ signals for the ring carbons indicates that there are two different environments for these atoms.

The dynamic behaviour of the protons can be observed qualitatively via the 2D EXSY spectra taken at 274 K (Figure 11). There are strong cross-peaks between the $r_1H(a)$ and $r_2H(b)$ protons and between the $r_1H(b)$ and $r_2H(a)$ protons. These correspond to the motion of the protons originally in the axial position arriving to the equatorial position and *vice versa*, while the $r_1$ and $r_2$ carbon atoms virtually change their position (Figure 13). With the notation introduced for DOTA complexes, this rearrangement is the *(δδδδ)*↔ *(λλλλ)* ring inversion. The existence of the other, weaker cross-peaks is the result of the NOE effect from neighbouring protons; if they arose from exchange processes, those would require the break of the metal-ligand bonds.

The existence of the *(δδδδ)*↔ *(λλλλ)* fluxionality is further supported by the temperature dependence of the $^1H$ NMR spectra (Figure 14). At high temperature, the ring protons collapse to two signals, probably to a “still exchange-broadened” AB doublet pair, in which the geminal coupling could

not be resolved even at this temperature. The temperature dependence of the $^1$H-NMR spectra for the ring protons could be described quantitatively by taking into account only this exchange process. The fluxionality of the ring in the Ln(DOTA)$^-$ complexes was described with this motion as well.[48-52] The AB doublets of the acetate arms broaden and collapse to one signal on elevation of the temperature (Figure 13). This fluxional motion can be attributed to the change of the acetate arms' helicity in Bi(DOTA)$^-$, denoted by $\Delta \leftrightarrow \Lambda$. This type of motion has also been detected in $Ln^{3+}$ complexes.[49] The activation parameters obtained for these motions can be found in Table 4.

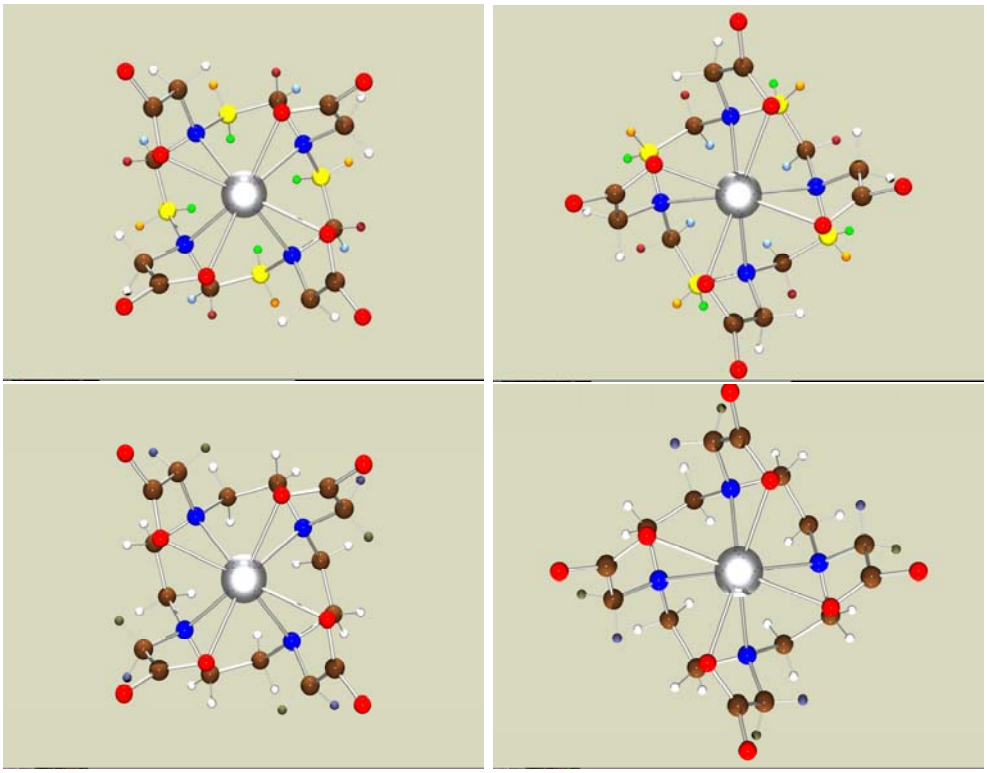

**Figure 13.** $^{1}H$-$^{1}H$ and $^{13}C$-$^{13}C$ exchange processes during the dynamic exchange reaction between the two enantiomers of $Bi(DOTA)^-$
Above: exchange between the ring protons, below: exchange between the acetate -$CH_2$- protons.

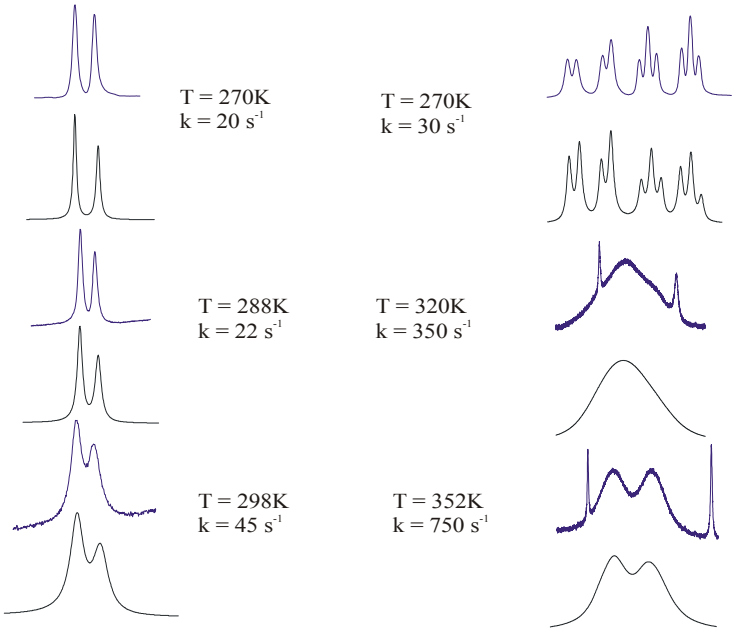


**Figure 14.** Measured (above) and calculated (below) $^{1}$H NMR spectra of Bi(DOTA)$^{-}$ for acetate region (left) and ring (right). The narrow peaks in the ring region are due to the free ligand

**Table 4.** Activation parameters for intramolecular motions in several DOTA complexes

| | $\Delta H^{\#}$ ring inversion kJ mol$^{-1}$ | $\Delta S^{\#}$ ring inversion J mol$^{-1}$ K$^{-1}$ | $\Delta H^{\#}$ ring slewing kJ mol$^{-1}$ | $\Delta S^{\#}$ ring slewing J mol$^{-1}$ K$^{-1}$ | $\Delta H^{\#}$ acetate arms kJ mol$^{-1}$ | $\Delta S^{\#}$ acetate arms J mol$^{-1}$ K$^{-1}$ |
|---|---|---|---|---|---|---|
| Yb(DOTA)$^{-}$[a] | 79 ± 8<br>64 ± 8 | 46 ± 26<br>9 ± 27 | - | - | 80 ± 15<br>66 ± 13 | 49 ± 51<br>14 ± 45 |
| La(DOTA)$^{-}$[b] | 59.4±0.8 | -4.6 ± 3.3 | - | - | - | - |
| Bi(DOTA)$^{-}$ | 40±7 | -76±15 | - | - | 35±6 | –96±20 |
| K(DOTA)$^{4-}$ | 47±1 | -26±24 | 95±7 | 133±24 | 67±3 | 48±10 |

The complex Bi(DOTA)$^-$ has one dominant diastereomer in the solution, which consists of an enantiomer pair denoted as Δ*(λλλλ)*/Λ*(δδδδ)*, according to the IUPAC standard. The concentration of the other Λ*(λλλλ)*/Δ*(δδδδ)* enantiomer pair is so low that we could not even detect the presence of them. Therefore, the exchange observed is as follows:

$$\Delta(\lambda\lambda\lambda\lambda) \rightleftharpoons \Lambda(\delta\delta\delta\delta)$$

The similar activation parameters obtained for the ring inversion and for the change in the acetate arms' helicity support the suggestion of Jacques *et al.* based on $^1$H-$^1$H 2D EXSY measurements on the complex Yb(DOTA)$^-$; that the two types of motions, *i.e.* the motion of the ring and the acetate arms, proceed at the same rate in a concerted way.[49] Another explanation can be a two-step mechanism where the slow, rate-determining ring inversion is followed by a fast change in the acetate arms' helicity.[55] Since the Λ*(λλλλ)*/Δ*(δδδδ)* enantiomer pair cannot be detected, both accounts can be applied to explain our results.

The free energy of activation is smaller than for La(DOTA)$^-$, but the entropy of activation is a larger *negative* value for Bi(DOTA)$^-$. Generally, it is not an easy task to explain the activation parameters for fluxional systems, but some comment can be made. The entropy of activation characterizes the remaining hindrance of a certain process when there is no energetic barrier, which occurs at infinitely high temperature. For La(DOTA)$^-$, it is close to zero,[46] while for Yb(DOTA)$^-$, it is $\Delta S^{\#} = 46 \pm 26$ J mol$^{-1}$ K$^{-1}$.[49] These data were interpreted that in the transition state the Yb(DOTA)$^-$ probably loses one water ligand resulting in increased disorder, while this does not occur for

$La(DOTA)^-$. The entropy of activation for the enantiomerisation reaction of $Lu(DOTA)^-$ is even more positive, 116 J $mol^{-1}$ $K^{-1}$, which is in agreement with the water free transition state concept, although Aime *et al.* did not analyse the reaction from this point of view.[50] The $Bi(DOTA)^-$ has no water in the coordination sphere, and the transition state can be conceived as more symmetrical than either of the reactants or the products, probably as an antiprismatic arrangement, explaining the high negative value for the entropy of activation.

### 3.3.2 pH dependence of $^1$H NMR spectrum of $K(H_xDOTA)^{(3-x)-}$ system

The NMR spectrum of 0.1 M $H_4$DOTA solution in $D_2O$ (pH after dissolution is 3.5) consists of three peaks. One belongs to the HDO while the other two are the ring (rH) and the acetate-methylene (acH) protons. At room temperature, the signal for rH protons is about 25 Hz while for the acH protons is about 10 Hz broad, and no fine structure of the spectrum from scalar coupling could be observed. The water peak shows 2 Hz line width. Titrating with KOD, all peaks show a maximum in line width at about pH = 4.2; then the line widths become constant from pH 6 to 9.5: it is 8 Hz for rH, 5 Hz for acH and less than 2 Hz for the HOD (Figure 15).

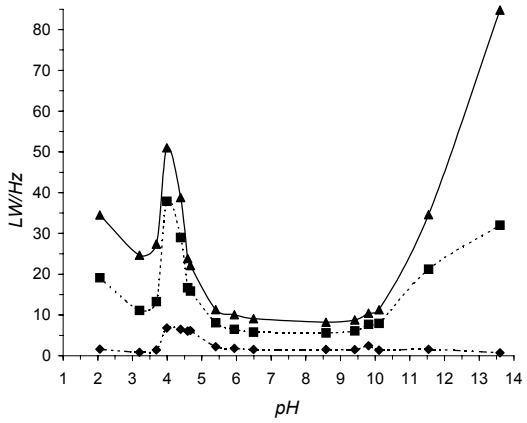


**Figure 15.** Linewidths of species present in $[K(H_XDOTA)]^{(3-x)-}$ - water system versus pH at 298 K. (▲) ring protons (*r*), (■) acetate-$CH_2$ protons and (◆) HOD protons

At pH higher than 9.5, the lines belonging to DOTA broaden dramatically, while the water signal remains constant narrow. When we repeated the experiment with TMAOD, no such phenomena were observed; but the same effect appeared when KCl was added to the DOTA/TMAOD solutions. Therefore, we assumed that the formation of $[K(H_xDOTA)]^{(3-x)-}$ species is responsible for this behaviour. The observed line broadenings of r(H) and ac(H) protons originate from the internal motion of the molecule or from ligand exchange process. On the other hand, the line broadening of HDO signal must be a consequence of intermolecular proton exchange between the HDO and $[K(H_xDOTA)]^{(3-x)-}$ present in the solution at pH~4.

### *3.3.2.1 Intramolecular motion at high pH*

In order to have a deeper insight into the nature of the dynamic processes of $[K(H_xDOTA)]^{(3-x)-}$ species present in alkaline media (where x is probably 0), temperature dependence of the spectrum was recorded at pH~13. Since at the freezing temperature of the solution no clear peak separation was achieved, 30% deutero-acetone was added to the solution for further cooling. At 260 K, the peaks became well resolved and even the following scalar couplings could also be determined (Table 5).

**Table 5.** $^1$H NMR spectrum of K(DOTA)- at 260 K

| $^1$H signal label | δ ppm | $^2J_{HH}$, $^3J_{HH}$ Hz |
|---|---|---|
| $r_1H(a)$ | 5.39 | $^2J_{HH}\{r_1H(a)\text{-}r_1H(b)\} = -11.6$ |
| $r_1H(b)$ | 4.51 | $^2J_{HH}\{r_1H(a)\text{-}r_1H(b)\} = -11.6$<br>$J_{HH}\{r_1H(b)\text{-}r_2H(b)\} = 2.0$ |
| $r_2H(a)$ | 5.69 | $^2J_{HH}\{r_2H(a)\text{-}r_2H(b)\} = -9.9$<br>$^3J_{HH}\{r_1H(b)\text{-}r_2H(b)\} = 13.2$ |
| $r_2H(b)$ | 4.39 | $^2J_{HH}\{r_2H(a)\text{-}r_2H(b)\} = -9.9$<br>$J_{HH}\{r_1H(b)\text{-}r_2H(b)\} = 2.0$ |
| acH(a) | 6.03 | $^2J_{HH}\{acH(a)\text{- }acH(b)\} = -13$ |
| acH(b) | 5.18 | $^2J_{HH}\{acH(a)\text{- }acH(b)\} = -13$ |

The assignment was made on the basis of 2D COSY experiment (Figure 16). In contrast of most previously investigated DOTA complexes, only one set of signals was detected. The ionic radius of $K^+$ is 1.51 Å,[41] even larger

compared to $Bi^{3+}$ and $La^{3+}$. In the case of $Bi(DOTA)^-$ and at the beginning of the lanthanide series, for example for $La(DOTA)^-$, also only one dominant enantiomer pair, the $\Delta(\lambda\lambda\lambda\lambda)/\Lambda(\delta\delta\delta\delta)$ pair was detected.

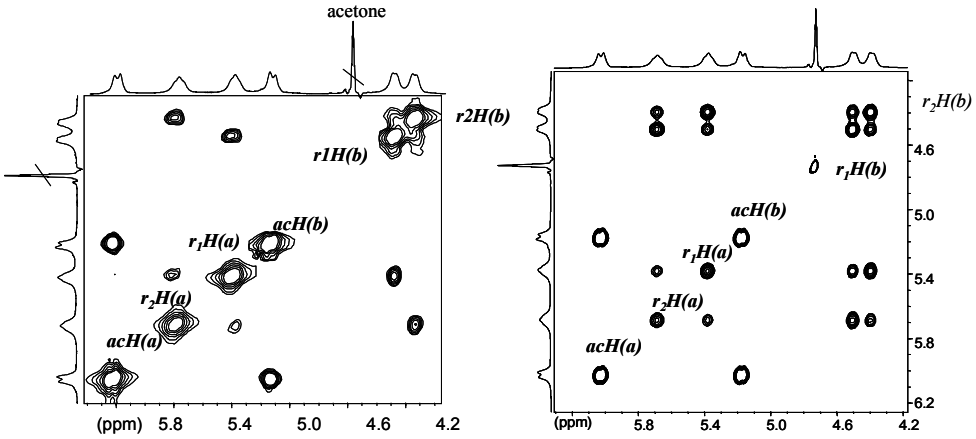


**Figure 16.** $^1$H-$^1$H COSY (left) and. $^1$H-$^1$H EXSY (right) spectra of $K(DOTA)^{4-}$ at 260K

By means of 2D EXSY (Figure 16), intramolecular exchange could be detected, on the one hand between the acH protons, and on the other hand between all rH protons. It is known that the ring inversion results in that the ring carbons switch their positions. It was apparently revealed that in the meantime the vicinal ring protons also take part in a changeover, following the $r_1H(a) \leftrightarrow r_2H(b)$ and $r_1H(b) \leftrightarrow r_2H(a)$ scheme (Figure 17). The rate of the $r_1C \leftrightarrow r_2C$ changeover and the rate of the $r_1H(a) \leftrightarrow r_2H(b)$ and $r_1H(b) \leftrightarrow r_2H(a)$ exchange are of necessity the same. Furthermore, besides this known ring inversion, a new type of intermolecular proton-exchange was detected,

resulting in an exchange process between the geminal ring protons: $r_1H(a) \leftrightarrow r_1H(b)$ and $r_2H(a) \leftrightarrow r_2H(b)$. This geminal ring-proton exchange process requires metal-ligand bond breaking and leads to what we call the ring-slewing motion (Figure 17).

This fluxionality, therefore, could not be detected in the case of inert lanthanide-DOTA complexes. Another verification for the existence of this new process is that by elevating the temperature the ring protons fuse into a singlet peak, while in the case of inert DOTA complexes, they fuse into an AB doublet. According to our finding, carbon exchange does not take place during the ring slewing, only the geminal protons switch their positions. This observation serves as an excellent tool to separate the two different types of ring motions.

Between the acH(a) and acH(b) protons we also detected exchange, which is in connection with the change in the acetate arms' helicity. Since we could detect only one enantiomer pair, these three types of motions must occur between the two enantiomers. The question arises whether the acH(a)↔acH(b) exchange, which is the $\Delta \leftrightarrow \Lambda$ motion, and the two types of motions of the ring (ring inversion and ring slewing) occur in a parallel way, independently of each other, or it is a two-step consecutive reaction where one of the reactions is very fast, leading to steady-state level (not observable by NMR) of the other enantiomer pair.

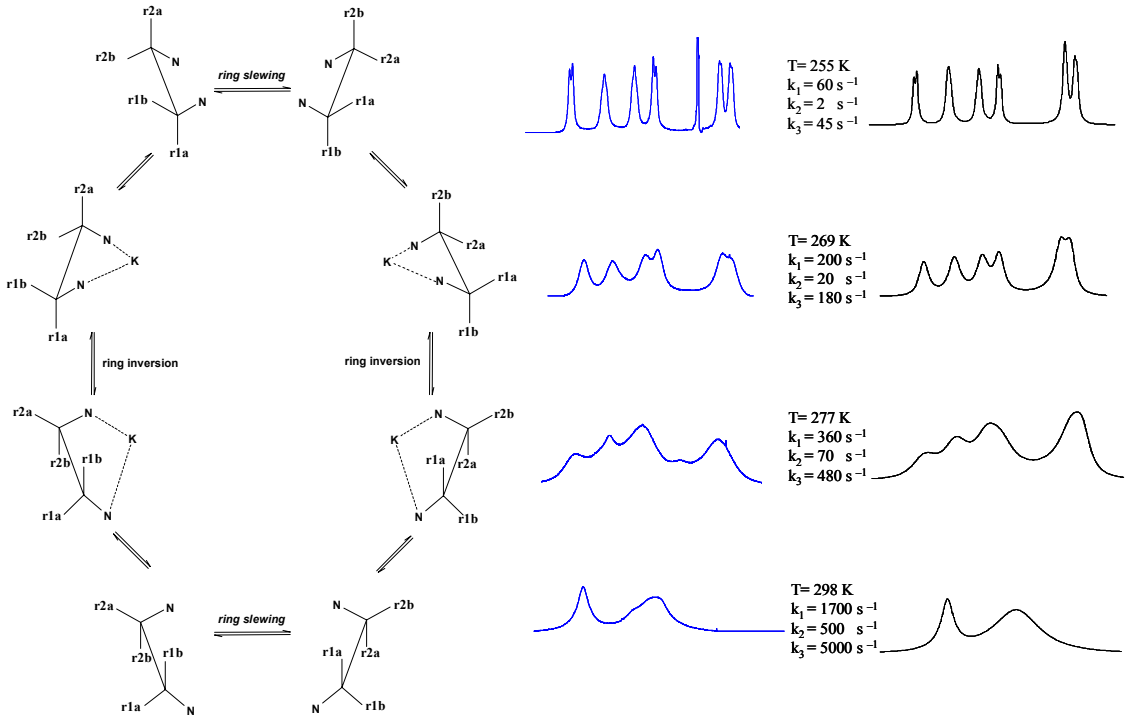


**Figure 17.** Left: $K(DOTA)^{3-}$ ring motions in the case of labile metal-ligand bond: besides the ring inversion well-known from inert lanthanide-DOTA complexes, there is another way of intramolecular rearrangement (”ring slewing”), which requires the rupture of the metal-ligand bond

Right: Measured (blue) and calculated (black) $^1H$ NMR spectra of $K(DOTA)^{4-}$ at several temperatures. The rate costants belong to the ring inversion ($k_1$), the ring slewing ($k_2$ ) and the change in the acetate arms’ helicity ($k_3$)

In order to obtain the rate constants at various temperatures for all process mentioned above, we have made complete band shape analysis by model calculations, based on the Bloch-McConnell equation. The $k_1$ values for the $r_1C \leftrightarrow r_2C$ exchange (the ring inversion) at different temperatures were obtained from modelling the $^{13}C$ spectra. We used these $k_1$ values as fixed parameters for the $r_1H(a) \leftrightarrow r_2H(b)$; $r_1H(b) \leftrightarrow r_2H(a)$ proton exchange. The $k_2$ values, characterizing the $r_1H(a) \leftrightarrow r_1H(b)$; $r_2H(a) \leftrightarrow r_2H(b)$ exchange (the ring slewing), were step-by-step varied until the calculated and the measured $^1H$ spectra fitted (Figure 17). The $k_3$ values for the exchange between the acetate-methylene protons were calculated by modelling the collapse of their AB doublet pair in conformity with the measured temperature-dependent $^1H$-NMR spectra. The Eyring plots for the exchange processes are shown in Figure 18.

The enthalpy of activation for the ring inversion ($\lambda\lambda\lambda\lambda \leftrightarrow \delta\delta\delta\delta$) of $[K(DOTA)]^{3-}$ is smaller than that of $[La(DOTA)]^-$, but larger than that of $[Bi(DOTA)]^-$. The energetic barrier looks independent of the lability of the complexes. The small entropy of activation, $\Delta S^{\#} = -26 \pm 24$ J mol$^{-1}$ K$^{-1}$ for $[K(DOTA)]^{3-}$, shows that there is probably no increase in the number of species during the ring inversion. We can conclude that for this sort of fluxionality, ligand exchange process is probably not required. The ring slewing has larger activation enthalpy than the ring inversion, probably because of the rupture of $K^+$–$(DOTA)^{4-}$ bonds. The large positive entropy of activation shows that this motion is accompanied by the dissociation of the coordinated metal ion.

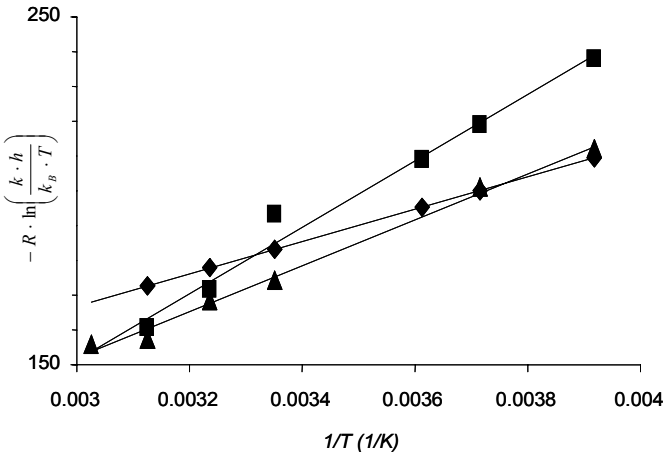


**Figure 18.** Eyring-plots for determining the activation parameters of intramolecular motions of $[K(DOTA)]^{3-}$ complex. (◆) for the ring inversion, (■) for the ring slewing and (▲) for change in acetate arms's helicity

The big difference in the enthalpy of activation between the two ring fluxionalities causes that at lower temperatures the ring inversion is the main ring motion, while the simultaneously existing ring slewing occurs much slower. The change in the acetate arms' helicity accompanies the ring inversion. However, as the temperature increases the $K^+$ ion can dissociate more easily from the DOTA, giving rise to the new type of ring motion, the ring slewing. Interestingly, at high temperature the acH(a)↔ac(H)b (Δ↔Λ) exchange process follows the ring slewing; while the ring inversion has slower rate, compared to the other two motions. We may state that the change in helicity of acetate arms is not an independent form in the fluxionality of $KDOTA^{3-}$ complex. For $La(DOTA)^-$, Jacques *et al.* came to the same conclusion by analysing activation parameters. For $K(DOTA)^{3-}$, the

fluxionality at low temperatures corresponds to that of $La(DOTA)^-$, *i.e.* probably first a slow ring inversion occurs, followed by a fast change in the acetate arms' helicity, resulting in the $\Lambda(\delta\delta\delta\delta) \rightleftharpoons \Delta(\lambda\lambda\lambda\lambda)$ enantiomeric rearrangement. At higher temperatures, the ring slewing becomes faster than the ring inversion, and then this is followed by the fast acH(a) $\rightleftharpoons$ acH(b) exchange. It means that the ring slewing motion is the dominant ring motion, driving the $\Lambda(\delta\delta\delta\delta) \rightleftharpoons \Delta(\lambda\lambda\lambda\lambda)$ enantiomeric rearrangement.

*3.3.2.2 Proton exchange between the water and the DOTA at pH 3.5-5*

Between pH 3.5 and 5 and at room temperature, HDO and both of the $[K(H_xDOTA)]^{(3-x)-}$ $CH_2$ proton signals show significant line broadening (Figure 13). This phenomenon is most likely a consequence of the proton exchange between the bulk water and labile protons of $[K(H_xDOTA)]^{(3-x)-}$ (causes line broadening, observed on HDO signal), accompanied by fluxional motion of the $[K(H_xDOTA)]^{(3-x)-}$ skeleton (causes line broadening, observed on $[K(H_xDOTA)]^{(3-x)-}$ $CH_2$ proton signals). Increasing the temperature, all $CH_2$ signals narrowed; while the water signal showed a maximum in line width, indicating that this latter exchange process is at room temperature on the borderline of slow and fast exchange. By determining the population of protons coordinated to DOTA, we found that the population is less than one percent, compared to the HDO protons in the investigated pH range. Therefore, the Anet equation for strongly biased systems can be used to determine the rate constant, $1/\tau_A$.

$$LB = \frac{4\pi\, p_A\, \tau_A\, \delta^2\, SF^2}{1 + 4\pi^2\, \tau_A{}^2\, \delta^2\, SF^2} \qquad \text{Eq. 3.1}$$

In Eq. 3.1, *LB* is the line broadening, measured at the more populated site, $p_A$ is the population of the less populated site ($[K(H_xDOTA)]^{(3-x)-}$), *SF* is the spectrometer frequency, $\tau_A$ is the lifetime of the proton on the less populated site ($1/k_{AB}$), and $\delta$ is the chemical shift difference between the two exchanging sites. It is easy to show that the line width of the dominant site has a maximum with decreasing $\tau_A$, which is with increasing the temperature. From Eq. 3.1, it follows that the maximum value of line broadening is

$$LB_{max} = p_A\, \delta\, SF \qquad \text{Eq. 3.2}$$

from which $\delta$ could be determined because $p_A$ can be calculated from the protonation constants of DOTA. Since we do not know the exact composition of the exchange partner of HDO, we simply used the average number of protons on DOTA; in other words we handled the DOTA species present in this solution as one kinetic unit. Having determined all unknowns in Eq. 3.1, the $k_{BA} = p_A/\tau_A$ rate constants were determined at different temperatures. We obtained the following kinetic parameters: $\Delta H^{\#} = 54.2 \pm 2$ kJ mol$^{-1}$ and $\Delta S^{\#} = -33 \pm 7$ J mol$^{-1}$ K$^{-1}$ at pH = 3.87 with $\delta$ = 3.35 ppm, while $\Delta H^{\#} = 52 \pm 6$ kJ mol$^{-1}$ and $\Delta S^{\#} = -43 \pm 18$ J mol$^{-1}$ K$^{-1}$ at pH = 4.31$\delta$ = 5.55 ppm. The large change in $\delta$ with increasing pH is not surprising because at pH= 3.87 the dominant species are $K(H_4DOTA)^+$, $K(H_3DOTA)$ and $K(H_2DOTA)^-$ with

almost the same contribution, while at pH= 4.31 $K(H_3DOTA)$ is the dominant. It is difficult to identify what kind of DOTA complex can exchange protons slowly at pH around 4 with water, however, keeping in mind the exceptional stability of diprotonated $[H_2DOTA]^{2-}$, we suppose that an ion pair between this anion and $K^+$ can be responsible for this phenomenon. This $K(H_2DOTA)^-$ can be protonated, forming $K(H_3DOTA)$ assembly, which contains exchangeable protons with HDO. The potassium probably has an "out-of-cage" position, but it can also slow down the intramolecular motion of the macrocycle, leading to line broadening in both of the ring and acetate-methylene proton signals of DOTA (Figure 13). In order to determine what the state of the dynamics is at pH between 6 and 9.5, where $H_2DOTA^{2-}$ and $HDOTA^{3-}$ (both partially containing $K^+$) species are present, we examined the line width of all peaks in a sample of pH 5.94 at 300, 310 and 320 K. The width of water signal was 2.2, 3.2 and 4.3 Hz, respectively. It means that the detected proton exchange with HOD turns to *slow exchange regime*. The line widths of ac and r protons were found to be 6 (300 K), 4.5 (310 K), 3 (320 K) and 9 (300 K), 5 (310 K), 3 (320 K) Hz, respectively. It means that the fluxionality is *in the fast exchange regime* when the pH is between 6 and 9.5, then starts to slow down when the pH is above 10. Already Desreux *et al.* assumed that $[H_2DOTA]^{2+}$ (in 1 M NaCl ionic medium) is a very interesting species. The protonated nitrogens probably make strong H-bonds with the carboxylate groups of the acetate arms on the same nitrogen. In the same time, the basicity of the other two nitrogens decreases dramatically, and becomes even lower than that of the carboxylates not involved in H-bonds. In the presence of $K^+$-ions, we could

show that this species is inert for proton exchange; however, it has a relatively fast fluxionality. The existence and dynamic behaviour of this species support the slow intermolecular proton exchange hypothesis in the formation kinetics of lanthanide complexes. The inertness in proton exchange can be a consequence of the H-bond because at higher pH, when monoprotonated ligand is present (at pH = 9.5, approximately 50% is in the form of $K(HDOTA)^{2-}$, practically no change in the proton exchange rate is observed, since the remaining proton is still in H-bond. Similar observation was published in the case of tricyclic tetramine ligands (so-called "adamanzanes"), where the H-D exchange was found to be extremely slow.

The two minima in the line width of the non-dissociable protons can be interpreted as follows. At pH~2, $H_6DOTA^{2+}$ and $H_5DOTA^{+}$ species are present. The fluxionality is slow in these species, however, its rate may increase by further deprotonation (line narrowing). This acceleration is stopped by the formation of $K(H_xDOTA)^{(3-x)-}$ species (line broadening), then the fluxional motion speeds up again, when $K(H_2DOTA)^{-}$ and $K(HDOTA)^{2-}$ are forming. The rate of the fluxionality does not change until the potassium starts to coordinate to the nitrogens. Consequently, the line widths remain constant until pH about 9.5, where, according to our suggestion, the formation of $K(DOTA)^{3-}$ starts. We assume that this species contains an "in-cage" coordinated $K^{+}$, similarly to the DOTA complexes of lanthanides and other metal ions. It seems to be reasonable to state that the protonation and fluxional phenomena described here play an important role in the early stage of mechanism set up for the formation of inert DOTA complexes.

# 4 Structural and dynamic aspects of C5-substitution on DTPA. Studies on the Lu(*S*-EOB-DTPA)$^{2-}$ complex

## *4.1 Introduction*

Gd(*S*-EOB-DTPA)$^{2-}$ was designed as a hepatobiliary MRI contrast agent (Eovist: (4*S*)-4-(4-ethoxybenzyl)-3,6,9-tris(carboxylatomethyl)-3,6,9-triaza-undecanedioic acid, gadolinium complex, disodium salt).[75,76] This complex is specifically taken up by the hepatocytes via a not fully described mechanism, but not by the tumour cells, resulting in contrast in the MRI image.[77] Novel studies showed its moderate non-covalent binding to human serum albumin, HSA, therefore a possibility to provide a good relaxivity enhancement also in blood vessels.[78]

The introduction of the ethoxybenzyl-group into the 5-position has several physicochemical, structural and stereochemical consequences, compared with the DTPA and its complexes. Gd(EOB-DTPA)$^{2-}$ shows increased relaxivity, compared to Gd(DTPA)$^{2-}$, and it was explained by the expected longer rotational correlation time accounted to the molecular weight increase and by the significantly shorter distance between the hydrogen atoms of the coordinated water molecule and the paramagnetic ion.[75] The water exchange rate also slightly increased, compared with the parent compound. In a recent article, it has been shown that in a new type, bifunctional contrast agent, Gd(*S*-EOB-DTPA-BMA), the presence of the EOB-group fastens the water exchange, compared to Gd(DTPA-BMA).[79]

In the ligand, the carbon in the 5-position becomes asymmetric, resulting in two enantiomers, *S*-EOB-DTPA and *R*-EOB-DTPA. In aqueous solution, as expected, Gd(*S*-EOB-DTPA)$^{2-}$ and Gd(*R*-EOB-DTPA)$^{2-}$ have the same relaxivity. However, Gd(*S*-EOB-DTPA)$^{2-}$ showed more pronounced interaction with human serum albumin than Gd(*R*-EOB-DTPA)$^{2-}$, and competition between Gd(*S*-EOB-DTPA)$^{2-}$ and Gd(*R*-EOB-DTPA)$^{2-}$ for the same binding site was detected.[78]

The coordination of the $Ln^{3+}$ to the EOB-DTPA induces another chiral center appearing on the central nitrogen, *N2*. As a consequence, two diastereomers appear in solution (*C5SN2S*, *C5RN2R* and *C5SN2R*, *C5RN2S*) (Figure 19, 20). Diastereomers can be separated on a reverse phase HPLC column. In the case of Gd(*S*-EOB-DTPA)$^{2-}$, the isomerisation kinetics of the separated diastereomers (*C5SN2S* and *C5SN2R*) was followed by HPLC, which allowed an estimate of 75.3 kJmol$^{-1}$ for the activation energy. NMR investigations on diamagnetic La(*S*-EOB-DTPA)$^{2-}$ assigned the major component (60%) as the *C5SN2R* and the minor isomer as the *C5SN2S* diastereomer. The two separated diastereomers, therefore, differs in the configuration of the *N2* central nitrogen.[76]

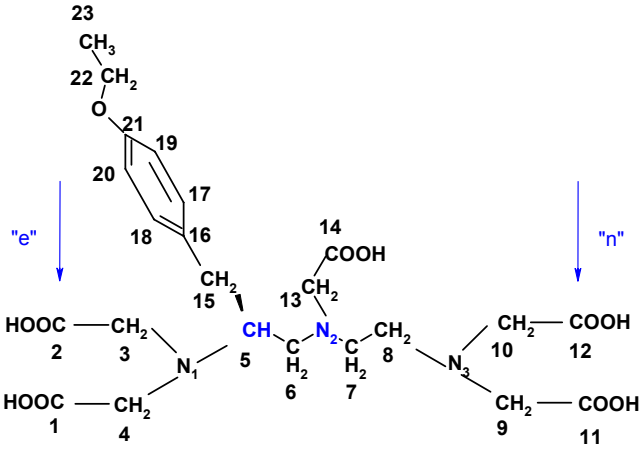


**Figure 19.** Stereochemical consequences of introducing an ethoxy-benzyl group into the 5-position in the case of Ln(EOB-DTPA)2- complexes

However, both isolated components can be mixtures of diastereomers that differ in the position of the acetate arms. Among the five coordinated acetate oxygen atoms, four are in one plain, while the fifth one is on the opposite side of this plain, compared to the coordinated water molecule. This fifth acetate arm can be on the side closer to the EOB-group (labelled by *e*) or on the other, "non-EOB" side (labelled by *n*). In the case of La(*S*-EOB-DTPA)$^{2-}$, the interconversion (wagging process) between these isomers was detected to be fast on the NMR time scale (Figure 19, 20).

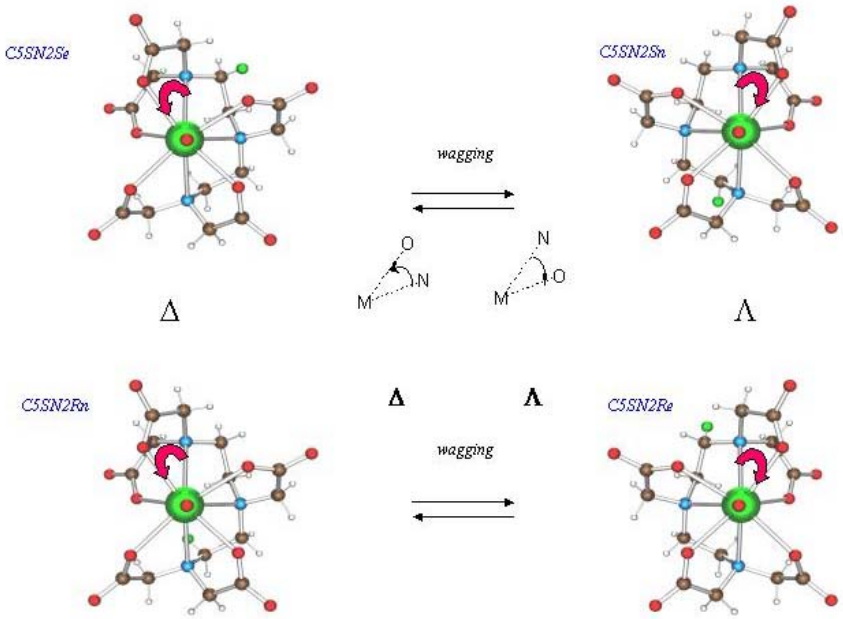


**Figure 20.** The four possible diastereomers in Ln(EOB-DTPA)$^{2-}$ complexes and the wagging processes interconverting the pairs differing in the acetate arms' helicity (the small green ball represents the EOB-group)

These four possible diastereomers all differ in chemical and physical properties. Recently, in the case of EPTPA (ethylenepropylene-triamine-pentaacetate) separate water-exchange rates were determined for individual diastereomers differing in the configuration of the central nitrogen.[80]

In the case of Ln-DOTA-like complexes, it was already observed that the exchange rate between the coordinated water and the bulk may be affected by the isomer conformation.[81]

Our aim was to gain information about that in Ln(*S*-EOB-DTPA)$^{2-}$ systems (Ln=Lu), to learn which isomers can be assigned, what the ratios and the structural differences are between them, and what kind of interconversion processes can be detected between them.

## *4.2 Experimental*

The ligand was kindly provided by Schering AG, Germany. The $LuCl_3$ stock solution was prepared by dissolving 99.9% $Lu_2O_3$ (Fluka) in HCl, followed by evaporating the HCl excess. The concentration of the $LuCl_3$ solution was determined by complexometric titration with standardised $Na_2(H_2EDTA)$ solution, using xylenolorange indicator.

The 0.2 M solution of the Lu(*S*-EOB-DTPA)$^{2-}$ complex was made by dissolving appropriate amount of the ligand in distilled water, followed by dropwise adding of stoicheiometric amount of $LuCl_3$. The pH was adjusted between 6-6.5 at the end by adding NaOH. The $H_2O$ was evaporated and the remaining solid complex was dissolved in 600 μl $D_2O$. This evaporation-dissolution procedure was repeated in two more times.

The NMR measurements were made on Bruker AM 360 or Bruker DMX 500 spectrometers in deuterium-locked mode. The chemical shifts were referenced to TMS*. The temperature was regulated by Eurotherm equipment, fitted to the spectrometer. The temperature was corrected by using methanol chemical shifts according to literature.[72] The $^{13}C$ NMR spectra were recorded in J-modulated decoupling or inverse gated decoupling mode, depending on the need for getting quantitative spectrum. Typical pulse width corresponded to 30$^o$ flip angle and 10-15 s relaxation delays were used

in order to use the signal integrals determination of quantitative concentration of $^{1}H$ spectra.

The $^{1}H$-$^{1}H$ COSY spectra were made with the standard Bruker program, using 45º mixing pulse. The $^{1}H$-$^{13}C$ correlation spectra were recorded on Bruker DMX 500 spectrometer in inverse mode, using gradient pulses in the *z* direction with the usual Bruker HSQC or Bruker HMQC pulse sequence. Data processing was made by Bruker WinNMR software package. The line widths were determined by deconvolution, fitting Lorentz curves on the peaks.

## *4.3 Results and Discussion*

At 300 K temperature, two sets of signals appear both in $^{13}C$ and $^{1}H$-NMR. The signals are broad, however, the integration of the $^{1}H$ NMR signals shows that the ratio between the two sets of signals is 35:65. These isomers differ in the configuration of the central nitrogen, similarly to the observation of Schmitt-Willich *et al.*[76] Elevating the temperature, the signals of the two sets showed separate narrowing, showing that the change in the configuration of the central nitrogen is too slow to detect on this NMR time scale (Figure 21).

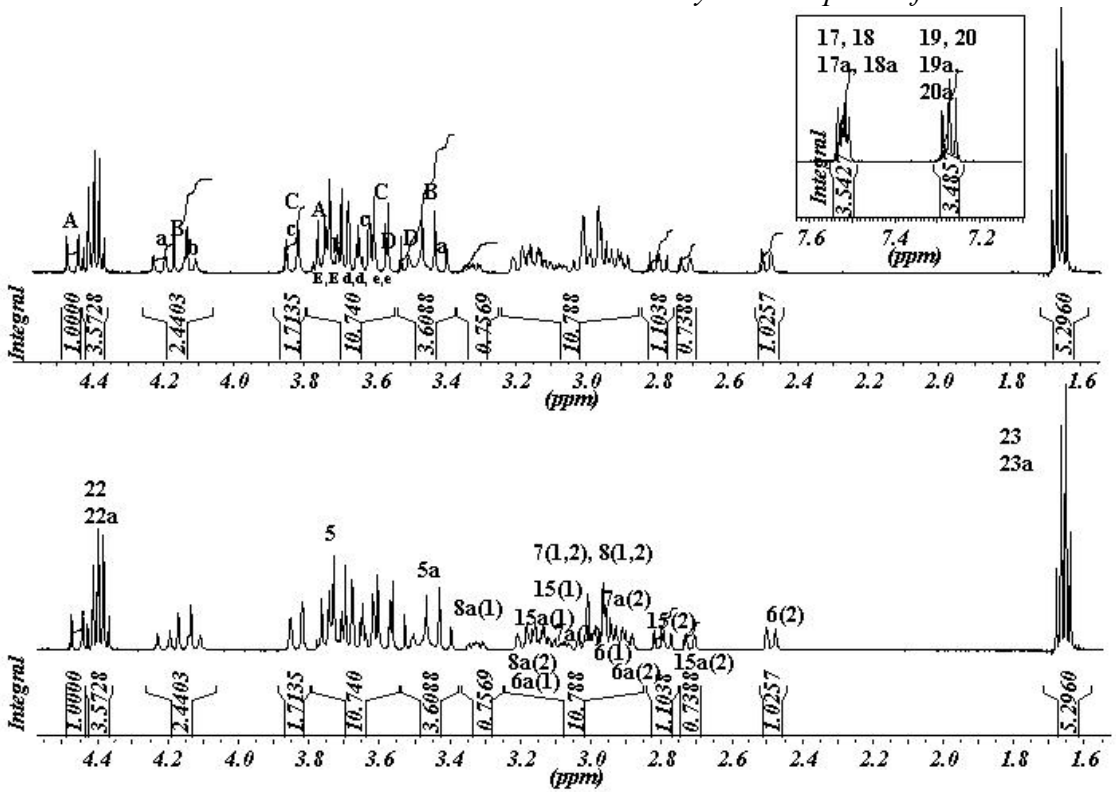


**Figure 21.** $^{1}$H NMR spectrum of Lu(EOB-DTPA)$^{2-}$ at 330K. Index a labels signals for the minor isomer. A,B,C,D,E label the acetate $CH_2$ protons for the major, a,b,c,d,e for the minor isomers

At 330 K, the assignment of the signals was possible by 2D $^{1}$H-$^{1}$H COSY (Figure 22), $^{1}$H-$^{13}$C HMQC and $^{1}$H-$^{13}$C HMBC techniques. Especially the $^{1}$H-$^{13}$C HMBC proved to be very useful to assign the $CH_2$ protons neighbouring the $COO^-$ groups. In the $^{1}$H spectra (Figure 21), these protons can be found separately in the chemical shift range 3.35-4.50 ppm, except that in this range the *22* ("major isomer") and *22a* ("minor isomer") ethoxy $CH_2$ proton (4.35-4.45 ppm) and the *5* (3.7-3.8 ppm) and *5a* (3.4-3.5 ppm) asymmetric CH proton signals also appear.

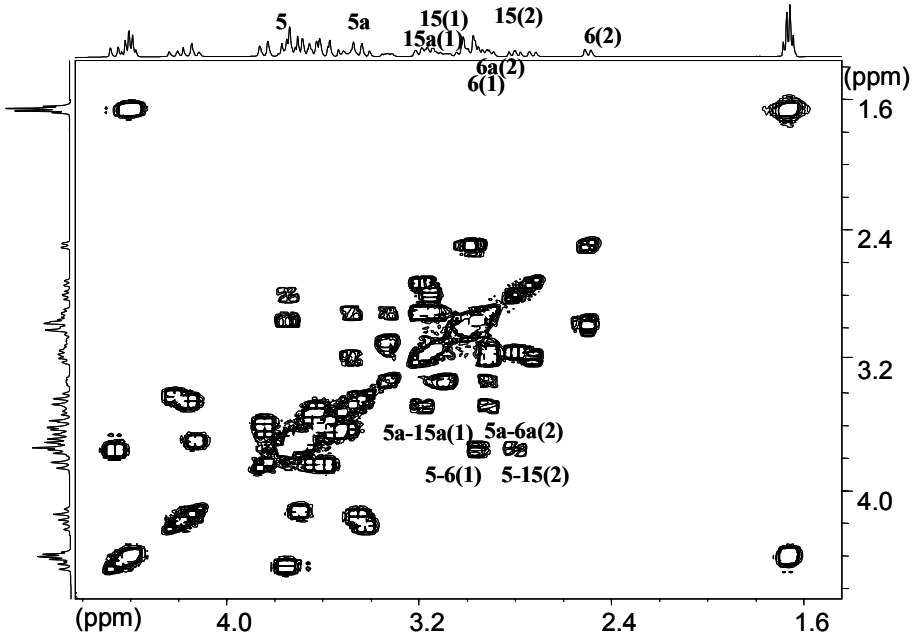


**Figure 22.** $^{1}$H-$^{1}$H COSY spectra of $Lu(EOB\text{-}DTPA)^{2-}$ at 330K. Index *a* labels signals for the minor isomer

By the $^{1}H$-$^{1}H$ COSY, we could assign which protons are geminal among the $COO^{-}$-neighbouring $CH_2$-s. They are labelled with the same letter (small for the minor, capital for the major isomer). The further assignation showed at 1.6-1.7 ppm the *23* and *23a*, between 2.45 and 3.35 ppm the diethylene-triamine backbone protons (except *5* and *5a*), and the aromatic protons of the ethoxy-benzyl group at 7.25-7.30 ppm *(19, 19a, 20, 20a)* and at 7.50-7.55 ppm *(17, 17a, 18, 18a)*. At 330 K, despite the partly overlapping signals, several coupling constants could be determined. For the minor isomer, the *7a(1), 7a(2), 8a(1), 8a(2)* protons could be (partly) separated, and their couplings could be determined by modelling the spin system (Figure 23). The obtained coupling constants are the following: $J_{7a(1)\text{-}7a(2)}$ = 12 Hz, $J_{7a(1)\text{-}8a(1)}$ = 8 Hz, $J_{7a(1)\text{-}8a(2)}$ = 2 Hz, $J_{8a(1)\text{-}8a(2)}$ = 12 Hz, $J_{8a(1)\text{-}7a(2)}$ = 2 Hz, $J_{8a(2)\text{-}7a(2)}$ = 2 Hz. It indicates the staggered conformation of the ethylene-diamine backbone, already shown for $Ln(DTPA)^{2-}$ complexes.

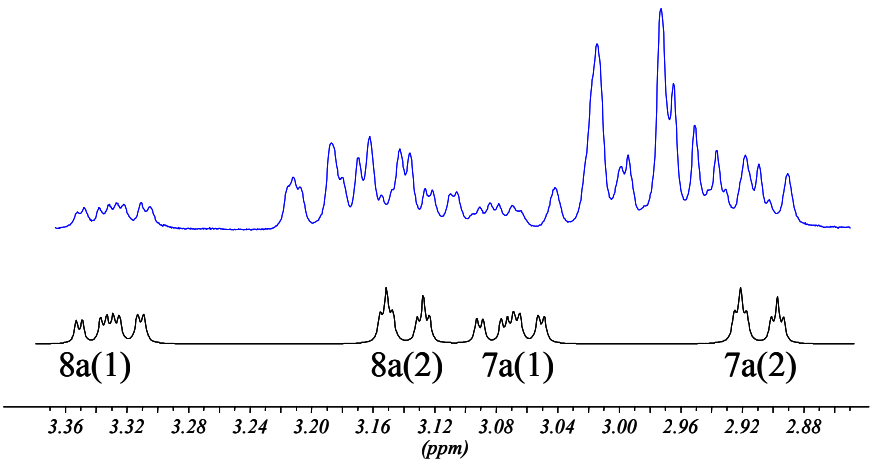


**Figure 23.** Modeling the coupling scheme for the 7a-8a ethylenediamine backbone of the minor isomer of $Lu(EOB\text{-}DTPA)^{2-}$

Other characteristic couplings could be (partly) determined: the *15(2)* and *15a(2)* protons couple with their geminal pairs (*15(1)* and *15a(1)*) and with the vicinal 5 and 5a protons. The geminal coupling constants have almost the same value, $J_{15(1)\text{-}15(2)}$ = 13.7 Hz, $J_{15a(1)\text{-}15a(2)}$ = 13.5 Hz, while the vicinal coupling constants differs, $J_{15(2)\text{-}5}$ = 10.6 Hz, $J_{15a(2)\text{-}5}$ = 2.2 Hz. Since we could not separate the *15(1)*- and *15a(1)*-proton signals, we can only assume that in both cases among the *15* and *15a* protons one couples with the *5* and *5a* protons with large coupling constant, indicating an axial position (*15(2), 15a(1)*), and the other couples with smaller coupling constant, indicating a gauche position (*15(1), 15a(2)*).

At temperatures lower than 300 K, the lines of the two isomers showed separate broadening. This observation is a consequence of the change in the acetate arms' helicity, "wagging", which is observable on the NMR time scale. However, until freezing it remained in the "fast" exchange region, so we could not determine the population of those diastereomers differing in the acetate arms' positions. In the case of the Ln-DTPA complexes, the wagging process occurs between enantiomers with equal populations. Here, the wagging occurs between diastereomers (Figure 20). In our case, an assumption can be made for the populations of the diastereomers, which are in fast exchange, resulting in the average signals of the minor isomer. The "wagging" process results in a rearrangement shown in Figure 24, concerning the *7a(1), 7a(2), 8a(1), 8a(2)* moiety: while in one position, two vicinal protons are in axial position with large vicinal couplings, the other two have smaller vicinal coupling constant. In the other position, the second two turn into axial position, while the others occupy the equatorial position. In fast

exchange, it results in a population-averaged coupling constant. Model-calculations showed that in our case the pattern, seen in the 330 K $^{1}$H-spectrum, could be obtained only if the ratio of the populations is at least 1:8 or 1:10 (Figure 25).

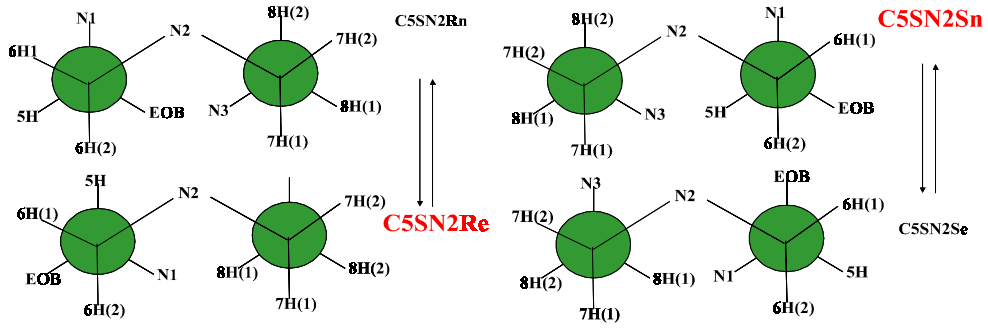


**Figure 24.** Schematic representation of the wagging process through the C5-C6-N2-C7-C8 bonds

To answer the question what the dominant position is for the major and minor isomers, we can get some information by investigating the coupling scheme for the *5* and *5a* protons. Since their signals cannot be resolved, only the 330 K 2D $^{1}$H-$^{1}$H COSY cross-peaks provide qualitative information (Figure 22). The *5a* proton shows intensive cross-peaks with two signals, the *15a(1)* and *6a(2)* protons. Similar observation is possible in the case of the *5* proton, which shows intensive cross-peaks with the *15(2)* and *6(1)* protons. Moreover, in the case of the separated *6(2)* proton signal, only the geminal coupling with the *6(1)* can be resolved, indicating the small, non-detectable vicinal coupling with *5*. This can be explained by the larger population of *C5SN2Sn* and *C5SN2Re* isomers in the equilibrium which takes place by the change in the acetate arms' helicity. In these isomers, the position of the *6*

and *6a* protons results in one large vicinal (axial) and one smaller vicinal (gauche) coupling. In the *C5SN2Se* and *C5SN2SRn* isomers the position of the two *6* and *6a* protons is gauche to the *5* and *5a* protons, and it would be indicated by two-two small vicinal couplings appearing on *5* and *5a* (Figure 24).

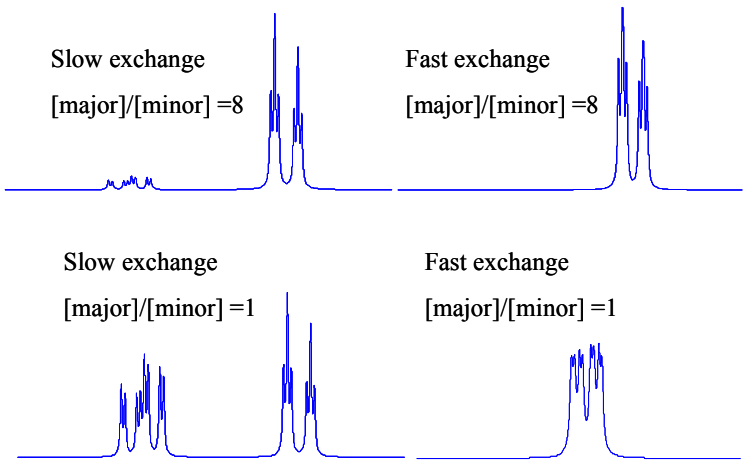


**Figure 25.** Modeling the coupling scheme and the dynamics for the 7a-8a ethylenediamine backbone of the minor isomer of Lu(EOB-DTPA)$^{2-}$

With the obtained information we can state that the two isomers existing in observable population are the *C5SN2Sn* and *C5SN2Re*. However, we cannot distinguish which one gives the major and which one gives the minor set of signals. A recent publication about the chiroptical examination of the diastereomers of Eu(*S*-EOB-DTPA)$^{2-}$ has arrived to the same conclusion: they have found that both isomers have Λ helicity, according to the acetate arms' position.[82] If we applied this notation initially introduced for DOTA complexes, we can see that this Λ helicity appears exactly in the *C5SN2Sn*

and *C5SN2Re* with our abbreviation; while the *C5SN2Sn* and *C5SN2Re* would show Δ helicity (Figure 20).

With decreasing temperature, the proton signals of the minor isomer showed more intensive broadening than the proton signals of the major isomer. Therefore we can say that the thermodynamically less stable isomer shows larger temperature dependence (larger activation energy) in its internal motion, and at 273 K it is slower than the similar internal motion of the major isomer. Since we could not reach the slow exchange region even at freezing temperature and therefore we don't know the exact population of the four diastereomers, these statements remain only qualitative.

# 5 $Gd^{3+}$-loaded zeolites as potential particulate MRI contrast agents

## *5.1 Introduction*

The development of the MRI technique has provoked an increasing interest in specific contrast agents that target certain organs and regions in the human body. Gadolite, which is a $Gd^{3+}$-modified NaY zeolite for the targeted imaging of the gastrointestinal tract, was developed by Balkus *et al*.[28,83] More recently, Reynolds *et al.* have synthesised $Gd^{3+}$-loaded core-shell polymer nanoparticles with a diameter of 120 nm to be of a potential use both in the gastrointestinal part and the intravascular system, being small enough to pass through the vasculature.[37] More examples can be found in the Bibliographic review.

Zeolites are chemically and thermally resistant crystalline aluminosilicates. They have well-defined pore structure and channel system of molecular dimensions; their framework consists of $AlO_4$ and $SiO_4$ tetrahedra, which are linked through oxygen bridges. Through these connections pores with various size can form.

The framework of zeolite Y is based on sodalite cages (which can be seen as truncated octahedron) that are joined by O bridges between the hexagonal faces. Eight sodalite cages are linked, leaving a large central cavity or supercage with a diameter of 12.5 Å. The supercages share a 12-membered ring with an open diameter of 7.4 Å. (Figure 26)

The framework of zeolite A is also made up of sodalite cages but the arrangement of them is different from the framework Y. Here, the eight sodalite cages are connected through the tetragonal faces, leading to cubic arrangement. The supercage formed between the eight sodalite cages, therefore, is smaller, with 9.6 Å diameter, so is the 8-membered ring with an open diameter of 4.1 Å. (Figure 26)

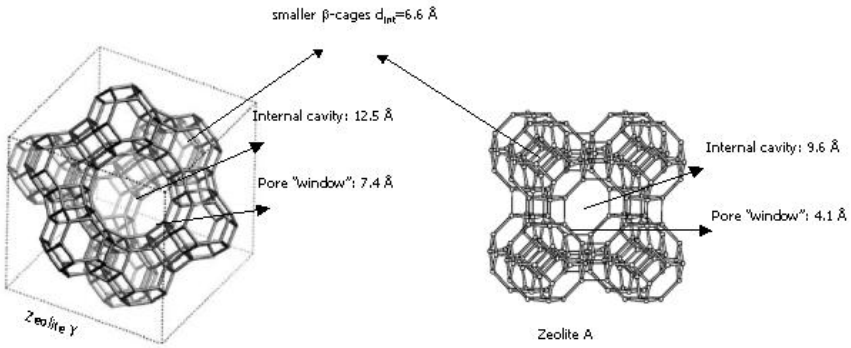


**Figure 26.** Structure of zeolite A and zeolite Y framework

The cations that balance the negative charge of the $AlO_4$ units can be exchanged, which allows incorporation of paramagnetic ions into the structure. Therefore these various aluminosilicate frameworks can serve as "carrier matrices", encapsulating the Gd(III)-ion. This simple model already predicts that the accessibility of the encapsulated Gd(III) ions for water plays

a crucial role in the mechanism of "spreading" the paramagnetic effect to the bulk water.

Recently, Peters *et al.* have presented a detailed study of $Gd^{3+}$-loaded NaY zeolite nanoparticles showing relaxivity substantially higher than the one of Gadolite.[36] The nanoparticles had an average size of 80-100 nm, as determined by TEM and XRD. The structure was determined by means of multinuclear solid state NMR spectroscopy. The NMRD (NMR dispersion) profiles, obtained for aqueous suspensions of samples with various $Gd^{3+}$ loading within the range 1.3-5.4 wt% at various temperatures, showed relaxivities ranging between 11.4 and 37.7 $s^{-1}mM^{-1}$ at 60 MHz and 37 $^{o}C$. The relaxivity increased drastically as the $Gd^{3+}$-loading decreased. The combined EPR and NMRD experimental data were explained by the use of a model considering two-step water exchange: first between the water molecules in the coordination sphere of the immobilised $Gd^{3+}$ and the water in the interior of the zeolite pores; followed by the relatively slow diffusion of the water from the pores into the bulk water (Figure 27).

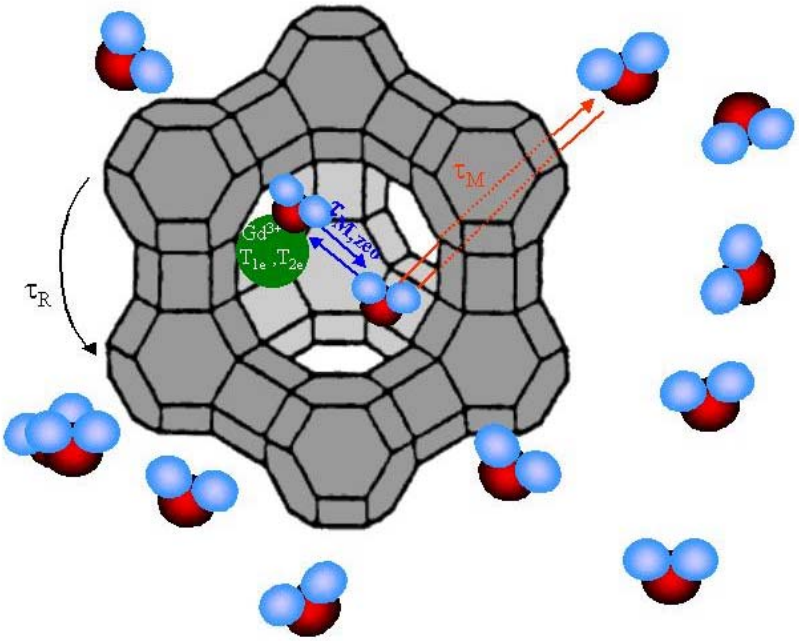


**Figure 27.** Representation of the two-step model suggested by Peters *et al.* to explain the $r_1$ enhancement caused by $Gd^{3+}$-loaded zeolite nanoparticles

The relaxivity measured on the bulk water can be expressed similarly to the Swift-Connick equation used for the "classic" contrast agents, since the population of the bulk water is larger than the population of the water inside the zeolite pores.[9,10,36]

$$r_1 = \frac{1}{c_{Gd^{3+}}}\left(\frac{1}{T_{1,obs}} - \frac{1}{T_{1,dia}}\right) = \frac{x+q}{1000 \cdot 55.5}\left(\frac{1}{T_{1zeo} + \tau_{zeo}}\right) \qquad \text{Eq. 5.1}$$

In Eq. 5.1, $c_{Gd3+}$ is the $Gd^{3+}$ concentration in mM, $T_{1,obs}$ is the measured $T_1$ in presence of the $Gd^{3+}$-exchanged zeolite, $T_{1,dia}$ is the measured $T_1$ in presence

of the zeolite without $Gd^{3+}$, $x$ is the number of free water molecules inside the zeolite per $Gd^{3+}$ ion (water molecules not coordinated to $Gd^{3+}$), $q$ is the number of inner sphere water molecules coordinating to the $Gd^{3+}$ ion, $\tau_{zeo}$ is the residence time of the water protons inside the zeolite, and $T_{1zeo}$ is the longitudinal relaxation time of water protons inside the zeolite.

However, inside the zeolite, the population of the water molecules coordinated to $Gd^{3+}$ and the population of free water molecules inside the zeolite per $Gd^{3+}$ ion (water molecules not coordinated to $Gd^{3+}$) do not differ much, therefore we should use Eq. 5.2 for chemical exchange in a concentrated system to express $T_{1zeo}$.[36,84,85]

$$\frac{1}{T_{1zeo}} = \frac{\frac{q}{x}}{\tau_m + T_{1m}\left(1+\frac{q}{x}\right)} \qquad \text{Eq.5.2}$$

in which $T_{1m}$ is the longitudinal relaxation time of inner sphere water protons, and $\tau_m$ is the mean residence time of water protons in the inner sphere of the $Gd^{3+}$ ions. The longitudinal relaxation rate of the inner sphere water molecules is governed by the dipolar mechanism, according to Eq. 2.6.[11-13]

The results of the simultaneous fitting of the NMRD and EPR measurements showed that the relaxivity is mainly limited by the relatively slow diffusion of water protons from the interior of the zeolite cavities towards the bulk water. The $Gd^{3+}$ ions are immobilised very efficiently in the zeolite cavities, which was indicated in the very long $\tau_R$. $q$ was estimated to have a value of 7; the model is: the $Gd^{3+}$ ions are immobilised by two O-bridges to the zeolite. The decrease of relaxivity observed with increased $Gd^{3+}$-loading is mainly

due to the decrease in the number of water molecules inside the cavities. The water exchange rate located in the zeolite pores is within an order of magnitude of that on $Gd(H_2O)_8^{3+}$ but decreases drastically when the $Gd^{3+}$ loading increases.

Our aim was to study systematically the effect of changing various parameters such as Si/Al ratio within the zeolite framework, pore size and $Gd^{3+}$ distribution on the relaxivity. Therefore NaA zeolite with similar particle size was synthesised, NaY and NaA zeolite samples were dealuminated by using milder and severe methods prior to $Gd^{3+}$-loading. We used calcination to change the distribution of $Gd^{3+}$ ions inside the zeolite and to revise its effect on the relaxation rate enhancement. To gain more information about the mechanism, $r_2$ transverse relaxivities were also measured at higher fields, and equations were worked out for interpreting the results.

## *5.2 Experimental*

### 5.2.1 Materials

The batch of zeolite NaY used in this study was a gift from Akzo Nobel. The chemicals used for zeolite NaA synthesis were aluminium-isopropylate, tetramethyl-ammonium-hydroxide, Ludox HS30 and NaOH (all of them from Aldrich). $GdCl_3 \cdot 6\ H_2O$, $DyCl_3 \cdot 6\ H_2O$ and xanthan gum were also purchased from Aldrich.

The zeolite NaA synthesis was made according to Traa *et al.*[86] 80.4 g tetramethyl-ammonium-hydroxide solution, 4.8 g 1 M NaOH solution, 6.0 g

aluminium-isopropylate and 15.6 g distilled water were stirred in a 250 $cm^3$ Nalgene polypropylene bottle until the aluminium-isopropylate was dissolved. In another polypropylene bottle, 16.0 g $H_2O$ and 18 g Ludox HS30 were mixed together. This mixture was added to the basic aluminium-isopropylate solution, and the polypropylene bottle was capped tightly. The obtained opalic solution was slowly stirred magnetically at 80 $^oC$ in an oil bath for 24 h. After 2 hours, the solution became clear; the final product was white solid dispersed in the mother liquid. The bottle was cooled by ice and water, and the zeolite was separated by centrifugation with 4000 rpm for 60 min at 5 $^oC$. The resulting solid was washed three times with appropriate amount of water under ultrasonication, followed by centrifugation with 4000 rpm for 60 min at room temperature. The NaA zeolite was dried at 80 $^oC$ overnight. Afterwards the NaA zeolite was calcined, using the following temperature ladder: 25 $^oC \rightarrow$ 5 $^oC$/min $\rightarrow$ 150 $^oC$ 1 hour $\rightarrow$ 5 $^oC$/min $\rightarrow$ 550 $^oC$ 3 days $\rightarrow$ -5 $^oC$/min 25 $^oC$. The weight of the resulted NaA sample was around 1 g.

The dealumination of both NaA and NaY was completed in two ways. The mild dealumination was made by using $(NH_4)_2SiF_6$ (Riedel-de-Haën), while in the severe method we used 0.5 M HCl.

For the mild method 1 g was used from each type of zeolites. First, highly ammonium-exchanged zeolite was made by subjecting 1 g of the zeolite to ion exchange with 20 $cm^3$ of 1 M $NH_4NO_3$ solution (Merck) at 60 $^oC$ for 1 hour. After product recovery and washing, the zeolite samples were dried at room temperature to avoid damage to the zeolite structure. For the actual mild dealumination step, the samples of $NH_4$-exchanged zeolites were

dispersed by ultrasonic treatment in 70 $cm^3$ of 1 M $NH_4$-acetate solution (Aldrich) in 125 $cm^3$ polypropylene Nalgene flasks. Using vigorous stirring, 0.25-0.25 g $(NH_4)_2SiF_6$ was added. The flasks were capped and were kept at 60 $^oC$ for 1 hour in an oil bath with further vigorous stirring. The solid samples were separated by centrifugation and washed three times with demineralised water to remove all soluble by-products. For stabilisation, the obtained materials were treated twice with 1 M Na-acetate solution (Aldrich) and washed again with water three times. The solid samples were dried at room temperature.

The severe dealumination of NaA and NaY was made by stirring 0.6 g NaA and 0.5 g NaY with 10-10 $cm^3$ 0.5 M HCl at 80 $^oC$ for 4 hours. The solid was separated by centrifugation and washed three times with demineralised water to remove all soluble by-products. The solid was dried at room temperature.

Before $Gd^{3+}$-exchange, the four dealuminated NaA and NaY samples were stirred with 10 $cm^3$ 1M NaCl overnight. The $Gd^{3+}$-exchange was completed by using 0.3 g NaA dealuminated by HCl, 0.5 g NaA dealuminated by $(NH_4)_2SiF_6$, 0.2 g NaY dealuminated by HCl, and 0.3 g NaY dealuminated by $(NH_4)_2SiF_6$. The solid samples were dispersed under ultrasonication in 2 $cm^3$ demineralised water, except that the 0.5 g NaA dealuminated by $(NH_4)_2SiF_6$ was dispersed in 3.3 $cm^3$ water. The pH of the samples were 4.1, 8.4, 7.3 and 6.8, respectively. The pH was adjusted with 0.1 M HCl or 0.1 M NaOH to pH 5.5. Next, 0.013-0.013 g $GdCl_3 \cdot 6\ H_2O$ was added, except that to the 0.5 g NaA dealuminated by $(NH_4)_2SiF_6$ 0.019 g $GdCl_3 \cdot 6\ H_2O$ was added. The samples were stirred overnight. Afterwards, the $Gd^{3+}$-exchanged zeolites were transferred into dialysis tubes (Sigma-Aldrich, 1 cm diameter), and

dialysis was made for 24 hours against water. The water was removed by rotation evaporation, and the $Gd^{3+}$-exchanged zeolites were dried at room temperature.

The calcination of the original GdNaY with 1.3 weight% Gd used by Peters *et al*.[36] was made as it follows. 0.1 g-0.1 g GdNaY were heated in a calcination oven with continuous, mild air flow for 1 hour at 100, 300, 400 or 500 $^{o}$C, respectively. We used the following temperature programme: 25 $^{o}$C $\rightarrow$ 5 $^{o}$C/min $\rightarrow$ the desired temperature 1 hour $\rightarrow$ -5 $^{o}$C/min 25 $^{o}$C.

The characterisation of the obtained zeolites was made by using x-ray power diffraction (XRD), $^{29}$Si and $^{27}$Al MAS NMR, and ICP.

### 5.2.2 Methods

The XRD patterns were obtained with a D-5000 Siemens diffractometer, with Ni-filtered $Cu_{K\alpha}$ radiation ($\lambda$= 1.5406 Å). MAS NMR spectra were recorded on a Varian VXR-400S spectrometer with resonance frequencies of 79.460 MHz ($^{29}$Si) and 104.229 MHz ($^{27}$Al).

High-resolution transmission electron microscopy (HRTEM) was performed on a Jeol JEM-2010 electron microscope operated at 200 kV.

The NMRD measurements were made on a Stelar equipment, the $T_1$ and $T_2$ measurements on 20 and 60 MHz were made on Bruker Minispec relaxometers, the 300 MHz measurements were made on a Varian Inova-300 spectrometer, using inversion recovery sequence for $T_1$ and CPMG spin-echo sequence for $T_2$ measurements. The 500 MHz measurements were made on a Bruker DMX 500 spectrometer, using inversion recovery sequence for $T_1$ and CPMG spin-echo sequence for $T_2$ measurements.

For the NMRD measurements, 10 mg of the given $Gd^{3+}$-exchanged zeolite was dispersed under ultrasonication in 10 $cm^3$ demineralised water, containing 0.2% xanthan gum as surfactant. The diamagnetic term was measured by using 10 mg of NaY or NaA dispersed in 10 $cm^3$ demineralised water, containing 0.2% xanthan gum as surfactant.

## *5.3 Results and Discussion*

### 5.3.1. Synthesis

During the NaA synthesis we followed the procedure described in the literature.[86] In the synthesis of nanocrystalline zeolites usually tetraalkyl-ammonium salts are used as organic templates, around which the pore formation could start. Therefore the shape and the size of the pores can be tailored, the requested type of framework can be formed. The use of the tetramethyl-ammonium hydroxide as a template in the synthesis led to the formation of high crystalline zeolite A. The relatively high concentration of the used template promoted the nucleation and, thus, the formation of small crystals. The yield, however, is low since crystallisation time longer than one day would have led to undesired larger crystal size.[87] The template was removed by calcination afterwards. The obtained crystals were characterized by XRD, which gave the typical zeolite A pattern and HRTEM, which showed high cubic crystalline particles with average crystal diameter around 130 nm (Figure 28).

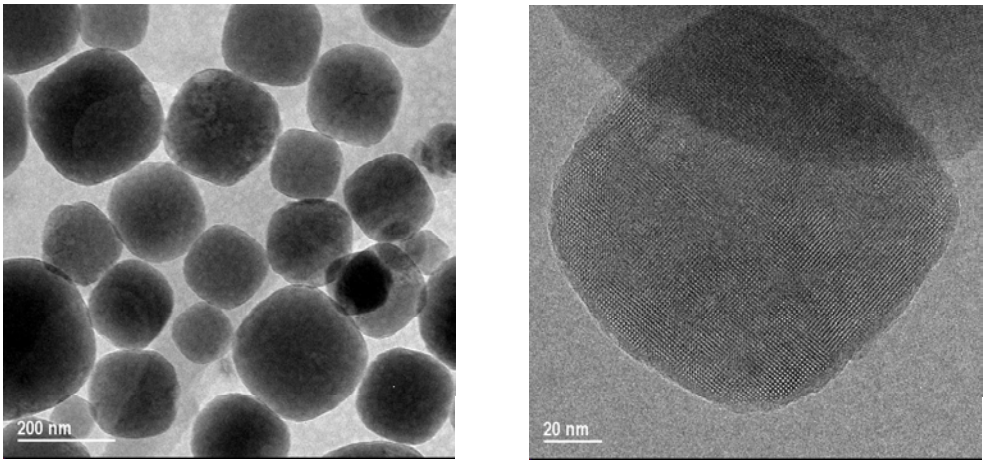


**Figure 28.** HR-TEM pictures of zeolite A with average diameter of 130 nm.

Dealumination of zeolites is an often-applied method to gain zeolites with higher Si/Al molar ratio in the framework, which makes them more hydrophobic. It has high importance in catalysis or gas separation when the nanocrystals are incorporated in hydrophobic polymers, providing increased compatibility between the polymer and the zeolite particles. However, with dealumination we also create vacancies in the zeolite framework by (partly) removing the Al, so loss in crystallinity and appearance of extra pores can also occur. We used two methods for dealumination of the zeolites with Y and A framework. The "mild dealumination" was completed by using $(NH_4)_2SiF_6$. First, the $Na^+$ counter cations were exchanged to $NH_4^+$ ions. After ammonium ion exchange, the zeolite frameworks were not destroyed. This dealumination reaction was resulted in significant increase in the Si/Al ratio, as it was shown by ICP, and loss in crystallinity was demonstrated by

the decreased signal intensities in XRD. It can be seen that using the same conditions, the less stable A framework suffered larger loss in crystallinity (Figure 29).

The “severe dealumination” was completed by using 0.5 M HCl. Here, higher Si/Al ratios were gained compared to the samples obtained from the “mild dealumination” method. The loss in crystallinity was also higher; the XRD signals completely disappeared in the case of the A framework, indicating the collapse of the structure and appearance of amorphous material.

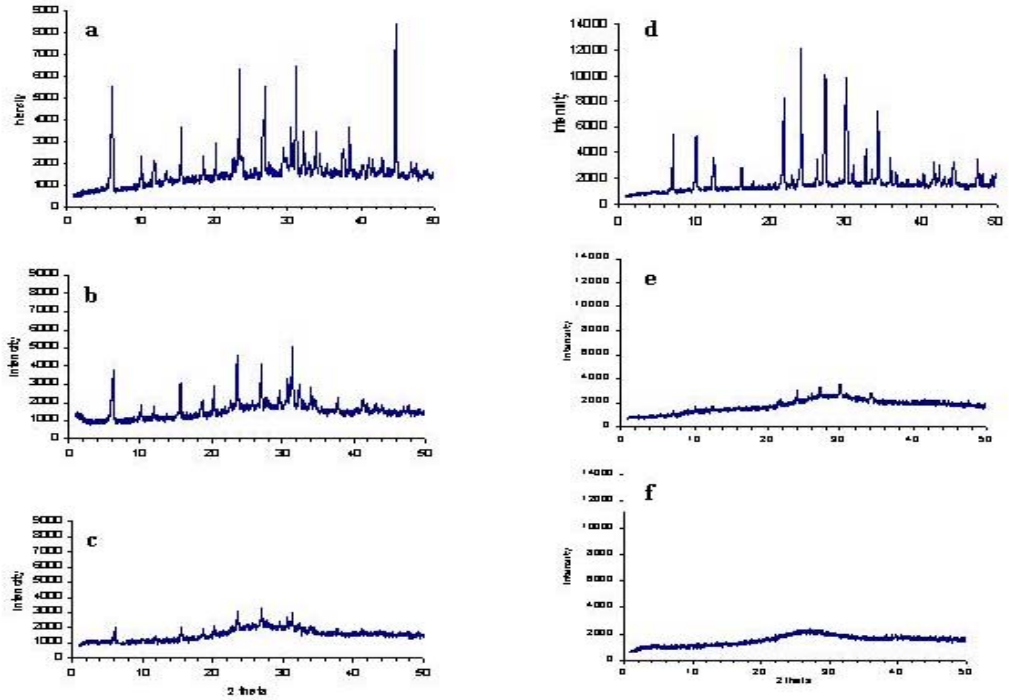


**Figure 29.** XRD patterns for zeolite NaY (left) and zeolite NaA (right), effect of mild (b and e) and strong (c and f) dealumination

### 5.3.2. Relaxivity measurements

The $Gd^{3+}$-exchanged, dealuminated Y zeolites were studied by NMRD. For the NMRD fitting, we used the model first described by Peters *et al.* For initial parameters, we used the parameters obtained for the original, non-dealuminated GdNaY with 2.3 weight% Gd. We tried to prepare the $Gd^{3+}$-exchanged dealuminated Y zeolites with similar $Gd^{3+}$-loading, since it is known that with increased $Gd^{3+}$-loading the relaxivity decreases. We obtained the following two samples: GdNaY/$(NH_4)_2SiF_6$-1.8 and GdNaY/HCl-2.3 where the numbers indicate the $Gd^{3+}$-loading in weight%. The relaxivity is increased upon dealumination and the mild dealuminated sample showed the highest relaxivity (Figure 30).

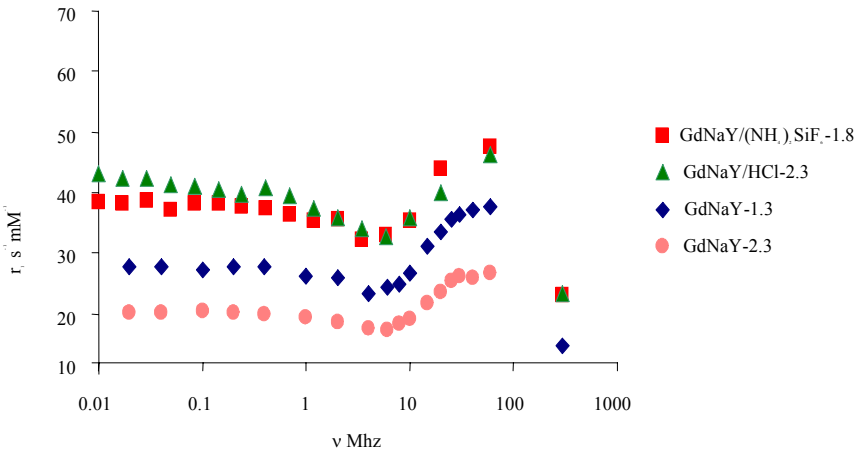


**Figure 30.** Measured NMRD curves for the dealuminated samples compared to the original GdNaY zeolites

If we compare the NMRD parameters obtained for the two dealuminated samples and for the original, non-dealuminated GdNaY zeolites with 1.3 and 2.3 weight% $Gd^{3+}$-loading, interesting conclusions can be made (Figure 31, Table 6). The $\tau_R$ rotational correlation time remained very long, indicating that the $Gd^{3+}$ ions are still successfully immobilized. The difference appears in increased $\tau_{zeo}$, which is most likely due to the increased Si/Al ratio and, therefore, slower diffusion through the more hydrophobic zeolite pore windows. The other difference is the smaller $\tau_M$, which means that the water exchange inside the zeolite becomes faster between the water molecules coordinated to the $Gd^{3+}$ ions and the water inside the zeolite pores. The *x* values increase so there are more non-coordinated water molecules per $Gd^{3+}$ ion inside the pores. The latter two parameters can be explained by the bigger pores induced by removing the Al from the framework; that could lead to "more diluted $Gd^{3+}$ solution" inside the pores.

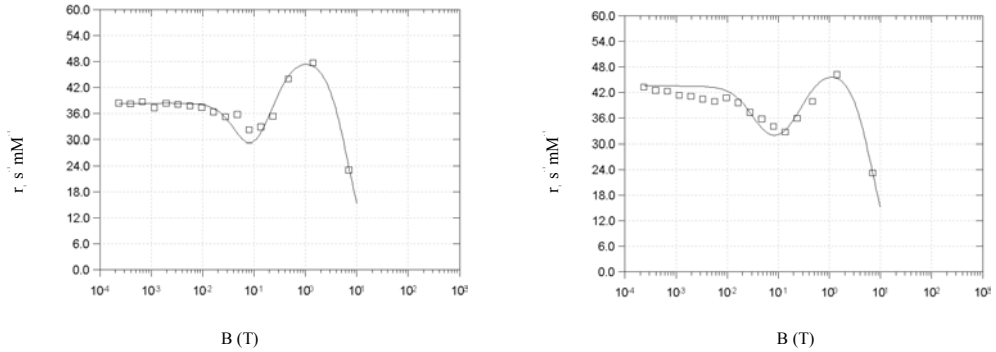


**Figure 31.** Measured and calculated NMRD curves for the dealuminated samples (left: GdNaY/$(NH_4)_2SiF6$-1.8, right: GdNaY/HCl-2.3

Recording NMRD curves was not possible in the case of GdNaA zeolites since the relaxivities were very low at lower fields and it could have caused thermal effects during continuous wave experiments at lower fields. However, at 20, 60 and 300 MHz we made measurements comparable with the original and the dealuminated GdNaY zeolites.

**Table 6.** Parameters obtained from NMRD fitting for the dealuminated samples compared to the original GdNaY samples

| | GdNaY/HCl-2.3 Si/Al=3.4 | GdNaY/$(NH_4)_2SiF6$-1.8Si/Al=2.6 | GdNaY-1.3Si/Al=1.6 | GdNaY-2.3Si/Al=1.6 |
|---|---|---|---|---|
| $\tau_R$ 310 K [s] | $>10^{-9}$ | | | |
| $\tau_{zeo}$ 310 K [$10^{-5}$ s] | 3.2±0.04 | 3.0±0.05 | 2.8 | |
| $\tau_M$ 310 K [ns] | 1.6±0.2 | 1.6±0.3 | 3.6 | 5.6 |
| x | 94±3 | 90±4 | 60±21 | 37±13 |
| $T_{2e}$ 310 K 0.34 T [$10^{-10}$ s] | 5.19 | 3.74 | 1.90 | 1.86 |

If we compare the non-dealuminated GdNaY and GdNaA samples with similar Gd-loading, we can see that the GdNaA sample has significantly lower relaxivity. (Figure 32) Since we could not made NMRD measurements in this case, our explanation remains only qualitative but we can assume that it can be connected with *i)* the lower *x* values inside the smaller pores and *ii)* the lower water exchange rate through the smaller and more hydrophobic pore windows to the bulk.

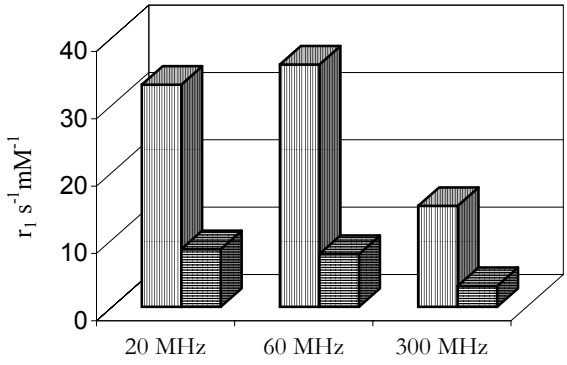


**Figure 32.** $r_1$ relaxivities of GdNaY-1.3, Si/Al = 1.6 (vertical stripes) and GdNaA-1.5 Si/Al = 1.0 (horizontal stripes) samples at 37 $^{o}$C and at different fields

The dealuminated GdNaA samples behaved differently compared to the dealuminated GdNaY samples. The "mild dealumination" increased the relaxivity, similarly to what we have seen with the GdNaY samples but it had still lower relaxivity compared to them. However, the "severe dealumination" completely destroyed the framework; it could not even retain the $Gd^{3+}$ immobilised. It reflected in very low $Gd^{3+}$-content and very low relaxivity.

The relaxivities of the non-dealuminated and mildly dealuminated GdNaA samples increased with increasing temperature (Figure 33). That is a good indication that the proton relaxivity is limited by the relatively slow water exchange, in the same way as for GdNaY.

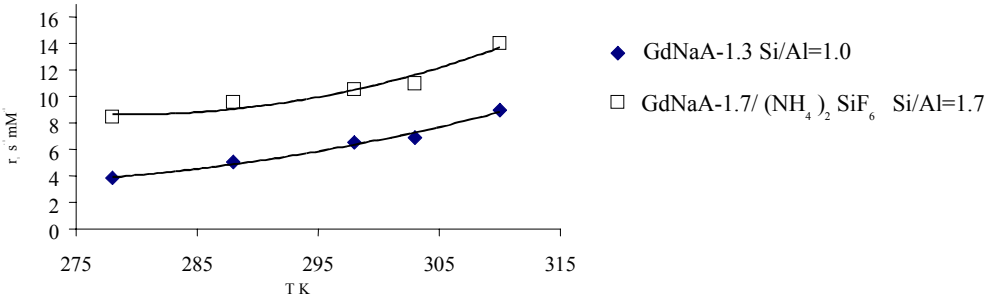


**Figure 33.** Temperature dependence of $r_1$ relaxivities of GdNaA samples at 20 MHz

It was already shown by luminescence[88] and MAS NMR spectroscopy[89] that the lanthanide ions "travel" from the supercages towards the inside of the sodalite cages. There, the water exchange is very low between the sodalite cages and the supercages or between the sodalite cages and the bulk water, so we would expect that these lanthanide ions are "lost" from our point of view, since they have not relaxivity enhancement effect. On the other hand, *x* is expected to increase with this treatment, which would lead to increased relaxivity. Therefore we studied the effect of the calcination at various temperatures on the room temperature $r_1$ and $r_2$ relaxivities (300 MHz) of the GdNaY sample with 1.3 weight% Gd.

The sample calcined at 100 $^{o}$C did not show significant change in its relaxivity. However, the sample calcined at 300 $^{o}$C already showed significant loss in the relaxivity, while the samples calcined at 400 and 500 $^{o}$C had relaxivity reduced by half, compared to the untreated GdNaY sample. (Figure 34)

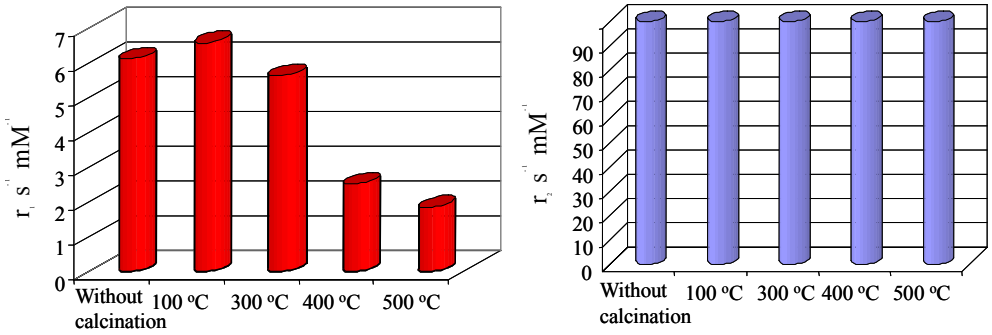


**Figure 34.** Effect of calcination on $r_1$ and $r_2$ relaxivities of GdNaY-1.3 at room temperature and at 300 MHz

Interesting result came out when we measured the transverse ($r_2$) relaxivities of the calcined samples. They did not change at all after calcination. We decided to extend the two-step exchange model to understand these unchanged $r_2$ values. Nevertheless, we wanted to check whether the parameters obtained from the NMRD fitting of the dealuminated GdNaY samples are also appropriate to describe the field dependence of the $r_2$ values measured in the same samples.

The two-step model already used for describing the field dependence of $r_1$ can also be applied for the $r_2$ values. For both processes of this two-step model, we can derive approximate equations from the exact solutions of the Bloch equations for the transverse relaxation time of a system in which two water protons undergo chemical exchange between two magnetically distinct environments A and B (Eq. 5.3.).

$$\frac{1}{T_2} = -A_2 \pm \left\{ \frac{G + \left(G^2 + H^2\right)^{1/2}}{2} \right\}^{1/2} \qquad \text{Eq. 5.6. a}$$

where

$$G = \frac{\left(\frac{1}{\tau_{2A}} - \frac{1}{\tau_{2B}}\right)^2}{4} + \frac{1}{\tau_a \tau_b} - \frac{\left(\Delta\omega_A - \Delta\omega_B\right)^2}{4} \qquad \text{Eq. 5.6. b}$$

$$H = \frac{\left(\frac{1}{\tau_{2A}} - \frac{1}{\tau_{2B}}\right)\left(\Delta\omega_A - \Delta\omega_B\right)}{2} \qquad \text{Eq. 5.6. c}$$

$$A_2 = \frac{1}{2}\left(\frac{1}{\tau_{2A}} + \frac{1}{\tau_{2B}}\right), \frac{1}{\tau_{2A}} = \frac{1}{T_{2A}} + \frac{1}{\tau_a} \qquad \text{Eq. 5.6. d}$$

In Eq. 5.6. $T_{2A}$ is the intrinsic relaxation time in the A environment, and $\tau_a$ is the residence time in the A environment. Analogous definitions apply for the B environment. $\Delta\omega_A$ and $\Delta\omega_B$ are the frequencies of the protons in the A and the B environment, respectively. Considering the B system as the water inside the zeolite cavities and the A system to constitute the bulk water, we can assume that $T_{1A} >> T_{1B}$ and $\tau_a >> \tau_b$. If we take $\Delta\omega_A = 0$ (on resonance) we obtain Eq. 5.7.

$$\frac{1}{T_2} = \frac{\frac{\left(\frac{1}{\tau_{2A}\tau_{2B}} - \frac{1}{\tau_a \tau_b}\right)}{\tau_{2B}} + \frac{\Delta\omega_B}{\tau_{2A}}}{\frac{1}{\tau_{2B}^2} + \Delta\omega_B{}^2} \qquad \text{Eq. 5.7}$$

and, consequently, $r_2$ is given by Eq. 5.8:

$$r_2 = \frac{1}{1000}\frac{(q+x)}{55.5\tau_{zeo}}\frac{\frac{1}{T_{2zeo}}\left(\frac{1}{T_{2zeo}}+\frac{1}{\tau_{zeo}}\right)+\Delta\omega_{zeo}^2}{\left(\frac{1}{T_{2zeo}}+\frac{1}{\tau_{zeo}}\right)^2+\Delta\omega_{zeo}^2} \qquad \text{Eq. 5.8}$$

in which $\Delta\omega_{zeo}$ is the frequency difference between the water in the bulk and in the zeolite cavities; the other symbols have analogous meaning like in equations describing $r_1$.

The inequality $\tau_a >> \tau_b$ does not hold for the interior of the zeolite. Therefore, to evaluate $T_{2zeo}$, we assume a chemical exchange between two magnetically distinct environments in a concentrated system; water protons in the interior of the zeolite (A environment) and water molecules coordinated to the $Gd^{3+}$ ion (B environment).

In fast exchange, where the conditions are $(1/\tau_a+1/\tau_b) >> |(1/T_{2A})-(1/T_{2B})|$ and $1/\tau_{ab} >> (\Delta\omega_A-\Delta\omega_B)$, the transverse relaxation time is given as

$$\frac{1}{T_2} = \frac{f_a}{T_{2A}} + \frac{f_b}{T_{2B}} + f_a f_b \tau_{ab}\left(\Delta\omega_A - \Delta\omega_B\right)^2 \qquad \text{Eq. 5.9}$$

where $f_a$ and $f_b$ are the mole fractions and $\tau_{ab}$ is given as $1/\tau_{ab} = 1/\tau_a + 1/\tau_b$. If we take $\Delta\omega_A=0$ and we substitute the parameters used for the two-site system in the zeolite cavities we obtain Eq. 5.10:

where $f_a$ and $f_b$ are the mole fractions and $\tau_{ab}$ is given as $1/\tau_{ab} = 1/\tau_a + 1/\tau_b$. If we take $\Delta\omega_A=0$, we obtain Eq. 5.10, describing $1/T_{2,zeo}$ in the zeolite interior cavities:

$$\frac{1}{T_{2,zeo}} = \frac{x}{(x+q)T_{2,water}} + \frac{q}{(x+q)T_{2m}} + \frac{xq}{(x+q)}\tau_m \left(\Delta\omega_m\right)^2 \qquad \text{Eq. 5.10}$$

in which $T_{2m}$ is the transverse relaxation time of inner sphere water protons, $T_{2,water}$ is the transverse relaxation time of water protons not coordinated to $Gd^{3+}$ in the zeolite cavities and $\Delta\omega_m$ is the chemical shift difference induced by the $Gd^{3+}$ ions. The other parameters have the same meaning as above.

Similarly to the model describing $T_{1m}$, first we assumed that $T_{2m}$ is mainly governed by the dipole-dipole interactions. Then, $T_{2m}$ is described by Eq 2.7. Since the parameters determining $T_{2m}$ are the same as the ones for $T_{1m}$, we performed a simulation to estimate the field dependence of $T_{2m}$ compared to $T_{1m}$, based strictly on the dipole-dipole interaction. For this calculation we used the parameters obtained from the $r_1$ fitting in the case of the GdNaY/F-1.8 sample.

We found that at lower fields $T_{1m}$ and $T_{2m}$ are equal, while, because of the $4\tau_{c1}$ term, at higher fields (> 0.1 T) $T_{2m}$ gradually becomes shorter than $T_{1m}$ and above 1 T the difference becomes significant. From the simulation we could estimate the length of $T_{2m}$ to be less than $3 \cdot 10^{-6}$ s in the whole field range.

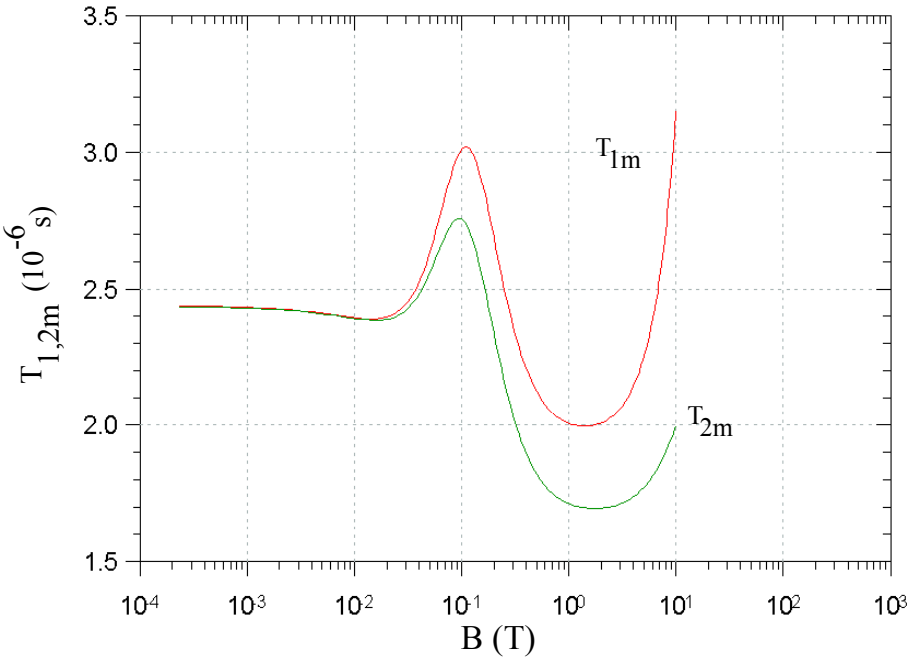


**Figure 35.** $T_{1m}$ and $T_{2m}$ vs. $B$ according to the model using dipole-dipole contact mechanism and the parameters obtained for GdNaY/ $(NH_4)_2SiF_6$-1.8

Therefore we can state that in Eq. 5.10 the first term is negligible compared to the second term, containing $1/T_{2m}$. With a simple calculation, using the parameters obtained for the GdNaY/F-1.8 sample, we obtain that to have the third term comparable with the second term, we should have a chemical shift difference about $10^{14}$ ppm at 300 MHz. Consequently, Eq. 5.10 can be simplified to Eq. 5.11.

$$\frac{1}{T_{2,zeo}} = \frac{q}{(x+q)T_{2m}} \qquad \text{Eq. 5.11}$$

A model calculation using Eqs 5.8, 5.12 and 5.11 and the parameters obtained from the $r_1$ fitting of the NMRD curve of GdNaY/F-1.8 showed that even with gradually increased $\Delta\omega_{zeo}$ we can not reach the high $r_2$ values measured at 300 MHz. The maximum $r_2$ obtained with this model and with these parameters is around 60 $mM^{-1}s^{-1}$, while the measured $r_2$ at 300 MHz is 120 $mM^{-1}s^{-1}$.

In the particulate contrast agents, the Curie contribution is often very high, mainly in $r_2$ and mainly at high field. Therefore we integrated the Curie terms both in $T_{1m}$ and $T_{2m}$, according to Eqs 2.15 and 2.16, resulting Eqs 5.12 and 5.13.

$$\frac{1}{T_{1m}} = \frac{1}{T_{1m}^{DD}} + \frac{1}{T_{1m}^{C}} = \frac{2}{15}\left(\frac{\gamma_I^2 g^2 \mu_B^2}{r_{GdH}^6}\right) S(S+1)\left(\frac{\mu_0}{4\pi}\right)^2 \left(7\frac{\tau_{c2}}{1+\omega_s^2\tau_{c2}^2} + 3\frac{\tau_{c1}}{1+\omega_I^2\tau_{c1}^2}\right) +$$
$$+\frac{2}{5}\left(\frac{\mu_0}{4\pi}\right)^2 \gamma_I^{\,2} B_0^{\,2} \mu_B^{\,4} g^4 S^2 (S+1)^2 \frac{1}{r^6}\frac{1}{(3k_B T)^2}\left[\frac{3\tau_{CC}}{1+\omega_I^{\,2}\tau_{CC}^{\,2}}\right]$$

Eq. 5.12

$$\frac{1}{T_{2m}} = \frac{1}{T_{2m}^{DD}} + \frac{1}{T_{2m}^{C}} = \frac{1}{15}\left(\frac{\gamma_I^2 g^2 \mu_B^2}{r_{GdH}^6}\right) S(S+1)\left(\frac{\mu_0}{4\pi}\right)^2 \left(13\frac{\tau_{c2}}{1+\omega_s^2\tau_{c2}^2} + 3\frac{\tau_{c1}}{1+\omega_I^2\tau_{c1}^2} + 4\tau_{c1}\right) +$$
$$+\frac{1}{5}\left(\frac{\mu_0}{4\pi}\right)^2 \gamma_I^{\,2} B_0^{\,2} \mu_B^{\,4} g^4 S^2 (S+1)^2 \frac{1}{r^6}\frac{1}{(3k_B T)^2}\left[4\tau_{CC} + \frac{3\tau_{CC}}{1+\omega_I^{\,2}\tau_{CC}^{\,2}}\right]$$

Eq. 5.13

In Figure 36, we can see that the Curie contribution in $T_{2m}$ is negligible since $T_{1m}^{C}$ is very long. However, the Curie contribution in $T_{2m}$ is also smaller compared to the dipole-dipole contribution, even at 300 MHz because $T_{2m}^{C}$ is here still one order of magnitude longer than $T_{2m}^{DD}$.

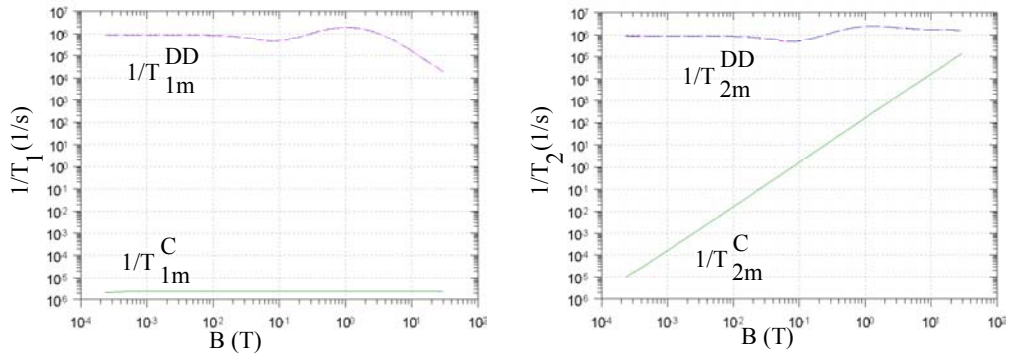


**Figure 36.** Calculated dipole-dipole and Curie contributions in $1/T_{1m}$ and $1/T_{2m}$

Another explanation could be for the high $r_2$ values that these particles have superparamagnetic effect expressed in $T_2$ shortening. Superparamagnetic particles not only have a much greater magnetisation as compared *e. g.* to the widely used $Gd^{3+}$-complexes, but also this magnetisation has a component oriented along the external field, which does not fluctuate with time in direction. In a widely used model, the water dispersion of these superparamagnetic particles is treated as a heterogenous system, composed of randomly distributed, stationary magnetic spheres surrounded by water

proton spins with unrestricted, isotropic diffusion.[90] Only the relaxation caused by the interaction between the magnetic spheres and the nearby spins (within the effective range of the spheres' dipole field) is considered.

In our case, the possibility of superparamagnetism is further supported by the calcination experiment on GdNaY-1.3 because the position of the $Gd^{3+}$ ions is not expected to alter the diffusion rate of the water molecules outside the zeolite particles.

Based on this model, two frequency scales are present, each characterising one relaxation mechanism: the dynamic frequency scale and the magnetic frequency scale.

The dynamic frequency scale is the diffusion rate $1/\tau$, and it specifies how fast the spins are relaxed during the imaging time, on average, by the randomly distributed magnetic spheres they encounter as they move about. $\tau$, the translational correlation time is defined by Eq. 5.14.

$$\tau = R^2 / D \qquad \text{Eq. 5.14}$$

Here, $D$ is the translational diffusion coefficient of the spins relative to the magnetic spheres, and $R$ is the radius of the magnetic sphere.

The magnetic frequency scale is defined as the equatorial field $(B_{eq}(R))$ in frequency units, determined by Eq. 5.15.

$$\delta\omega = \gamma B_{eq}(R) = \gamma \frac{4\pi}{3} \Delta\chi B_0 \qquad \text{Eq. 5.15}$$

Here, $\gamma$ is the proton gyromagnetic ratio, $\Delta\chi$ is the susceptibility difference between the sphere and its surroundings, $B_0$ is the external field. In other words, $\delta\omega$ represents the characteristic Larmor frequency difference at the equator surface due to the field perturbation caused by the presence of the sphere, as it is experienced by the nearby spins.

Based on the relative magnitude of these two characteristic frequencies, the relaxation behaviour of these spin-sphere systems can be categorised in five diffusion regimes. The empirical equations describing the transverse relaxation rates in these regimes are given as follows:

In the outer-sphere $(1/\tau >> \delta\omega)$ and in the fast diffusion $(1/\tau > \delta\omega)$ regimes, the empirical equations show squared $\delta\omega$ dependence, therefore squared $B_0$ dependence.

$$\frac{1}{T_2} = af\frac{R^2}{D}\left(\delta\omega\right)^2 = af\frac{R^2}{D}\left(\gamma\frac{4\pi}{3}\Delta\chi B_0\right)^2 \qquad \text{Eq. 5.16}$$

Here, $a$ is a proportionality constant, and $f$ is the volume fraction of the magnetic spheres in the medium.

In the slow diffusion regime $(1/\tau < \delta\omega)$, the transverse relaxation rate is derived according to Eq. 5.17, not showing $B_0$ dependence.

$$\frac{1}{T_2} \approx f\frac{\sqrt{D}}{R} \qquad \text{Eq. 5.17}$$

In the static dephasing regime *(1/*$\tau$ <<$\delta\omega$*)*, *R* approaches infinity in Eq. 5.17, therefore transverse relaxation rate enhancement is not observed.

In the intermediate regime, where *1/*$\tau$ and $\delta\omega$ are comparable, the following empirical equation was proposed:[90]

$$\frac{1}{T_2} = f(\delta\omega)\frac{a\left(\sqrt{\frac{\delta\omega}{D}}R\right)^2}{1+\frac{a}{b}\left(\sqrt{\frac{\delta\omega}{D}}R\right)^3} \qquad \text{Eq. 5.18}$$

Here, the field dependence of the transverse relaxation rate shows a maximum curve. Regarding Eqs 5.16-5.18, already the nature of the field-dependent $r_2$ relaxivity curve could give an impression about the diffusion regime the system under study belongs to.

To obtain further information on $r_2$ (and $r_1$) field dependence, we performed $T_2$ (and $T_1$) measurements also at 500 MHz. The obtained curves both for GdNaY/$(NH_4)_2SiF6$-1.8 and GdNaY/HCl-2.3 showed maximum at 300 MHz in $r_2$ (while they both showed monoton decrease in $r_1$) (Figures 37, 38). Therefore we can assume that these systems are in the intermediate regime, where *1/*$\tau$ and $\delta\omega$ have comparable values.

These (modified) GdNaY zeolite nanoparticles show significant $r_1$ enhancement at lower fields, where the traditional MRI works. However, at the higher fields of the recently designed MRI equipments they can be used

as $r_2$-enhancing contrast agents, due to their large superparamagnetic contribution.

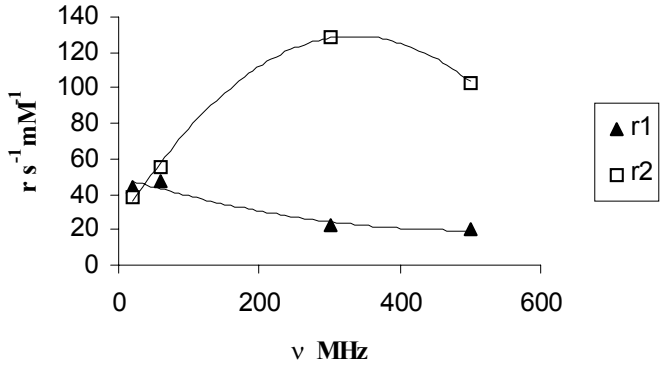


**Figure 37.** Field dependence of $r_1$ and $r_2$ relaxivities in water dispersion of GdNaY/$(NH_4)_2SiF_6$-1.8 zeolite

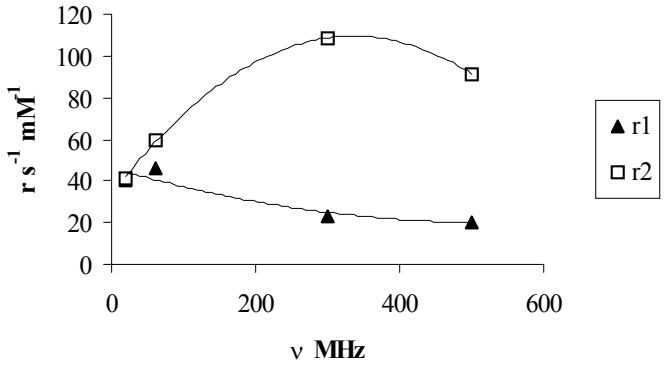


**Figure 38.** Field dependence of $r_1$ and $r_2$ relaxivities in water dispersion of GdNaY/HCl-2.3 zeolite.

# 6 Summary

This thesis deals with structural and dynamic aspects of several compounds related to contrast agents of current or promising use in medical imaging techniques. We have studied: *i)* the structure and dynamics of an inert and a labile complex of the macrocyclic DOTA ligand ($(BiDOTA)^-$ and $K(H_xDOTA)^{(3-x)-}$, *ii)* the effect of C5-substitution on the structure and dynamics of the DTPA-skeleton ($Lu(S\text{-}EOB\text{-}DTPA)^{2-}$) *iii)* the effect of the pore size, the Si/Al ratio and the calcination on the relaxivity of Gd-loaded zeolite nanoparticles. The main tool for these studies was the NMR spectroscopy, but x-ray diffraction (powder or single crystal), NMR relaxometry, or ICP was also used to gain more information.

In Chapter 3 we continued to search that in what extent the DOTA ligand itself is responsible for the intramolecular motions of the metal - DOTA complexes and what is the new feature brought about by the formed complex, which is a special assembly of the metal ion and the ligand. In the case of $Bi(DOTA)^-$, a potential CT contrast agent, the isomeric composition has been studied and compared with the results obtained for the $Ln(DOTA)^-$ complexes. We have found that the $Bi(DOTA)^-$ prefers the twisted square antiprismatic (TSA) arrangement, similarly to DOTA complexes formed with the larger lanthanide ions. By VT $^1H$ NMR spectroscopy and the 2D EXSY spectra taken at 274 K, the dynamic behaviour of the complex has also been revealed. The observed fluxionalities correspond *i)* to the motion of the ring

protons and *ii)* to the change of the acetate arms' helicity. With the notation introduced for DOTA complexes, these fluxionalities are *i)* the *(*δδδδ*)*↔ *(*λλλλ*)* rearrangement for the ring and *ii)* the Δ↔Λ rearrangement for the acetate arms. The similar activation parameters obtained for the ring inversion and for the change in the acetate arms' helicity (Table 4) support the suggestion of Jacques *et al.* based on $^{1}$H-$^{1}$H 2D EXSY measurements on the complex Yb(DOTA)$^{-}$; that the two types of motions, *i.e.* the motion of the ring and the acetate arms, proceed at the same rate in a concerted way.[49] Another explanation can be a two-step mechanism where the slow, rate-determining ring inversion is followed by a fast change in the acetate arms' helicity.[55] Since the Λ*(*λλλλ*)*/Δ*(*δδδδ*)* enantiomer pair cannot be detected, both accounts can be applied to explain our results.

Besides these types of fluxionalities, a new type of ring motion appears in the case of K(DOTA)$^{3-}$ at pH~13. This ring-proton exchange process requires metal-ligand bond breaking and leads to we called the ring-slewing motion (Figure 17). This fluxionality, therefore, could not be detected in the case of inert lanthanide-DOTA complexes. According to our finding, carbon exchange does not take place during the ring slewing, only the geminal protons switch their positions. This observation served as an excellent tool to separate the two different types of ring motions.

The analysis of the activation parameters showed that at lower temperatures the ring inversion is the main ring motion, while the simultaneously existing ring slewing occurs much slower. The change in the acetate arms' helicity accompanies the ring inversion with similar rate. However, as the temperature increases the $K^{+}$ ion can dissociate more easily from the DOTA,

giving rise to the new type of ring motion, the ring slewing. Interestingly, at high temperature the change in the acetate arms' helicity follows the ring slewing; while the ring inversion has slower rate, compared to the other two motions. We may state that the change in helicity of acetate arms is not an independent form in the fluxionality of $K(DOTA)^{3-}$ complex.

By line shape analysis of the HDO- $K(H_xDOTA)^{(3-x)-}$ system at lower pH, we have found that besides the intramolecular dynamic processes, exchange occurs also between HDO and $K(H_xDOTA)^{(3-x)-}$. It is difficult to identify what kind of DOTA complex can exchange protons slowly at pH around 4 with water, however, keeping in mind the exceptional stability of diprotonated $H_2DOTA^{2-}$, we suppose that an ion pair between this anion and $K^+$ can be responsible for this phenomenon. This $K(H_2DOTA)^-$ can be protonated, forming $K(H_3DOTA)$ assembly, which contains exchangeable protons with HDO. The potassium probably has an "out-of-cage" position, but it can also slow down the intramolecular motion of the macrocycle, leading to line broadening in both of the ring and acetate-methylene proton signals of DOTA (Figure 13). At pH between 6 and 9.5, where $H_2DOTA^{2-}$ and $HDOTA^{3-}$ (both partially containing $K^+$) species are present, the detected proton exchange with HOD is in the *slow exchange regime*, while the fluxionality is *in the fast exchange regime.*

In Chapter 4, we studied what are the structural and dynamic consequences of introduction of an ethoxybenzyl-group into the 5-position in the Lu(*S*-EOB-DTPA)$^{2-}$ complex. At 330 K, two sets of signals appear both in $^{13}C$ and $^{1}H$-NMR, which were assigned to isomers differing in the configuration of the central nitrogen, with ratio 35:65. At temperatures lower than 300 K, the

lines of the two isomers showed separate broadening. This observation is a consequence of the change in the acetate arms' helicity, "wagging", which is observable on the NMR time scale. By analysing the coupling patterns of the ethylene-diamine protons we determined that in both cases the preferred (and only detectable) arrangement of the acetate arms corresponds to the Λ helicity.

In Chapter 5, our aim was to study systematically the effect of changing various parameters as Si/Al ratio within the zeolite framework, pore size and $Gd^{3+}$ distribution on the $r_1$ relaxivity. To gain more information about the mechanism, $r_2$ transverse relaxivities were also measured at higher fields, and equations were worked out for interpreting the results. Dealumination of zeolites is an often-applied method to gain zeolites with higher Si/Al molar ratio in the framework, which makes them more hydrophobic. However, with dealumination we also create vacancies in the zeolite framework by (partly) removing the Al, so loss in crystallinity and appearance of extra pores can also occur. Dealumination of the Y framework resulted in higher relaxivities of the GdNaY system, which can be explained by the larger water content inside the zeolite pores, overcompensating the slower diffusion through the more hydrophobic zeolite pore windows, as it was shown by NMRD fittings.. If we compare the non-dealuminated GdNaY and GdNaA samples with similar Gd-loading, we see that the GdNaA sample has significantly lower relaxivity, due to the smaller pores (lower water content inside the zeolite pores) and smaller pore windows (slower diffusion), as it was shown by NMR relaxometry.

The calcination induced $Gd^{3+}$-"travelling" inside the Y framework from the larger pores towards the smaller ones, which have very slow water diffusion rate towards the larger pores and the bulk in the NMR time scale. It resulted in reduced $r_1$ values. However, $r_2$ transverse relaxivities did not change upon calcination. This result and the fact that using the dipolar mechanism to describe the magnetic field dependence of $r_2$ was unsuccessful in the case of dealuminated GdNaY samples lead to the conclusion that outer-sphere effects play significant role in the transverse relaxivities. $r_2$ values measured at 20, 60, 300 and 500 MHz for the dealuminated GdNaY samples showed a maximum at 300 MHz, therefore by help of the available empirical equations we could assume that these systems are in the intermediate regime, where $1/\tau$ (diffusion rate of the bulk water around the zeolite particles) and $\delta\omega$ (the characteristic Larmor frequency difference at the equator surface due to the field perturbation caused by the presence of the sphere) have comparable values.

# 7 Összefoglalás

Az értekezésben az orvosi képalkotó módszerekben eredményesen használt vagy ígéretes tulajdonságokat mutató kontrasztanyagokkal kapcsolatos szerkezeti és dinamikai vizsgálatainkat mutatjuk be. Ph.D. munkám során a következő témákkal foglalkoztam:

- egy inert ($(BiDOTA)^-$) és egy labilis ($K(H_xDOTA)^{(3-x)-}$) DOTA-komplex szerkezetének és dinamikájának felderítése
- C5-helyzetű szubsztitúció hatásának tanulmányozása a DTPA alapvázat tartalmazó komplexek esetében a $Lu(S\text{-}EOB\text{-}DTPA)^{2-}$ példáján
- a pórusméret, a Si/Al arány és a kalcinálás hatásának vizsgálata Gd-tartalmú zeolit nanorészecskék esetén.

Ezekhez a vizsgálatokhoz a fő eszköz az NMR spektroszkópia volt, de por- és egykristály-röntgendiffrakciót, NMR relaxometriát, illetve ICP-t is használtunk kiegészítő információk megszerzésére. A 3. és 4. fejezetben található eredményeket a Debreceni Egyetem Fizikai Kémiai Tanszékén végzett munka során értük el. Az 5. fejezetben leírtak a Delfti Műszaki Egyetemen Marie Curie ösztöndíjasként végzett munkám összefoglalása.

A 3. fejezetben azt kutattuk, milyen mértékben felelős maga a DOTA ligandum a DOTA fémkomplexeinél detektált belső mozgásért, és mi az új tulajdonság, amit a már kialakult komplex eredményez. A $Bi(DOTA)^-$ esetében, ami egy potenciális CT kontrasztanyag, megvizsgáltuk a komplex izomerösszetételét és az eredményeket összehasonlítottuk a széleskörűen

tanulmányozott $Ln(DOTA)^-$ komplexekkel. Azt találtuk, hogy a $Bi(DOTA)^-$ a csavart négyzetes antiprizmás (twisted square antiprismatic, TSA) elrendeződést preferálja, hasonlóan a nagyobb méretű lantanida ionok DOTA komplexeihez. A $^1$H-NMR spektrumok hőmérsékletfüggése és a 274 K-en felvett 2D EXSY spektrum segítségével felderítettük a rendszer dinamikáját. A detektált fluxionális mozgások a következők: i) a gyűrű mozgása, amely gyűrűprotonok közti cserefolyamatot jelent ii) az acetát karok helicitásának megváltozása, amit az acetát-metilén protonok közötti cserefolyamattal detektálhatunk. A DOTA komplexeknél bevezetett jelölésekkel, ezek a fluxionalitások *i)* a $(\delta\delta\delta\delta) \leftrightarrow (\lambda\lambda\lambda\lambda)$ átalakulás a gyűrűben, illetve *ii)* a $\Delta \leftrightarrow \Lambda$ átalakulás az acetát karok helicitásában. Hasonló aktiválási paramétereket kaptunk a kétféle mozgásra (4. táblázat), ami alátámasztja Jacques *et al.* javaslatát, amelyet $Yb(DOTA)^-$ $^1$H-$^1$H 2D EXSY vizsgálata alapján tettek, miszerint a kétféle mozgás ugyanazzal a sebességgel, egyidőben játszódik le. Egy másik magyarázat lehet egy kétlépéses mechanizmus, ahol a lassú, sebességmeghatározó gyűrűinverziót követi a gyors váltás az acetát-karok helicitásában. Mivel a $\Lambda(\lambda\lambda\lambda\lambda)/\Delta(\delta\delta\delta\delta)$ enantiomer párt nem detektáltuk, mindkét megközelítést alkalmazhatjuk tapasztalataink értelmezésére.

Emellett a két fluxionalitás mellett, egy új típusú gyűrűmozgás jelenik meg a $K(DOTA)^{3-}$ esetén pH~13 körül. Az újfajta gyűrűmozgás a 17. ábrán látható módon a fém-ligandum kötés felhasadását igényli, ezért ez nem észlelhető az inert lantanida-DOTA komplexeknél. Azt találtuk, hogy ennél az új mozgásnál, amelyet gyűrűátfordulásnak neveztünk el, a gyűrű szénatomjai nem cserélnek pozíciót, csak a geminális protonok. Ez a megfigyelés alapot

adott arra, hogy a kétféle (a régi és az új) gyűrűmozgást megkülönböztessük egymástól.

Az aktiválási paraméterek elemzése az mutatta, hogy alacsony hőmérsékleten a gyűrűinverzió a fő gyűrűmozgás, míg a szintén jelenlévő gyűrűátfordulás sokkal lassabb. az acetát karok mozgása a gyűrűmozgást követi. Magasabb hőmérsékeleten a $K^+$-ion könnyebben disszociál a komplexből, így az új mozgás, a gyűrűátfordulás előtérbe kerül. Érdekes tapasztalat, hogy magasabb hőmérsékleten az acetát-karok mozgása a gyűrűátfordulást követi, míg a gyűrűinverzió a másik két mozgáshoz képest sokkal kisebb sebességgel zajlik. Mindezek alapján megállapíthatjuk, hogy az acetát-karok mozgása nem független a gyűrűmozgástól a $K(DOTA)^{3-}$ komplex esetén.

Vonalszélesség-vizsgálatok alapján azt találtuk, hogy a HDO- $K(H_xDOTA)^{(3-x)-}$ rendszerben kisebb pH-n az intramolekuláris cserefolyamatok mellett cserefolyamat zajlik a HDO és a $K(H_xDOTA)^{(3-x)-}$ között. Azt nehéz volna meghatározni, milyen DOTA complex mutat lassú protoncserét a vízzel pH=4 körül, azonban, felidézve a diprotonált $H_2DOTA^{2-}$ részecske nagy stabilitását, feltételezzük, hogy egy e részecske és a $K^+$-ion között kialakuló ionpár felelős ezért a jelenségért. A $K(H_2DOTA)^-$ részecske tovább is protonálódhat, és a kialakuló $K(H_3DOTA)$ tartalmaz olyan protonokat, melyek a HDO-val cserereakcióba léphetnek. A káliumion feltehetően a koordinációs üregen kívül helyezkedik el és csak az acetát-karokhoz koordinálódik, de még így is lelassíthatja a makrociklus mozgását, jelszélesedést eredményezve a DOTA gyűrű-és acetát-metilén proton jelein (13. ábra). pH=6-9,5 között, ahol (részben K+-ionokat koordináló) $H_2DOTA^{2-}$ and $HDOTA^{3-}$ részecskék vannak jelen, szobahőmérsékleten a

detektált intermolekuláris protoncserefolyamat a HDO-val lassú, míg a fluxionalitás gyors az NMR időskálán.

A 4. fejezetben azt tanulmányoztuk, milyen szerkezeti és dinamikai következményei vannak, ha a DTPA molekulát az 5-ös helyzetben egy etoxibenzil-csoporttal szubsztituáljuk. Ezeket a következményeket a Lu(*S*-EOB-DTPA)$^{2-}$ komplex konkrét esetén vizsgáltuk. 330 K hőmérsékleten, két külön jelkészletet detektáltunk mind a $^{13}$C, mind a $^{1}$H NMR spektrumban, amelyeket két, egymástól a központi N-atom konfigurációjában különböző izomerként azonosítottunk, melyek aránya 35:65. 300 K-nél kisebb hőmérsékleten, a két izomerhez tartozó jelek egymástól független jelszélesedést mutattak a hőmérséklet csökkenésével. Ezt az acetát-karok helicitásának változásával magyaráztuk. Az etilén-diamin protonok közötti csatolások elemzésével meghatároztuk, hogy az acetát karok preferált (és így kizárólagosan detektálható) elrendeződése mindkét izomernél a Λ-val jelölt helicitásnak felel meg.

Az 5. fejezetben Gd-tartalmú zeolit nanorészecskék vizes diszperziójában mért $r_1$ relaxivitásának változását vizsgáltuk különböző paraméterek, mint a pórusméret, a Si/Al arány változtatása és a kalcinálás hatására. Hogy a mechanizmusról több információt nyerjünk, $r_2$ relaxivitásokat szintén mértünk magasabb térerőkön és különböző, irodalomból ismert egyenletekkel próbáltuk magyarázni a tapasztalatokat.

A dealuminálás egy általános módszer nagyobb Si/Al mólarányú, így nagyobb hidrofóbicitású zeolitok előállítására. A dealuminálás azonban Al eltávolításával jár a szerkezetből, így a kristályszerkezet szabályossága romlik, extra pórusok jelennek meg. Az Y szerkezet dealuminálása

relaxivitásnövekedéssel járt a GdNaY zeolitok esetében, amit NMRD illesztéseink alapján a pórusok megnövekedett víztartalmával magyaráztunk, amely ellentételezte a megnövekedett hidrofóbicitásúvá vált zeolit pórusnyílásokon keresztüli lassabb vízdiffúziót. Az eredeti, nem dealuminált, hasonló Gd-tartalmú GdNaY és GdNaA minták öszehasonlításakor azt tapasztaltuk, hogy a GdNaA mintának sokkal kisebb a relaxivitása, amelyet a kisebb pórusokkal (kisebb belső víztartalom) és kisebb pórusnyílásokkal (lassabb diffúzió) magyaráztunk.

A kalcinálás a $Gd^{3+}$-ionok részleges vándorlását eredményezte az Y zeoliton belüli nagyobb üregekből a kisebb üregek felé, amelyek azonban az NMR időskálán igen lassan cserélnek vizet mind a nagyobb pórusokkal, mind a zeoliton kívüli vízzel. Ez az $r_1$ értékek csökkenését eredményezte, azonban az $r_2$ értékek nem változtak. Ez a tapasztalat, és az, hogy a dealuminaált GdNaY minták esetén $r_2$ térerőfüggését nem tudtuk a dipoláris mechanizmussal leírni, ahhoz a következtetéshez vezetett, hogy külső szférás hatások jelentős szerepet játszanak a mért magas transzverzális relaxivitás kialakulásában. 20, 60, 300 és 500 MHz-en mért $r_2$ relaxivitások a dealuminált GdNaY minták esetében maximumot mutattak 300 MHz-en. A rendelkezésre álló empírikus egyenletek segítségével megállapítottuk, hogy a vizsgált rendszerek abban a tartományban vannak, ahol $1/\tau$ (a víz diffúziósebessége a zeolit részecskék körül) és $\delta\omega$ (a paramágneses részecske által létrehozott mágneses tér perturbáció indukálta Larmor-frekvenciakülönbség a részecske közelében) hasonló nagyságrendűek.

# 8 References


1. Yu, S.-B.; Watson, A. D. *Chem. Rev.* **1999**, *99*, 2353-2377.
2. Nobel E-Museum www.nobel.se Copyright © 2004. The Nobel Foundation
3. Freeman, R. *Magnetic Resonance in Chemistry and Medicine*; Oxford University Press, Inc.: New York, 2003.
4. Hornak, J. P. The Basics of MRI. A hypertext book on magnetic resonance imaging www.cis.rit.edu/htbooks/mri/ Copyright © 1996-2003 J. P. Hornak
5. Bradley, W. G.; Adey, W. R.; Hasso, A. N. *Magnetic Resonance Imaging of the Brain, Head and Neck - A Text Atlas*; Aspen Publishers, Inc.: Rockville, Maryland, 1985.
6. Lammers, H.; van der Heiden, A. M.; van Bekkum, H.; Geraldes, C. F. G. C.; Peters, J. A. *Inorg. Chim. Acta* **1998**, *268*, 249-255.
7. Sarka, L.; Burai, L.; Brücher, E. *Chem. Eur. J.* **2000**, *6*, 719-724.
8. Caravan, P.; Ellison, J. J.; McMurry, T. J.; Lauffer, R. B. *Chem. Rev.* **1999**, *99*, 2293-2352.
9. Swift, T. J.; Connick, R. E. *J. Chem. Phys.* **1962**, *37*, 107.
10. Luz, Z.; Meiboom, S. *J. Chem. Phys.* **1964**, *40*, 2686.
11. Solomon, I. *Phys. Rev.* **1955**, *99*, 559.
12. Bloembergen, N. *J. Chem. Phys.* **1957**, *27*, 572.
13. Bloembergen, N.; Morgan, L. O. *J. Chem. Phys.* **1961**, *34*, 842.

14. McLahlan, A. D. *Proc. R. Soc. London* **1964**, *A280*, 271.
15. Koenig, S. H.; Kellar, K. E. *Magn. Reson. Med.* **1995**, *34*, 227-233.
16. Vander Elst, L.; Roch, A.; Gillis, P.; Laurent, S.; Botteman, F.; Bulte, J. W. M.; Muller, R. N. *Magn. Reson. Med.* **2002**, *47*, 1121-1130.
17. Gueron, M. *J. Magn. Reson.* **1975**, *19*, 58-66.
18. Freed, J. H. *J. Chem. Phys.* **1978**, *68*, 4034.
19. Koenig, S. H.; Brown, R. D. I. *Prog. Nucl. Magn. Reson. Spectrosc.* **1990**, *22*, 487.
20. Wolff, S. D.; Balaban, R. S. *Magn. Reson. Med.* **1989**, *10*, 135-144.
21. Ward, K. M.; Aletras, A. H.; Balaban, R. S. *J. Magn. Reson.* **2000**, *143*, 79-87.
22. Zhang, S.; Winter, P.; Wu, K.; Sherry, A. D. *J. Am. Chem. Soc.* **2001**, *123*, 1517-1518.
23. Zhang, S.; Merrit, M.; Woessner, D. E.; Lankinski, R. E.; Sherry, A. D. *Acc. Chem. Res.* **2003**, *36*, 783-790.
24. Woods, M.; Zhang, S.; Von Howard, E.; Sherry, A. D. *Chem. Eur. J.* **2003**, *9*.
25. Aime, S.; Castelli, D. D.; Terreno, E. *Angew. Chem. Int. Ed.* **2002**, *41*, 4334-4336.
26. Zhang, S.; Michaudet, L.; Burgess, S.; Sherry, A. D. *Angew. Chem. Int. Ed.* **2002**, *41*, 1919-1921.
27. Aime, S.; Barge, A.; Castelli, D. D.; Fedeli. F.; Mortillaro, A.; Nielsen, F. U.; Terreno, E. *Magn. Reson. Med.* **2002**, *47*, 639-648.
28. Balkus, K. J.; Bresinska, I. *Journal of Alloys and Compounds* **1994**, *207/208*, 25-28.

29. Balkus, K. J.; Shi, J. *Langmuir* **1996**, *12*, 6277-6281.
30. Bresinska, I.; Balkus, K. J. *J. Phys. Chem.* **1994**, *98*, 12989-12994.
31. Bryant, R. G.; Listinsky, J. J. **1990** U.S. US 4,927,624
32. Sur, S. K.; Heinsbergen, J. F.; Bryant, R. G. *Journal of Magnetic Resonance, Series A* **1993**, *103*, 27-33.
33. Sur, S. K.; Heinsbergen, J. F.; Bryant, R. G. *Journal of Magnetic resonance A* **1993**, *103*, 8-12.
34. Braybrook, J. H.; Hall, L. D. *Carbohydrate Research* **1989**, *187*, c6-c8.
35. Braybrook, J. H.; Hall, L. D. *Polymer International* **1991**, *26*, 251-259.
36. Platas-Iglesias, C.; Elst, L. V.; Zhou, W.; Muller, R. N.; Geraldes, C. F. G. C.; Maschmeyer, T.; Peters, J. A. *Chem. Eur. J.* **2002**, *8*, 5121-5131.
37. Reynolds, C. H.; Annan, N.; Beshah, K.; Huber, J. H. *J. Am. Chem. Soc.* **2000**, *122*, 8940-8945.
38. Glogard, C.; Stensrud, G.; Klaveness, J. *International Journal of Pharmaceutics* **2003**, *253*, 39-48.
39. Krause, W. *Top. Curr. Chem.* **2002**, *222*.
40. Peters, J. A.; Zitha-Bovens, E.; Corsi, D. M.; Geraldes, C. F. G. C. In *The Chemistry of Contrast Agents in Medical Magnetic Resonance Imaging*; Merbach, A. E., Tóth, É., Eds.; John Wiley & Sons, Ltd.: New York, 2001.
41. Shannon, R. D. *Acta Cryst.* **1976**, *A32*, 751-767.
42. Peters, J. A. *Inorg. Chem.* **1988**, *27*, 4686-4691.

43. Jenkins, B. G.; Lauffer, R. B. *Inorg. Chem.* **1988**, *27*, 4730-4738.
44. Micskei, K.; Helm, L.; Brücher, E.; Merbach, A. E. *Inorg. Chem.* **1993**, *32*, 3844-3850.
45. Benetollo, F.; Bombieri, G.; Calabi, L.; Aime, S.; Botta, M. *Inorg. Chem.* **2003**, *42*, 148-157 and the references herein.
46. Desreux, J. F. *Inorg. Chem.* **1980**, *19*, 1319-1324.
47. Aime, S.; Botta, M. *Inorg. Chim. Acta* **1990**, *177*, 101-105.
48. Aime, S.; Botta, M.; Ermondi, G. *Inorg. Chem.* **1992**, *31*, 4291-4299.
49. Jacques, V.; Desreux, J. F. *Inorg. Chem.* **1994**, *33*, 4048-4053.
50. Aime, S.; Barge, A.; Botta, M.; Fasano, M.; Ayala, J. D.; Bombieri, G. *Inorg. Chim. Acta* **1996**, *246*, 423-429.
51. Aime, S.; Botta, M.; Fasano, M.; Marques, M. P. M.; Geraldes, C. F. G. C.; Pubanz, D.; E., M. A. *Inorg. Chem.* **1997**, *36*.
52. Hoeft, S.; Roth, K. *Chem. Ber.* **1993**, *126*, 869-873.
53. Meyer, M.; Dahaoui-Gindrey, V.; Lecomte, C.; Guilard, R. *Coord. Chem. Rev.* **1998**, *178-180*, 1313-1405.
54. Dunand, F. A.; Borel, A.; Merbach, A. E. *J. Am. Chem. Soc* **2002**, *124*, 710-716.
55. Dunand, F. A.; Aime, S.; Merbach, A. E. *J. Am. Chem. Soc* **2000**, *122*, 1506-1512.
56. Zhang, S.; Wu, K.; Sherry, A. D. *J. Am. Chem. Soc.* **2002**, *124*, 4226-4227.
57. Brücher, E.; Laurenczy, G.; Makra, Z. *Inorg. Chim. Acta* **1987**, *139*, 141.

58. Wang, X.; Jin, T.; Comblin, V.; Lopez-mut, A.; Merciny, E.; Desreux, J. F. *Inorg. Chem.* **1992**, *31*, 1095.
59. Kumar, K.; Magerstadt, M.; Gansow, O. A. *J. Chem. Soc. Chem. Commun.* **1989**, 145.
60. Kumar, K.; Tweedle, M. F. *Inorg. Chem.* **1993**, *32*, 4193-4199.
61. Tóth, É.; Brücher, E.; Lázár, I.; Tóth, I. *Inorg. Chem.* **1994**, *33*, 4070.
62. Wu, S. L.; Horrocks, W. D. j. *Inorg. Chem.* **1995**, *34*, 3724-3732.
63. Marques, M. P. M.; D'Olieslager, W.; Geraldes, C. F. *Eur. J. Solid State Inorg. Chem.* **1991**, *28*, 251.
64. Burai, L.; Fábián, I.; Király, R.; Szilágyi, E.; Brücher, E. *J. Chem. Soc.,Dalton Trans.* **1998**, 243-248.
65. Kumar, K.; Jin, T.; Xiangium, W.; Desreux, J. F.; Tweedle, M. F. *Inorg. Chem.* **1994**, *33*, 3823.
66. Clarke, E. T.; Martell, A. E. *Inorg. Chim. Acta* **1991**, *190*, 37.
67. Desreux, J. F.; Merciny, E.; Loncin, M. F. *Inorg. Chem.* **1981**, *20*, 987-991.
68. Whitbread, S. L.; Politis, S.; Stephens, A. K. W.; Lucas, J. B.; Dhillon, R.; Lincoln, S. F.; Wainwright, K. P. *Dalton Transactions* **1996**, 1379-1384.
69. Stephens, A. K. W.; Dhillon, R. S.; Madbak, S. E.; Whitbread, S. L.; Lincoln, S. F. *Inorganic Chemistry* **1996**, *35*, 2019-2024.
70. Ranganathan, R. S.; Pillai, R. K.; Raju, N.; Fan, H.; Nguyen, H.; Tweedle, M. F.; Desreux, J. F.; Jacques, V. *Inorg. Chem.* **2002**, *41*, 6846-6855.
71. Mikkelsen, K.; Nielsen, S. O. *J. Phys. Chem.* **1960**, *64*, 632-637.

72. van Geet, L. A. *Anal. Chem.* **1970**, *42*, 679.
73. Csajbók, É.; Baranyai, Z.; Bányai, I.; Brücher, E.; Király, R.; Müller-Fahrnow, A.; Platzek, J.; Radüchel, B.; Schäfer, M. *Inorg. Chem.* **2003**, *42*, 2342.
74. Thomas, W. A. *Prog. Nucl. Magn. Reson. Spectrosc.* **1997**, *30*, 183-207.
75. Vander Elst, L.; Maton, F.; Laurent, S.; Seghi, F.; Chapelle, F.; Muller, R. N. *Mag. Reson. Med* **1997**, *38*, 604-614.
76. Schmitt-Willich, H.; Brehm, M.; Ewers, C. L. J.; Michl, G.; Müller-Fahrnow, A.; Petrov, O.; Platzek, J.; Radüchel, B.; Süzle, D. *Inorg. Chem.* **1999**, *38*, 1134-1144.
77. Schmitz, S. A.; Häbesle, J. H.; Balzer, T.; Shamiski, K.; Boese-Landgrag, J.; Wolf, K.-J. *Radiology* **1997**, *202*, 399-405.
78. Vander Elst, L.; Chapelle, F.; Laurent, S.; Muller, R. N. *J. Biol. Inorg. Chem* **2001**, *6*, 196-200.
79. Laurent, S.; Botteman, F.; Vander Elst, L.; Muller, R. N. *Eur. J. Inorg. Chem.* **2004**, 463-468.
80. Burai, L.; Tóth, É.; Merbach, A. E. *Chem. Comm.* **2003**, *21*, 2680-2681.
81. Dunand, F. A.; Dickins, R. S.; Parker, D.; Merbach, A. E. *Chem. Eur. J.* **2001**, *7*, 5160-5167.
82. Thompson, N. C.; Parker, D.; Schmitt-Willich, H.; Sülzle, D.; Muller, G.; Riehl, J. P. *Dalton Trans.* **2004**, 1892-1895.
83. Balkus, K. J.; Shi, J. *J. Phys. Chem.* **1996**, *100*, 16429-16434.
84. McLaughlin, A. C.; Leigh, J. S. *J. Magn. Reson.* **1973**, *9*, 296-304.

85. Leigh, J. S. *J. Magn. Reson.* **1971**, *4*, 308-311.

86. Rakoczy, R. A.; Traa, Y. *Microporous Mesoporous Mater.* **2003**, *60*, 69-78.

87. Mintova, S.; Olson, N. H.; Valtchev, V.; Bein, T. *Science* **1999**, *283*, 958.

88. Dexpert-Ghys, J.; Picard, C.; Taurines, A. *Journal of Inclusion Phenomena and Macrocyclic Chemistry* **2001**, *39*, 261-267.

89. Klein, H.; Fuess, H. *Faraday Trans.* **1995**, *91*, 1813-1824.

90. Yung, K. *Magn. Reson. Imaging* **2003**, *21*, 451-463.

# 9 List of Publications

## *2.1 Papers related to the dissertation*

Dynamic Properties of DOTA-ligand: $^{1}H$ NMR and $^{17}O$ NMR Studies
I. Bányai, É. Csajbók, E. Brücher
*J. Inorg. Biochem.* **2001,** *86,* 137 (Conf. abstract from the 10th International Conference on Bioinorganic Chemistry, Florence, Italy, 26th-31st of August, 2001)

Csajbók, É.; Baranyai, Z.; Bányai, I.; Brücher, E.; Király, R.; Müller-Fahrnow, A.; Platzek, J.; Radüchel, B.; Schäfer,
Equilibrium, $^{1}H$-, $^{13}C$-NMR-Spectroscopy and X-Ray Diffraction Studies on the Complexes $Bi(DOTA)^{-}$ and Bi(DO3A-Bu)
*Inorg. Chem.* **2003** *42* 2342-2349

É. Csajbók, I. Bányai and E. Brücher
Dynamic NMR Properties of DOTA Ligand: Variable pH and Temperature $^{1}H$ NMR Study on $[K(H_xDOTA)]^{(3-x)-}$ Species
*Dalton Trans.* **2004** 2152-2156

R. N. Muller, L. Vander Elst, A. Roch, J.A. Peters, É. Csajbók, P. Gillis, Y. Gossuin
Relaxation by Metal-Containing Nanosystems (review)
*Adv. Inorg. Chem.* (accepted for publication)

## *2.2 Lectures and posters presented at conferences and meetings*

*Lectures:*

É. Csajbók, I. Bányai, E. Brücher:
The intramolecular motion of DOTA ligand as studied by $^{1}$H NMR
XXXVI. Coordination Chemistry Conference, Pécs, 2001 (lecture in Hungarian)

É. Csajbók, I. Bányai, E. Brücher:
NMR studies on the dynamics of inert and labile DOTA complexes
EMT Conference, Félixfürdő, Rumania, 2001 (lecture in Hungarian)

É. Csajbók, I. Bányai, E. Brücher:
NMR structure of Ln-EOB-DTPA stereoisomers
XXXVII. Coordination Chemistry Conference, Mátraháza, 2002 (lecture in Hungarian)

É. Csajbók, E. Brücher, I. Bányai:
Dynamic NMR studies on labile complexes of DOTA (1,4,7,10-tetraazacyclododecane-N,N',N'',N'''-tetraacetic-acid)
9$^{th}$ Nordic Symposium on Coordination Chemistry, Umeå, Sweden (lecture in English)

*Poster presentations:*

É. Csajbók, E. Brücher, I. Bányai:
Intra-and intermolecular exchange processes: the DOTA molecule as an example
„Tavaszi szél"-Meeting of Hungarian Ph.D. Students, Gödöllő, 2001 (Poster in Hungarian)

É. Csajbók, I. Bányai, J. A. Peters
Gd(III)-loaded zeolite nanoparticles as MRI contrast agents
Interdisciplinary Workshop of Marie Curie Fellows, Institute For Energy, Petten, The Netherlands, 2003 (Poster in English)

É. Csajbók, I. Bányai, J. A. Peters
Gd(III)-loaded zeolite nanoparticles as MRI contrast agents
NMR Meeting, Groningen, The Netherlands, 2003 (Poster in English)

É. Csajbók, I. Bányai
Rediscovery of $^{1}$H NMR for studying complex systems: Lanthanides, macrocycles, polyamino-polycarboxylates
COST D18 ”Lanthanide Chemistry for Diagnosis and Therapy” Annual Workshop A Coruna, Spain, 2003 (Poster in English)

G. A. Pereira, C. F. G. C. Geraldes, D. Ananias, J. Rocha, É. Csajbók, J. A. Peters, L. Vander Elst, R. N. Muller
Magnetic, NMR and relaxivity studies of microporous lanthanide(III) silicates
COST D18 ”Lanthanide Chemistry for Diagnosis and Therapy” Annual Workshop A Coruna, Spain, 2003 (Poster in English)

# 10 Acknowledgements

First of all, I would like to thank my supervisors, Dr. István Bányai at the University of Debrecen and Dr. Joop Peters at the Technical University of Delft for their support, help and patience. István, thank you for introducing me to the world of NMR, for the discussions about not only chemistry and for being always ready for "thinking together". Joop, thank you for the daily guidance during my one-year trip to Delft and to the world of zeolites and for the support even when I thought I would never be successful in zeolite synthesis. I would like to thank Prof. Ferenc Joó for the possibility to work at the Physical Chemistry Department in Debrecen as a Ph. D. student and now as a teaching assistant. I am grateful to Prof. Ernő Brücher for his advices, helping me through all these years.

I am grateful to Prof. Robert Muller and Dr. Luce Vander Elst at the University of Mons-Hainaut for the possibility of making the NMRD measurements for Chapter 5.

I am also grateful to Dr. Gyula Batta and Dr. Katalin Kövér for helping me in dealing with NMR theory and measurements.

Special thanks are due to Dr. Éva Porzsolt for being always helpful and ready to deepen my knowledge about how to teach physical chemistry, especially at laboratory practices.

Thanks to Sándor Kovács and Viktor Kátai for their direct and indirect contribution to this thesis during their diploma work in our lab. Köszönöm Agárdiné Antek Éva technikus munkám során nyújtott segítségét.

Thanks to all, past and present roommates in the Ph.D. room in Debrecen: Péter Csabai, Gábor Kovács, Klári Kovács, Rita Tóth, Zoltán Kazsu for the nice time together.

Thanks go to Kristina Djanashvili, Luca Frullano, Petra Lebduskova, Giovannia A. Pereira, Carlos Platas-Iglesias, for their help and friendship during my stay in Delft.

Thanks to all colleagues and lab-mates at the University of Debrecen and at the University of Delft for the friendly atmosphere.

I would like to thank Erika Jacsmenik for her friendship and for weeding out my grammatical and spelling errors in this work.

Köszönöm családomnak, hogy ezek alatt az évek alatt szeretetükkel és türelmükkel támogattak: Anya, Apa, Bátyus, köszönöm. Thank you, András, for your help and support during all these years.

I am grateful to the Hungarian Research Science Foundation (OTKA T035127, to the Marie Curie Fellowship and to the COST D18 program for the financial support.